UC San Diego

UC San Diego Electronic Theses and Dissertations

Title

Molecular and Physical Regulation of Collective Cancer Invasion

Permalink

https://escholarship.org/uc/item/4zm3j5n0

Author

Ranamukhaarachchi, Sural K

Publication Date

2023

Supplemental Material

https://escholarship.org/uc/item/4zm3j5n0#supplemental

Peer reviewed|Thesis/dissertation

eScholarship.org Powered by the California Digital Library
University of California

UNIVERSITY OF CALIFORNIA SAN DIEGO

Molecular and Physical Regulation of Collective Cancer Invasion

A Dissertation submitted in partial satisfaction of the requirements
for the degree Doctor of Philosophy

in

Bioengineering

by

Sural K. Ranamukhaarachchi

Committee in charge:

Professor Stephanie I. Fraley, Chair
Professor Hannah Carter
Professor Adam J. Engler
Professor Pradipta Ghosh
Professor Wouter-Jan Rappel

2023

Copyright

Sural K Ranamukhaarachchi, 2023

All rights reserved.

The Dissertation of Sural K Ranamukhaarachchi is approved, and it is acceptable in quality and form for publication on microfilm and electronically.

University of California San Diego

2023

DEDICATION

To my mother, Nadika, who has taught me moderation, love and humility.

To my father, Daya, who has taught me dedication, perseverance and humility.

To my brother, Sayu, who has taught me fellowship, vitality and humility.

To my dog, Sudu, who has taught me consciousness, love, and humility.

To the brief moment in which I know of my existence, who has taught me…

- *Sural K. Ranamukhaarachchi*
May 01, 2023

EPIGRAPH

Have you ever seen flowing water?

Have you ever seen still water?

If your mind is peaceful, it's kind of like still, flowing water.

Have you ever seen still, flowing water?

You've only seen still water and flowing water.

You've never seen still, flowing water.

Right there, right where your thinking can't take you:

where the mind is still but can develop discernment.

When you look at your mind, it'll be kind of like flowing water, and yet it's still.

It looks like it's still, it looks like it's flowing, so it's called still, flowing water.

That's what it's like.

That's where discernment can arise.

-Ajahn Chah

TABLE OF CONTENTS

DISSERTATION APPROVAL PAGE iii

DEDICATION iv

EPIGRAPH v

TABLE OF CONTENTS vi

LIST OF FIGURES vii

LIST OF ABBREVIATIONS viii

ACKNOWLEDGEMENTS xii

VITA xiii

ABSTRACT OF THE DISSERTATION xiv

INTRODUCTION 1

CHAPTER 1 3

CHAPTER 2 37

CHAPTER 3 73

REFERENCES 94

LIST OF FIGURES

Figure 1.1 8

Figure 1.2 11

Figure. 1.3 14

Figure 1.4 16

Figure 1.5 17

Figure 1.6: Supplementary Figure 1.1. 33

Figure 1.7: Supplementary Figure 1.2 34

Figure 1.8: Supplementary Figure 1.3. 35

Figure 1.9: Supplementary Figure 1.4 36

Figure 2.1 41

Figure 2.2 44

Figure 2.3. 48

Figure 2.4 51

Figure 2.5 53

Figure 2.6 55

Figure 2.7: Supplementary Figure 2.1 71

Figure 3.1 77

Figure 3.2 79

Figure 3.3 81

Figure 3.4 83

Figure 3.5 85

Figure 3.6 87

LIST OF ABBREVIATIONS

ECM	Extracellular Matrix
CCM	Collective Cell Migration
CCI	Collective Cell Invasion
TNBC	Triple Negative Breast Cancer
CSC	Cancer Stem Cells
2D	Two-Dimensional
3D	Three-Dimensional
MMC	Macromolecular Crowding
PEG	Polyethylene Glycol
DQ	Dye-Quenched
AFM	Atomic Force Microscopy
ANOVA	Analysis of Variance
RT-qPCR	Reverse transcription quantitative polymerase chain reaction
FVO	Fractional volume occupancy
FOV	Field of View
D_f	Depth of field
RCM	Rotational Collective Migration
ICM	Invasive Collective Migration
GFP	Green Fluorescent Protein
H2B	Histone 2B
CW	Clockwise
CCW	Counterclockwise

CPM	Cellular Potts Model
MMPs	Matrix Metalloproteinases
MMPi	Matrix Metalloproteinase inhibitor
PCA	Principal Component Analysis
F-actin	Filamentous actin
ITGB1	Integrin Beta 1
CRISPR	Clustered Regularly Interspaced Short Palindromic Repeats
Cas9	CRISPR associated protein 9
WT	Wild Type
crITGB1	Cells with ITGB1 deletion using CRISPR–Cas9
FACS	Fluorescence-Activated Cell Sorting
sgRNA	Small Guide RNA
MIP	Maximum Intensity Projection
NA	Numerical Aperture
H	Hamiltonian
J	Coupling Strength
λ	Lambda, a constant of proportionality
A	Target cell area
P	Cell polarization vector
k	Rate of production or degradation
γ	Polarization persistence
E	Matrix-remodeling agent
D	Diffusion coefficient

δ	Kronecker delta
k_g	Global agent production rate
k_l	Local agent production rate
k_d	Auto-degradation rate of the agent
k_r	Reaction rate of the agent with the ECM
S	Concentration of the ECM
λ_{ECM}	Parameter that indicates the strength of the ECM
G	Cell growth rate
A_{thres}	Threshold cell area value
t	Time
ER	Estrogen Receptor
PR	Progesterone Receptor
EMT	Epithelial-to-Mesenchymal Transition
MET	Mesenchymal-to-Epithelial Transition
NSC	Normal Stem Cells
MDR	Multi-Drug Resistance
APL	Acute Promyelocytic Leukemia
RA	Retinoic Acid
TME	Tumor Microenvironment
TF	Transcription Factor
Col1	Collagen I
LD	Low Density
MD	Medium Density

HD	High Density
RNA-Seq	RNA Sequencing
WGCNA	Weighted Gene Co-expression Network Analysis
GO	Gene Ontology
MSigDB	Molecular Signatures Database
SHG	Second Harmonic Generation
FC	Fold Change
WB	Western Blotting
IC_{50}	Half Maximal Inhibitory Concentration

ACKNOWLEDGEMENTS

I would like to express my utmost gratitude to my thesis advisor, Dr. Stephanie Fraley, for being both a champion and a critic in guiding me towards developing a robust scientific mindset and learning to always question my assumptions. She entrusted me with leading my own project when I started in her lab as an undergraduate, which planted the seed that grew into my love of science and research. When I wandered because of my genuine curiosity, she empowered me to find my way. I will always be grateful for this guidance and philosophy.

I would like to thank each member of my committee, my collaborators, and colleagues in the lab for providing their genuine interest in my projects, shown every single day through questions, ideas, criticisms and excitement. These conversations helped to shine the light on the data I collected and made every single one of those days brighter.

This chapter is a partial reprint of "Macromolecular crowding tunes 3D collagen architecture and cell morphogenesis" as it appears on *Biomaterial Sciences*, 7(2), 618-633. (2019). Ranamukhaarachchi, S. K., Modi, R.N., Han, A., Velez, D.O., Kumar, A., Engler, A.J., Fraley, S.I. Macromolecular crowding tunes 3D collagen architecture and cell morphogenesis. The dissertation author was the co-primary investigator and co-first author of this paper.

Chapter 2, in part is currently being prepared for submission for publication of the material. Ranamukhaarachchi, S. K., Walker, A., Tang, M.H., Leineweber, W.D., Lam, S., Rappel, W.J., Fraley, S.I. The dissertation author was the co-primary investigator and co-first author of this paper.

Chapter 3, in part is currently being prepared for submission for publication of the material. Ranamukhaarachchi, S. K., Klie, A., Turner, J., Simon, J., Lam, S., Ghosh, P., Carter, H., Fraley, S.I. The dissertation author was the primary researcher and author of this material.

VITA

2018 Bachelor of Science in Physiology & Neuroscience, University of California San Diego

2023 Doctor of Philosophy in Bioengineering, University of California San Diego

PUBLICATIONS

Ranamukhaarachchi, S. K. ‡, Walker, A. ‡, Tang, M.H., Leineweber, W.D., Lam, S., Rappel, W.J., Fraley, S.I., Initial cell-matrix interactions determine collective migration and morphogenesis programs. *In Preparation* (2023).

Ranamukhaarachchi, S. K., Klie, A., Turner, J., Simon, J., Lam, S., Ghosh, P., Carter, H., Fraley, S.I., Therapeutic differentiation of CSCs in preclinical models of Triple Negative Breast Cancer. *In Preparation* (2023).

Ranamukhaarachchi, S. K. ‡, Modi, R.N. ‡, Han, A., Velez, D.O., Kumar, A., Engler, A.J., Fraley, S.I. Macromolecular crowding tunes 3D collagen architecture and cell morphogenesis. *Biomaterial Sciences*, 7(2), 618-633. (2019).

Velez, D., **Ranamukhaarachchi, S.K.**, Kumar, A., Modi, R., Lim, E., Engler, A.J., Metallo, C.M., Fraley, S.I. 3D collagen architecture regulates cell adhesion through degradability, thereby controlling metabolic and oxidative stress. *Integrative Biology*, 11(5), 221-234. (2019).

Cardozo, L., Dillingham, B., de Sousa, A., Dang, W., Job, N., Yoo, E. J., **Ranamukhaarachchi, S. K.**, Yuan, Q. Mayford, M. Localized Synaptic Potentiation is Necessary and Sufficient for Context Fear Memory. *BioRxiv* (2022).

Scott, K., Rychel, K., **Ranamukhaarachchi, S.K.**, Rangamani, P., Fraley, S. Emerging themes and unifying concepts underlying cell behavior regulation by the pericellular space. *Acta Biomaterialia*, 96, 81-98. (2019).

Guerrero-Cazares, H., Lavell, E., Drummond, G., **Ranamukhaarachchi, S.K**., Capilla-Gonzalez, V., Schiapparelli, P., & Quinones-Hinojosa, A. Abstract 444: Slit2 stimulation induces a chemorepellent effect on the migration of human GBM brain tumor initiating cells. *Cancer Research, 75(15_Supplement), 444-444*. (2015).

Guerrero-Cazares, H., Capilla-Gonzalez, V., Lavell, E., Ruiz-Valls, A., Chen, L., Drummond, G., **Ranamukhaarachchi, S.K**., & Quinones-Hinojosa, A. Abstract 3153: Slit-2 directs the migration of primary cultured human GBM tumor initiating cells. *Cancer Research*, 74(19_Supplement), 3153-3153. (2014).

R.N. Modi & **Ranamukhaarachchi, S.K.** (2018). Vasculogenic Mimicry: A Driver of Cancer Metastasis. *Saltman Quarterly.*

ABSTRACT OF THE DISSERTATION

Molecular and Physical Regulation of Collective Cancer Invasion

by

Sural K. Ranamukhaarachchi

Doctor of Philosophy in Bioengineering

University of California San Diego, 2023

Professor Stephanie I. Fraley, Chair

Cellular plasticity is essential for healthy function during development and healing. However, it is the dysregulated plasticity of neoplastic cells that gives cancer its advantageous heterogeneity and resistance to therapy. Plasticity also endows cancer cells with the ability to mimic and aberrantly activate fundamental developmental processes such as collective cell migration (CCM) in the form of collective invasion, which initiates the metastatic cascade that is the primary cause for cancer-related deaths. Remarkably, the initiation of this process is strongly associated with changes in the extracellular matrix (ECM) environment of the tumor, which functions as both a physical barrier and dynamic signaling cue for cell migration. Namely, simultaneous increases in the density, stiffness, and alignment of Collagen I fibers in the tumor

ECM mark a key transition. However, challenges associated with modeling this process limit our capacity for identifying new approaches that target these plastic cancer cells. In this dissertation, we develop ECM engineering and dynamic measurement techniques to enable study of the biophysical cell-cell and cell-matrix interactions that drive collective cancer cell invasion. We then use these newfound insights to develop a phenotypic screening model that successfully identifies a cytodifferentiation therapy of plastic Triple Negative Breast Cancer (TNBC) cells.

In chapter I, we advance a matrix engineering approach to tune Collagen I fibrillar architecture independently of known modulators of collective cell behavior such as ECM density and stiffness. We find that tighter fibril networks are less degradable and adhesive, inducing cellular confinement that prompts a switch from single cell migration to CCM. Chapter II integrates multiple modalities of biophysical imaging with *in silico* modeling to dissect the underlying cell-cell and cell-matrix interactions of the two distinct CCM behaviors that emerge from single populations of cancer cells in confining matrices: collective rotational migration and collective invasive migration. We find that the predominant phenotype of invasive CCM relies on a combination of proteolytic-based matrix remodeling and physical remodeling while the less common rotational CCM relies solely on mechanical-based matrix remodeling. Contrary to the current paradigm, we also find that epithelial characteristics such as cadherin-based cell-cell junctions or establishment of a Laminin-rich basement membrane are non-essential for either CCM behavior. In chapter III, we conduct a phenotypic screen of TNBC cells within confining Collagen I matrices to identify cytodifferentiation therapies targeting CCM, a trait that is associated with enrichment for Cancer Stem Cells (CSCs). Phenotypic screening identified two structurally similar leads that abrogate collective invasion, induce CSC cytodifferentiation and Mesenchymal-to-Epithelial Transition, and increase sensitivity to traditional chemotherapies.

Importantly, this cytodifferentiation response is not observed in 2D-treated cells or in non-confining 3D matrices, highlighting our simple 3D phenotypic screening assay as an improved method for identifying relevant cytodifferentiation therapies for TNBC. Taken together, we provide a bottom-up description of how understanding and designing cell-matrix interactions can give rise to physiologically relevant CCM behaviors that provide a novel paradigm for identifying therapeutics that target cancer plasticity.

INTRODUCTION

Cancer remains a major public health issue and a critical barrier to increasing life expectancy in every country of the world(Bray *et al.*, 2021). In 2019, the World Health Organization (WHO) estimated that cancer is the first or second leading cause of death before the age of 70 years in most countries worldwide.(*& Others. Global Health Estimates 2020: Deaths by Cause, Age, Sex, by Country and by Region*, 2000) The vast majority of these cancer-related deaths are due to metastasis, the multistep colonization of a distant organ site that advances cancer from a local lesion to a systemic disease.(Welch & Hurst, 2019) Initiation of this cascade requires tumor cells to penetrate the Collagen-rich peritumoral stroma, which provides a protective barrier from intravasation and systemic access. Interestingly, this extracellular matrix (ECM) environment itself undergoes several transformations as cancer progresses, including simultaneous increases in density, stiffness, and alignment of Collagen I fibers, which can assist collective invasion into the stroma.(Guo et al., 2001; Habel et al., 2004; Haeger et al., 2014; Paszek et al., 2005; P. P. Provenzano et al., 2009; Paolo P. Provenzano et al., 2006; Ursin et al., 2005) How might cells sense such changes and redirect their behavior accordingly? While collective movements are diverse and complex, their emergence is thought to arise from the interplay of cell-cell and cell-matrix interactions that are dependent on the position of cells within the collective, as well as the constraints imposed on cells by the extracellular environment.(Ladoux & Mège, 2017) The transformation of once-sedentary epithelial cells into motile cell groups is also enabled by transdifferentiation programs such as the epithelial-to-mesenchymal transition (EMT), with individual cells within a collective harboring genotypically and phenotypically distinct hybrid “E/M” states that prove advantageous for coordinating migration through the heterogenous stromal microenvironment.(Dongre &

Weinberg, 2019) In this thesis, we hypothesize that a better understanding of how the ECM directs collective cell invasion can help us to identify novel therapies targeting metastatic migration. In chapter I, we will explore whether ECM architecture can independently regulate collective cancer migration. In chapter 2, we will ask what are the underlying cell-cell and cell-matrix interactions that distinguish distinct forms of collective migration in both cancerous and normal epithelial cells. In chapter 3, we will ask whether we can use collective cell migration heterogeneity as a phenotypic screening model for identification of drugs targeting EMT and cancer stem cell differentiation.

CHAPTER 1

Macromolecular crowding tunes 3D collagen architecture and cell morphogenesis

1.1 Introduction

Collagen is the most abundant matrix component within the tumor microenvironment,(Fang *et al.*, 2014) and both clinical and *in vivo* studies have established the relevance of this particular ECM molecule in tumor progression. Collagen is both an independent clinical prognostic indicator of cancer progression(Conklin *et al.*, 2011) and a driver of tumorigenesis and metastasis.(Paolo P. Provenzano et al., 2008) As such, understanding how 3D collagen regulates cancer cell behavior could provide useful insights into disease pathogenesis and potential ECM targeted therapies.

The fibril architecture of collagen matrices has been implicated as a critical regulator of cancer cell behavior.(Fraley et al., 2012, 2010; Yue et al., 2016) However, it remains challenging to systematically vary architectural features like pore size and fiber alignment without also changing matrix density or stiffness, which are known to modulate cell behavior in their own right.(Jiang et al., 2006; Lo et al., 2000; Paszek et al., 2005) Gelation temperature, pH, or density of collagen can be used to tune matrix architecture, but each of these approaches also alters matrix stiffness.(Wolf et al., 2013; Wood & Keech, 1960; Xie et al., 2017) Magnetic, mechanical, and cell force driven reorganization of collagen fibrils as well as electrospinning can also be used to tune matrix architecture.(Ceballos et al., 1999; Dubey et al., 2001; Haeger et al., 2014; Oliveira et al., 2012) However, the resulting matrices present stiffness anisotropy to cells.(Antman-Passig et al., 2017; Engler, Griffin, et al., 2004; Paolo P. Provenzano et al., 2010; Ray et al., 2017; Zeng et al., 2017) Collagen engineering techniques capable of modulating fibril

characteristics independently of density and stiffness while also allowing cells to be fully embedded in 3D could lend new insight into how matrix architecture modulates cell behaviors.

Macromolecular crowding (MMC) is one possible approach to modulate fiber architecture without changing matrix stiffness or density. MMC is a phenomenon where high concentrations of macromolecules occupy space and generate excluded volume effects.(C. Chen et al., 2011; Lareu et al., 2007) Various MMC agents have been used to effectively tune matrix properties for tissue engineering applications, including to promote cell-derived matrix deposition, to produce hierarchical porous structures in bioprinting applications, and to tune the reconstituted structure of tissue-derived matrices.(Bateman et al., 1986; C. Chen et al., 2011; Dewavrin et al., 2014; Lee et al., 2016; Magno et al., 2017; Ng et al., 2018) However, previous studies have tuned matrix stiffness simultaneously with fibril architecture.(Dewavrin *et al.*, 2014; Magno *et al.*, 2017) Here, we sought to build on MMC-based matrix modification techniques to tune collagen matrix architecture (1) without changing matrix stiffness and (2) without direct effects of MMC on cell morphology migration or viability in fully embedded 3D culture.

We show that 8 kDa PEG can be used to fine-tune collagen architecture while simultaneously embedding cells, with no significant impact on cell viability, morphology, or migration. We also demonstrate that linearly increasing the amount of PEG added during collagen assembly and cell embedding reliably tunes fibril topography without significantly altering matrix stiffness or ligand density. Increasing amounts of PEG result in tighter networks of collagen fibers that are less degradable. This combination of features has the effect of confining cells in a rounded shape, reducing contractility, inducing the expression of cell–cell adhesion proteins, and triggering collective morphogenesis. We find that matrix degradability and fibril length are the strongest predictors of cellular confinement. In turn, confinement

predicts collective cell behavior. This suggests that matrix degradability and fibril length are key biomaterial design features for tuning confinement and morphogenesis outcomes in collagen matrices.

1.2 Results

1.2.1 Macromolecular crowding with PEG tunes collagen fibrils

To explore the impact of collagen architecture on cancer cell behavior in a 3D matrix, we sought to tune the fibril network of a 2.5 mg ml^{-1} collagen matrix without changing the density or stiffness of the matrix. The assembly of collagen I solution *in vitro* into a fibrous 3D matrix is thought to be driven by diffusion-limited growth of nucleated monomers, which is tunable through MMC.(Parkinson et al., 1995; Wess, 2005) Previous studies have used large molecular weight MMC agents (>50 kDa), which alter matrix stiffness along with fibril architecture.(Dewavrin *et al.*, 2014; Magno *et al.*, 2017) We chose to use a lower molecular weight molecule (8 kDa) in an attempt to finely tune the fibril architecture and minimize impacts on mechanical properties of the matrix. In choosing our MMC material, we found that several agents have been shown to affect the proliferation or viability of cells.(Rashid et al., 2014; Salvalaggio et al., 2002) However, PEG is a commonly used MMC agent for studies of biomolecular polymerization, like actin, and has been shown to be non-toxic for several different cell types including fibroblasts, cancer cells and stem cells.(Bateman *et al.*, 1986; Liu *et al.*, 2017) Additionally, PEG is a widely used material for the preparation of hydrogels for the study of cell migration and morphogenesis programs.(Lutolf & Hubbell, 2005) Thus, we chose to test PEG for our purposes. First, we investigated whether 8 kDa PEG modulates the pre-nucleation and nucleation phases of collagen polymerization, as has been the reported effect of other MMC molecules on biopolymer fibrilation.(Dewavrin *et al.*, 2014; Magno *et al.*, 2017) A dynamic

turbidimetry analysis(Dewavrin et al., 2014; Silver & Birk, 1983) (Supplementary Fig. 1.1A) revealed that addition of PEG to collagen solutions during polymerization dramatically shortened the lag time before nucleation (Supplementary Fig. 1.1B). This mechanism is similar to that of Ficoll and demonstrates that fibril architecture modification is a consequence of fibril formation in a molecularly crowded environment.(Dewavrin *et al.*, 2014)

Having validated PEG's ability to modify nucleation, we sought to tune collagen architecture. To do so, we introduced increasing amounts of 8 kDa PEG (0–10 mg ml^{-1}, labeled P0–P10) into a 2.5 mg ml^{-1} collagen I solution during polymerization. The gels were then washed with PBS to remove the PEG. Fig. 1.1A shows the resulting fibril architecture. Based on the small hydrodynamic radius of 8 kDa PEG (2.45 nm) (Kuznetsova et al., 2014; Rubinson & Krueger, 2009), we expected that diffusion of PEG out of the gel would not be hindered in any matrix condition. To validate this assumption, we measured the diffusivity of fluorescently labeled PEG in the matrix. We found no significant difference in the diffusion of PEG between the least and most crowded architectures (Supplementary Fig. 1.1C). Additionally, SEM imaging of the P10 matrix showed no evidence of PEG after washing (Fig. 1.1B). These experiments indicate that the PEG included during polymerization is effectively removed by washing afterwards.

Next, we characterized the resulting collagen architectures (Fig. 1.1, A and B). Quantitative analysis of reflection confocal images after washing and removal of the PEG revealed a linear decrease ($r^2 = 0.99$, $p = 0.0005$) in average fibril length from 14.1 μm without PEG (P0) to 11.7 μm with 8 mg ml^{-1} of PEG (P8) mixed in during polymerization (Fig. 1.1C). Interestingly, this trend reversed between 8 and 10 mg ml^{-1} of PEG, where average fibril length increased slightly from 11.7 μm to 12.4 μm (Fig. 1.1C). The average pore size of the matrices

varied irregularly, ranging from 1.75 to 2.2 μm^2 (Fig. 1.1D). These measurements are consistent with those reported by other groups analyzing collagen matrices of similar density using confocal reflection microscopy (~0.78–1.8 μm^2 pore areas for 2.5 mg ml^{-1} collagen;(Lang *et al.*, 2013) 2–5 μm^2 pore areas for 1.7 mg ml^{-1} ((Wolf *et al.*, 2013))) and cryo-EM (~3 μm^2 pore areas, 2 mg ml^{-1} collagen(Banerjee *et al.*, 2008)). Since larger pores could be more relevant in terms of influencing cell behavior than the average pore size of the matrix, as large pores could allow for easier cell migration, we also analyzed the 99^{th} percentile of pore size. Again, we found an irregular trend as crowding increases (Fig. 1.1E). Average fibril width, analyzed by SEM, varied by approximately 35 nm between the conditions with the highest and lowest PEG concentrations (Supplementary Fig. 1.1, D and E). These data show that MMC with PEG tunes collagen matrix architecture, with an overall effect of producing tighter networks with shorter fibers and smaller pores.

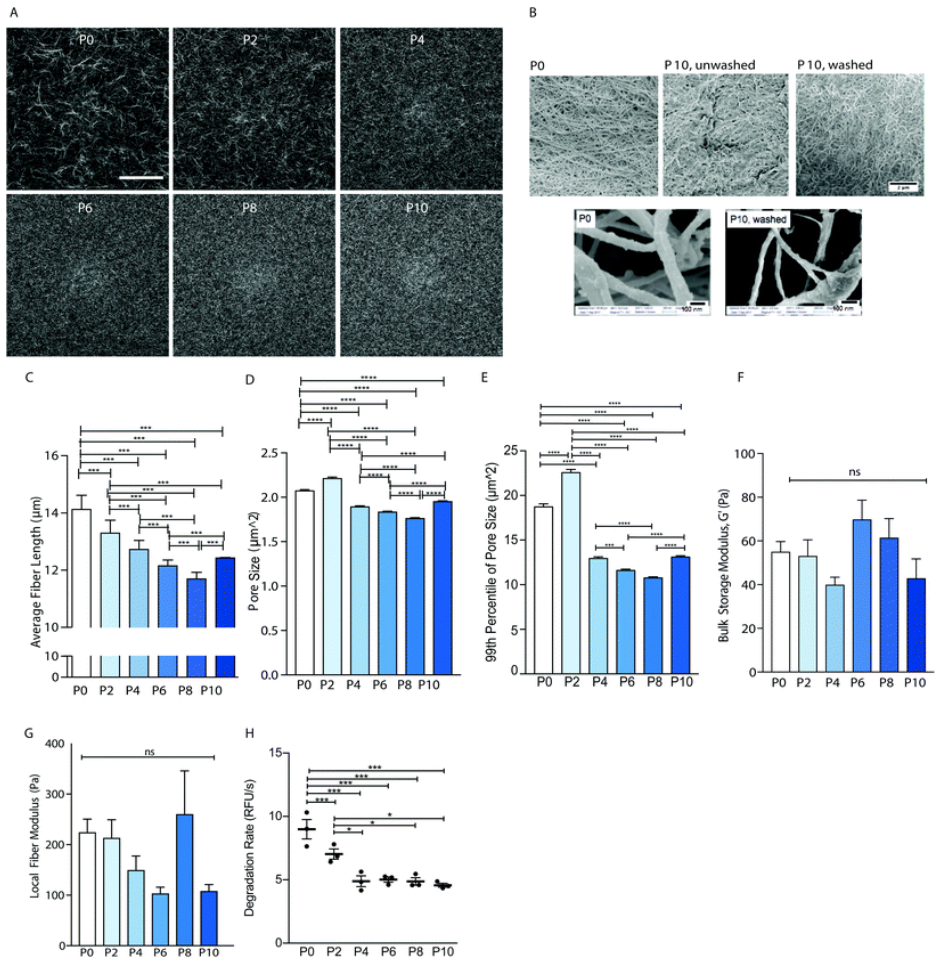


Figure 1.1 Fibril topography modulation by molecular crowding. (a) Reflection confocal micrographs of 2.5 mg ml^{-1} collagen polymerized without a molecular crowding agent, P0, or with 2–10 mg ml^{-1} of 8 kDa PEG as a crowding agent, P2–P10. Scale bar is 200 µm. (b) SEM images of a 2.5 mg mL^{-1} collagen gel (top left) and 2.5 mg ml^{-1} collagen gels polymerized with 10 mg mL^{-1} PEG without washing (top middle) or with thorough washing before fixing (top right). Bottom images are magnified versions of top left and right images. (c) Characterization of mean fibril length as a function of the extent of crowding. (d) Characterization of mean pore size and (e) 99th percentile of pore size as a function of the extent of crowding. (f) Bulk storage moduli of control and crowded matrices measured by shear rheometry. (g) Local moduli of control and crowded matrices measured by AFM. Measurements were taken at multiple locations, ~10 fibrils per replicate, three replicates per condition. (h) Characterization of matrix degradability by rh-MMP-8 as a function of molecular crowding. Unless noted above, n = 3 replicates per condition. At least three fields of view were analyzed per replicate. Graphs show the mean and standard error of measurements. Statistical significance tested by ANOVA and reported as $p < 0.001$, ***; $p < 0.01$, **; $p < 0.05$, *.

1.2.2 MMC does not significantly alter matrix mechanics

We next asked whether the mechanical properties of the 2.5 mg ml^{-1} matrix changed as a function of fibril architecture. To assess this, we measured the bulk and local stiffness of each matrix using shear rheometry and atomic force microscopy (AFM), respectively, after washing out the PEG. No significant differences were observed in the bulk storage moduli across all

conditions (P0–10) (Fig. 1.1F). To probe the local stiffness, an AFM tip of approximately the same size scale as nascent mechanosensory adhesions was chosen.(Choi *et al.*, 2008) No significant differences were observed across all crowding conditions (Fig. 1.1G). Importantly, the non-significant variation in the measured stiffness is well below the reported threshold for mechanosensory cellular responses.(Engler *et al.*, 2006; Wei *et al.*, 2015) These experiments demonstrate that MMC modulates collagen fibril architecture without significant alterations to matrix stiffness.

1.2.3 MMC mediated fibril modification alters matrix degradability

Finally, we asked whether the degradability of the 2.5 mg ml^{-1} matrix changed as a function of fibril architecture, since previous studies have shown a relationship between fibril architecture and sensitivity to enzymatic degradation.(Dewavrin *et al.*, 2014) To measure degradability, we incorporated dye-quenched (DQ) collagen into each matrix condition during gelation and MMC. After gelation, we removed the PEG using our washing procedure and added recombinant human MMP-8. Then, we monitored the rate of fluorescence increase, which corresponds to DQ collagen cleavage. Fig. 1.1H shows that increasingly crowded architectures corresponded to decreased degradability. To verify that diffusion of MMP-8 (52 kDa) was not hindered by changes in architecture, which could impact the rate of DQ cleavage, we measured the diffusivity of fluorescent dextran of approximately the same size (70 kDa) in the matrices. No significant differences in diffusivity were observed (Supplementary Fig. 1.1F). Taken together, the results of our matrix characterization experiments show that MMC produces progressively tighter, less degradable collagen matrices without altering stiffness or total ligand density.

1.2.4 MMC does not directly influence cell behavior

Our control experiments described above showed that PEG was not detectable in the matrices after washing. However, to ensure that potential residual PEG would not have a direct impact on cells, we conducted additional control experiments. We embedded MDA-MB-231 cells in a 2.5 mg ml^{-1} collagen matrix with no PEG added during polymerization. Then, we added 10 mg ml^{-1} PEG, the maximum concentration of PEG used in our matrix engineering experiments, on top of the fully polymerized matrix and allowed the 8 kDa molecules to freely diffuse into the interstitial spaces (Fig. 1.2A). In these experiments, no washing of the matrix was conducted. After 15 hours of culture, no significant differences were observed in cell morphology or migration, as assessed by cell circularity and the total path length traveled by the cells, respectively (Fig. 1.2, B and C). Next, we assessed the viability of the cells cultured for seven days in P0 gels with 10 mg ml^{-1} PEG added after polymerization. Live-dead staining revealed a very slight increase in cell viability between the two conditions (Fig. 1.2, D and E). We also noted that cells remained as single cells during this week of culture with PEG (Fig. 1.2D). Reflection confocal analysis of the matrix architecture with and without PEG added after polymerization revealed only slight differences in average fibril length (<1 μm) and pore size (<0.5 μm^2) (Supplementary Fig. 1.2, B and C). These control experiments confirm that residual PEG left by an imperfect wash does not alter cell morphology or influence the cell's ability to migrate.

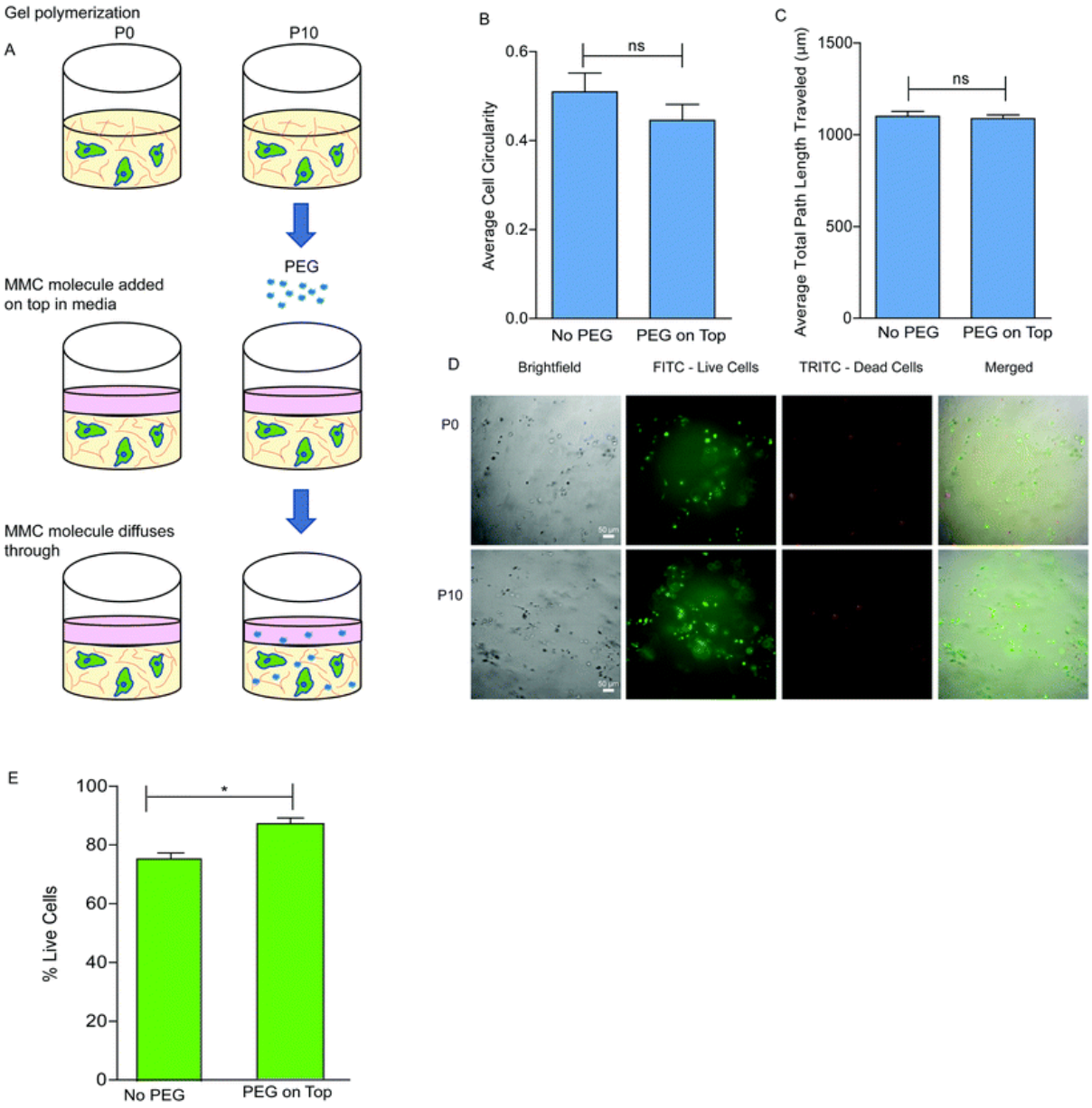


Figure 1.2 Influence of PEG alone on cell morphology, migration, and viability in 3D. (a) Schematic of control experimental setup. PEG was added *after* collagen polymerization to evaluate potential effects on cell behavior independent of matrix changes. Influence of PEG crowding on (b) cell circularity and (c) cell migration over 15 h. (d) Representative micrographs of cells after one week in culture showing brightfield (left), live (green), and dead (red) cell staining. Merged image on right. (e) Viability evaluated after one week of PEG crowding *after* polymerization. $N = 3$ biological replicates for each condition. At least 100 cells were analyzed per condition, ~35 per replicate. Bar graphs show the mean and standard error of measurements. Statistical significance tested by ANOVA and reported as $p < 0.001$, ***; $p < 0.01$, **; $p < 0.05$, *.

1.2.5 3D collagen fibril topography patterns cell shape

Next, we explored the influence of matrix architecture on the morphology and migration of cancer cells. To do so, we polymerized 2.5 mg ml^{-1} collagen I with a low seeding density of

MDA-MB-231 breast cancer cells and 0–10 mg ml^{-1} PEG mixed in. After polymerization, the cell-laden gels were washed to remove the PEG as described above. Single cells were then monitored using time lapse microscopy. Fig. 1.3A shows representative cell images observed at 15 h after seeding in each matrix condition. These morphology differences are a result of cell–matrix interactions as opposed to cell–cell interactions, as data was collected when cells were sparsely seeded and had not yet divided (Supplementary Fig. 1.2A). Quantitative assessment of individual cell shapes at this 15 h timepoint revealed that cell circularity increases with increasingly crowded architectures (Fig. 1.3, A and B).

Based on prior studies by others in the field, which modified collagen architecture by varying gelation temperature and found that small pore sizes correlated with cell confinement, we hypothesized that small pores limited cell spreading and as such would be predictive of cell circularity. However, plotting pore size *versus* cell circularity revealed no significant correlation (Supplementary Fig. 1.2, D and E). However, plotting the mean fiber length against the mean cell circularity in each matrix condition (Fig. 1.3C) showed a strongly linear and significant inverse correlation ($r = -0.94$, $p = 0.005$). Likewise, plotting degradability of the matrix against the mean of cell circularity in each condition (Fig. 1.3D) also showed a strongly linear and significant inverse correlation ($r = -0.89$, $p = 0.02$). This suggests that both fiber length and degradability are covariates in MMC-engineered collagen architectures and are strong predictors of cell confinement.

1.2.6 Confinement impacts cell contractility

Cell circularity induced by other means, *e.g.* microcontact ECM patterning or low stiffness substrates, is often associated with lower actomyosin contractility measured by reduced pMLC.(N. Jain et al., 2013; McKenzie et al., 2018) To probe the influence of confining matrix

architecture on the contractile phenotype of cells, we blotted for pMLC 15 h post cell embedding. Cells in confining P10 matrices remained rounded and contained less pMLC, while those in non-confining P0 matrices had spread and contained more pMLC (Fig. 1.3E), indicating that confined cells were indeed less contractile.

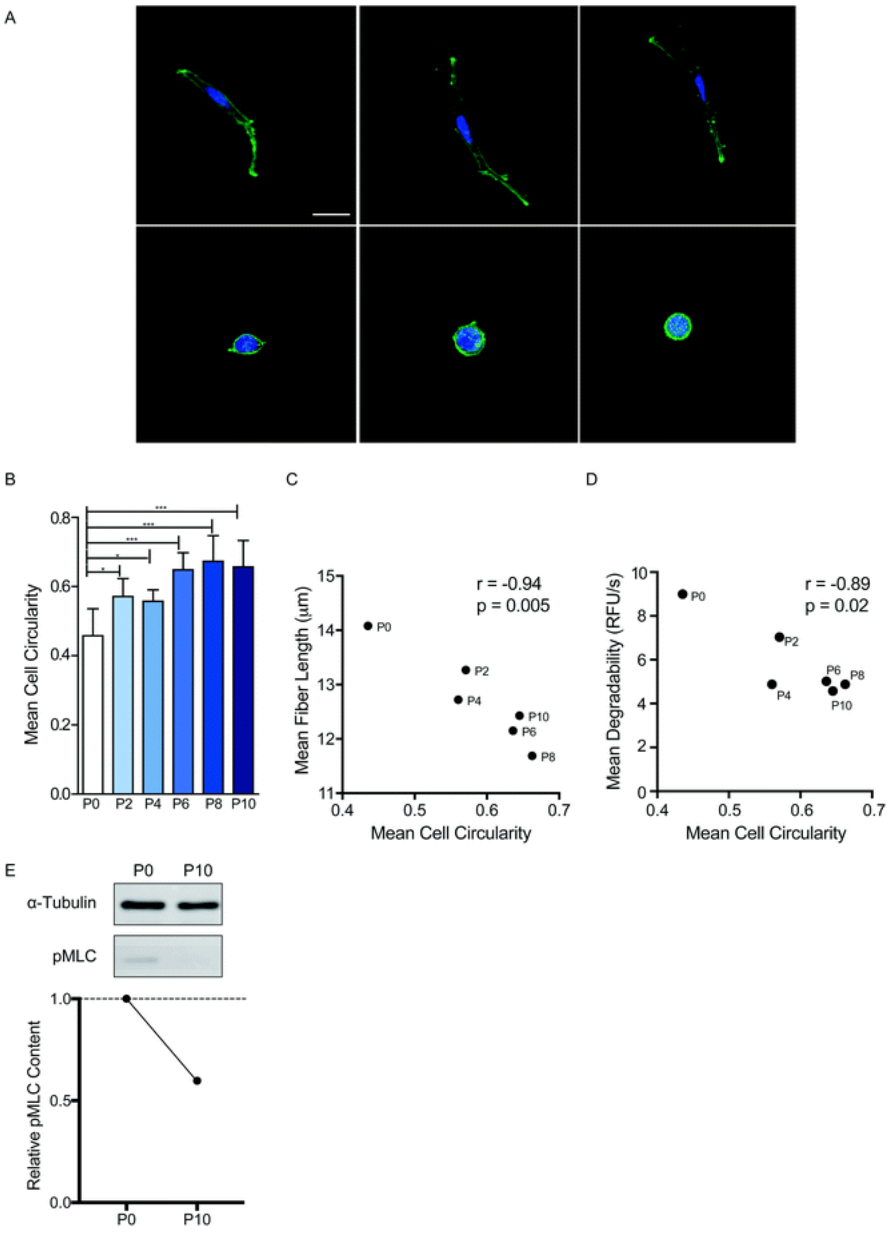


Figure. 1.3 Influence of crowded collagen fibril architectures on cell shape. (a) Representative micrographs of cells in each matrix condition, P0–P10, after 15 hours showing phalloidin (actin, green) and DAPI (nuclei, blue). Scale bar is 25 μm. (b) Mean cell circularity of cells in each matrix construct. (c) Mean fiber length and (d) mean degradability plotted against mean cell circularity in each construct with Pearson correlation coefficient displayed and significance displayed. (e) Western blot analysis of phosphorylated myosin light chain (pMLC) of cells in 2.5 mg ml^{-1} collagen (P0) and 2.5 mg ml^{-1} collagen with 10 mg ml^{-1} PEG (P10) at 15 h after embedding. $N = 3$ biological replicates for each condition. At least 100 cells were analyzed per condition, ~35 per replicate. Bar graphs show the mean and standard error. Statistical significance tested by ANOVA and reported as $p < 0.001$, ***; $p < 0.01$, **; $p < 0.05$, *.

1.2.7 3D collagen fibril topography modulates a transition from individual to collective cell behaviors and morphogenesis

Prior studies indicate that changes in actomyosin contractility can be associated with cellular reprogramming.(N. Jain et al., 2013) Therefore, we examined the impact of collagen fibril topography on breast cancer cell migration using the PEG-tuned matrices. To do so, we monitored MDA-MB-231 cells for seven days in P0–P10 matrix constructs. A striking transition from single cell behavior to collective morphogenesis was observed in the 2.5 mg ml^{-1} collagen matrices crowded with at least 6 mg ml^{-1} of PEG (P6, Fig. 1.4A). Collective cell behaviors arose in this condition as a series of distinct cell bodies in a chain-like structure. In the P8 and P10 conditions, similar chain-like structures were present, but were more fused and smooth-edged. These smooth-edged structures are characterized by having multiple cell bodies tightly fused to each other, with no apparent cellular protrusions extending outside the main structure (Fig. 1.4A and 1.5C). Fig. 1.4B shows the frequency of single cell, multicellular chain, and multicellular smooth structure phenotypes across all conditions. Multicellular structures resembling lobular and glandular structures of normal breast tissue(Sokol *et al.*, 2016) also emerged in the P8 and P10 conditions (Fig. 1.4C). Importantly, in the previously mentioned control condition where PEG was added after polymerization of a P0 matrix and left for seven days, no multicellular structures were observed (Fig. 1.2D). Again, this demonstrates that matrix architecture, not PEG, influences cell morphogenesis in our system.

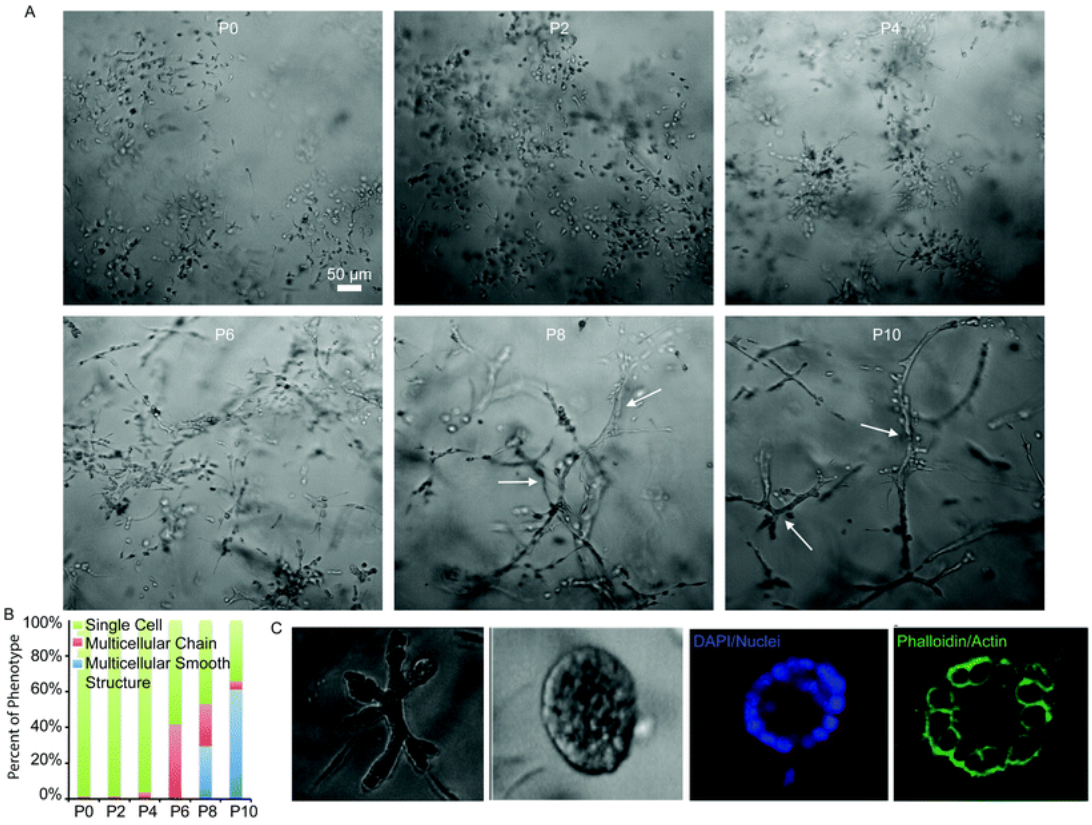


Figure 1.4 Influence of 3D fibril topography on cell behavior. (a) Representative brightfield micrographs of cells in each matrix construct after one week of culture. Arrows indicate the multicellular smooth structure phenotype that arises in the P8 and P10 conditions. (b) Frequency of phenotypes observed in each matrix construct. (c) Additional multicellular structures observed at low frequency in P8 and P10 conditions. Lobular (left) and acinar (right three images) structures resembling normal breast structures. Rightmost two images show representative acinar structure stained with DAPI (nuclei, blue) and phalloidin (actin, green), revealing an organized and hollow morphology.

Since tighter matrix architectures inhibited cell spreading and reduced pMLC at early timepoints (Fig. 1.3E), we wondered if matrix-induced cell confinement was predictive of the collective morphogenesis behaviors that arise later, over the course of seven days. To assess this, we compared cell circularity to the frequency of single cell *versus* multicellular phenotypes across the matrix conditions (Fig. 1.5A). We observed that multicellular structure formation was triggered exclusively in matrices where cell circularity was above ~0.6. As previously mentioned, cell circularity is predicted by matrix degradability and fiber length. This suggests that these two biomaterial parameters are useful for tuning single *vs.* collective behaviors through confinement.

To begin to elucidate the mechanism by which cells initiate cell–cell interactions in confining matrix architectures, we conducted gene expression analysis using RT-qPCR. This revealed that the multicellular phenotype is associated with expression of several cell–cell adhesion genes, including PECAM1, ICAM1, CTNNA1, ITGB4, and ITGB5 (Fig. 1.5B). Immunofluorescent staining of ICAM1 confirmed high protein expression in cell–cell junctions of MDA-MB-231 cancer cells undergoing the collective phenotype (Fig. 1.5C).

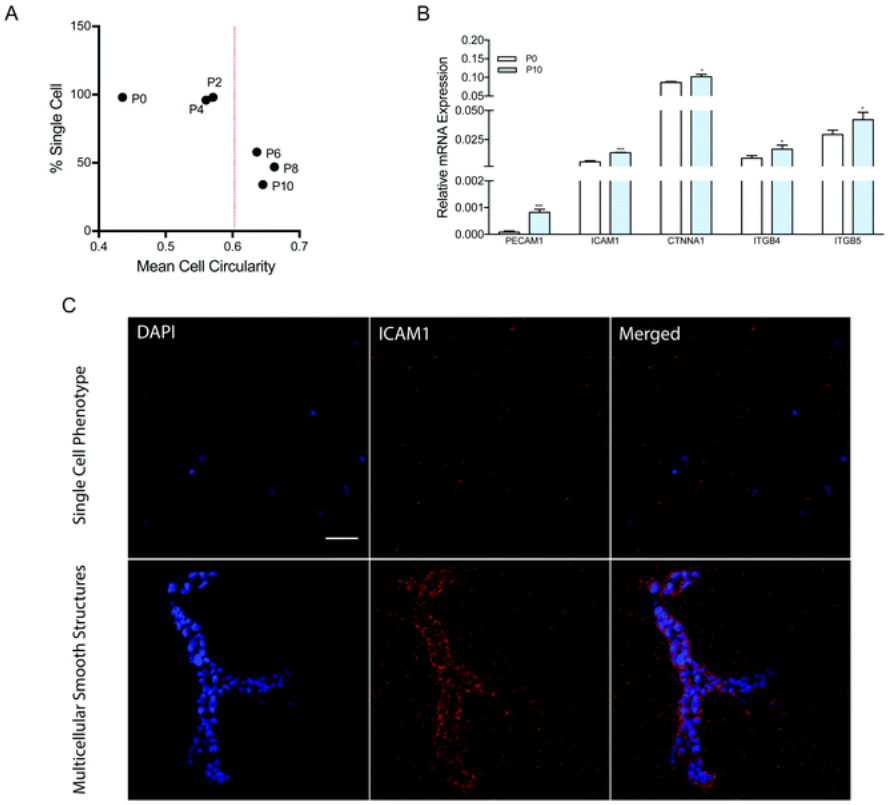


Figure 1.5 Cell confinement within the matrix predicts collective behavior. (a) Frequency of the single cell phenotype in each matrix construct plotted against the mean cell circularity in each construct. Red line shows the approximate cell circularity threshold predicting the transition from single to multicellular behavior. (b) Relative mRNA expression of cell–cell adhesion genes upregulated by cells in P10 constructs. (c) Immunofluorescence staining of MDA-MB-231 cells undergoing the multicellular phenotype. DAPI (nuclei, blue), ICAM1 (red), and merged images are shown. Scale bar shows 100 μm. $N = 3$ biological replicates for each measurement. Statistical significance tested by ANOVA and reported as $p < 0.001$, ***; $p < 0.01$, **; $p < 0.05$, *.

1.3 Discussion

Using PEG as an MMC agent, we successfully tuned 3D collagen fibril architecture without significantly altering matrix stiffness or ligand density. The slight variation in the

measured stiffness across crowding conditions was well below the reported threshold for mechanosensory cellular responses,(Engler *et al.*, 2006; Wei *et al.*, 2015) and is thus biologically insignificant. The stiffness of 2.5 mg ml^{-1} collagen (P0) has previously been shown to mimic normal breast tissue.(Paszek *et al.*, 2005) All of our PEG-crowded and non-crowded 2.5 mg ml^{-1} collagen constructs are within this range of stiffness and can be considered representative of the mechanical conditions cancer cells encounter during tissue invasion and metastasis.

The magnitude of the architectural changes induced by crowding were not as dramatic as those previously achieved by other means, such as varying gelation temperature or using larger MMC agents. This may explain the similarity in the mechanical behavior among our different collagen architectures created using a small MMC, whereas changes induced by larger MMCs or gelation temperature variations are greater and do impact matrix mechanics.(Haeger et al., 2014; Wolf et al., 2013) The similarity in mechanical properties across our crowding conditions may result from a balance between an increase in the connectivity of the collagen network (shorter fibers, smaller pores) and a simultaneous weakening of fibril connections, since overall density does not change.(Depalle *et al.*, 2015) Despite the relatively small magnitude of changes in matrix architecture produced by MMC, these were significant enough to dramatically alter cell behavior.

Similar to other MMC agents, our data shows that PEG causes a significant decrease in the lag time during the nucleation phase of collagen I gelation, thus leading to the development of shorter fibers. Interestingly, we show that this change can be achieved using a relatively small molecule (8 kDa) as compared to previous reports where molecules up to 400 kDa have been used. The fractional volume occupancy (FVO) we achieve with 8 kDa PEG is comparable to that achieved in previous studies using Ficoll and other larger macromolecules. For example,

Raghunath's group previously showed that a FVO of 8.06% 400 kDa Ficoll in Collagen I gels was enough to alter matrix assembly.(Dewavrin *et al.*, 2014) Using the same FVO calculation we estimate that we achieve a 4.63% FVO with 10 mg mL^{-1} of 8 kDa PEG, the maximum concentration of PEG used in our matrix engineering experiments. We calculated FVO using the hydrodynamic radius of PEG 8000 as 2.45 nm.(Kuznetsova et al., 2014) The hydrodynamic radius is the preferred measurement when considering excluded volume effect of soluble macromolecules.(Rashid *et al.*, 2014) However, it is also important to note that we use a higher concentration of collagen in our gels (2.5 mg mL^{-1}) than was used in previous reports (0.8 mg mL^{-1}), which is expected to contribute to self-crowding of the collagen.(Dewavrin *et al.*, 2014) These observations suggest that when MMC is used for 3D ECM architecture tuning, MMC size and FVO as well as ECM molecule size and FVO should be considered in an application-dependent manner. PEG and other MMCs have also been used as precipitating agents and to support deposition of ECM by cultured cells.(Lee *et al.*, 2016) To minimize these effects, which were undesired in our study, we thoroughly removed excess PEG in the collagen gels immediately after polymerization.

Increasing amounts of PEG linearly tuned fibril length until at high PEG concentration, where this trend reversed. The degradability of the matrices also decreased linearly with crowding, then plateaued. Non-linear polymerization effects at high PEG crowding concentrations have also been observed for actin filaments, where bundling is induced when the concentration of PEG exceeds a critical onset value.(Schnauß et al., 2016) Studies have shown that PEG polymers are not always excluded in a way that fits the hard-sphere model of crowding,(Bezrukov et al., 1994) and a wide range of partial exclusion as a function of concentration is possible.(Parsegian et al., 2000) This may explain the non-linear collagen

polymerization behavior we observed at high concentrations of PEG. In addition to concentration, the chemical nature of an MMC agent as well as its size can determine its exclusion from molecular surfaces, so MMC chain size and chemistry could be two additional "tuning knobs" to systematically explore for matrix engineering purposes.

Fibril length and matrix degradability were both linearly and significantly predictive of the degree to which cells were confined by the matrix, as measured by cell circularity index. However, pore size varied irregularly as crowding was increased and was not significantly correlated with cellular confinement. This may appear surprising because another study, which used gelation temperature to modulate collagen architecture, found a linear correlation between pore size and cell confinement.(Wolf *et al.*, 2013) However, this study did not assess whether matrix degradability was also altered as a function of changing gelation temperatures. When modifying collagen architecture through polymerization temperature, pore size and degradability may be covariates. Degradability dictates the cell's ability to modify the matrix and expand the pore size locally with MMPs, making initial pore size quickly irrelevant in a degradable matrix. Degradability is also required for integrin binding on 2D matrix-coated substrates.(Das *et al.*, 2017) If this is true for 3D fibril matrices, then cells may remain rounded in low-degradability matrices because they are unable to adhere, not because of steric confinement by small pores. In future work, we plan to examine how matrix degradability influences cell adhesion in our 3D collagen system.

Our results suggest that in native collagen matrices, degradability is a biomaterial feature that predicts cell confinement and thereby cell fate. These findings are consistent with studies showing that the degradability of synthetic hydrogels directs stem cell fate.(Khetan et al., 2013; Walters & Gentleman, 2015) In our study, the degree of cell confinement induced by matrix

architecture modulated actomyosin contractility and predicted distinct modes of cancer cell migration and gene expression. Single cell migration was favored in non-confining matrices where pMLC was initially high, whereas multicellular migration and morphogenesis was favored in confining matrices where pMLC was initially low. The multicellular chain phenotype we observe in our P6 construct is similar to a phenotype observed in fibrosarcoma and melanoma cells in high density collagen matrices, where individual cell bodies are distinguishable but touching, resembling a pearl necklace.(Haeger et al., 2014; D. O. Velez et al., 2017) However, the fused networks, glands, and lobule structures formed in our P8 and P10 conditions are distinct. Weaver and colleagues previously reported the reversion of a malignant breast cancer cell line into a normal glandular phenotype through the blockade of integrin beta 1 (ITGB1), which inhibits adhesion to the ECM substrate.(Weaver *et al.*, 1997) As discussed above, low degradability matrices could also limit adhesion(Das *et al.*, 2017) and as such could impinge on the same pathways to induce collective morphogenesis behaviors. Interestingly, less degradable forms of collagen I are deposited in many cancers, fibrotic tissues, and during embryogenesis.(Jimenez & Bashey, 1977) This could function to confine cells *in vivo*. Alternatively, physical confinement of cells in a rounded shape could alter the tensegrity of the cell, reducing the activation of cell surface integrins and their affinity for binding ECM.(Coughlin & Stamenović, 1998; Ingber et al., 2014)

We identified that the cell–cell adhesion genes PECAM1, ICAM1, CTNNA1, ITGB4, and ITGB5 were upregulated by breast cancer cells undergoing morphogenesis induced by confining matrices. ICAM1 expression in cancer cells has been correlated with more aggressive tumors and has been shown to mediate survival, migration, extravasation, homing, and metastasis.(Evani et al., 2013; Huang et al., 2004; Schröder et al., 2011) However, it is not fully

understood how ICAM1 expression is regulated in cancer.(G.-S. Park & Kim, 2015) Our study shows that 3D collagen architecture regulates ICAM1 expression. Confining architectures likely induce this gene expression program through the alterations to actomyosin contractility that we observed,(Aragona et al., 2013; Bao et al., 2017; Dupont et al., 2011; Halder et al., 2012; Ingber et al., 2014; Wada et al., 2011) however more work is necessary to identify the molecular mechanisms.

It will also be important to identify what drives the development of the heterogeneous structures formed by the breast cancer cells in our system and whether these represent different metastatic capabilities. The more abundant network phenotype we observe is reminiscent of the collective migration pattern implicated as the primary mode of tumor cell dissemination.(Gaggioli et al., 2007; Y. Kang & Pantel, 2013) This collective invasion behavior is thought to be linked to circulating tumor cells that are present as aggregates, which are predictive of poorer clinical outcomes.(Braun & Naume, 2005; Hou et al., 2012; D. O. Velez et al., 2017) Thus, collagen architecture and confinement in the tumor microenvironment may influence the metastatic capabilities of cancer cells through modulation of migration phenotype and cell–cell adhesion protein expression.

1.4 Conclusions

MMC is a robust technique to modify collagen fibril architectures in 3D hydrogels. Here we built on previous studies to develop an MMC technique for tuning 3D collagen architecture without significantly altering stiffness. This led us to discover an association between matrix degradability and cellular confinement, leading to low actomyosin contractility and cellular reprogramming into a collective morphogenesis phenotype. We propose that MMC-mediated

modification of collagen fibrils represents a powerful biomaterials technique to develop physiologically relevant *in vitro* models to study cancer cell biology.

A deeper understanding of the microenvironmental regulators of cancer cell migration could help identify therapies to combat metastasis and improve patient outcomes. By tuning collagen architecture in a way that decouples matrix architecture from density and stiffness, our study adds support for the strong role of ECM degradability and cellular confinement in modulating cancer cell behavior. The same techniques could be extendable to investigations of metastatic migration *in vivo*, since our 3D matrix constructs are implantable. These techniques may also be useful for stem cell and regenerative medicine studies as a means to control 3D morphogenesis outcomes in a native ECM.

1.5 Methods

1.5.1 Cancer cell culture

MDA-MB-231 breast cancer cells were ordered from ATCC (Manassas, VA) and cultured in Dulbecco's Modified Eagle's Medium (Life Technologies, Carlsbad, CA) supplemented with fetal bovine serum (Corning, Corning, NY) and gentamicin (Life Technologies, Carlsbad, CA), at 37 °C and 5% CO_2. Culture media was changed every other day as needed. Cells were cultured to 80% confluence prior to being trypsinized and embedded inside of 3D collagen I matrices at a seeding density of 50 000 cells per gel. Cell laden gels were cultured for a week to observe long-term phenotypic differences, with media changes every other day.

1.5.2 3D culture in collagen I matrix

High concentration, rat tail acid extracted type I collagen was ordered form Corning (Corning, NY). MMC agent PEG 8000 (8000 Da) was ordered in powder form from Sigma-

Aldrich (St Louis, MO) and reconstituted in PBS (Life Technologies, Carlsbad, CA) immediately before usage. Trypsinized cells to be embedded, were first mixed with 1× reconstitution buffer composed of sodium bicarbonate, HEPES free acid, and nanopure water. Appropriate amounts of MMC agent were then added to produce final concentrations of 0, 2, 4, 6, 8, and 10 mg ml^{-1} PEG (denoted by P0, P2, P4, P6, P8, P10). Afterwards, collagen solution was added to the mixture for a final concentration of 2.5 mg ml^{-1} collagen. Finally, pH of the final mixture was adjusted using 1 N sodium hydroxide, prior to polymerization *via* incubation at 37 °C (∼1 h). Gels were prepared inside of 48-well plates with a total volume of 200 µl. Following gel polymerization, MMC molecules were washed out of the collagen gels by rinsing with PBS 3× for 5 min each. Cell culture media was then added on top of the gels and changed every two days.

1.5.3 Turbidimetry assay

Collagen I turbidimetric analyses were performed as done by Dewavrin *et al.* Solutions of collagen I were prepared at 2.5 mg ml^{-1} with and without the addition of 10 mg ml^{-1} PEG, and immediately transferred to a 96-well plate pre-heated to 37 C for polymerization in a Tecan Infinite 200 Pro (Tecan, Männedorf, Switzerland) at the stem cell core of Sanford Consortium of Regenerative Medicine (La Jolla, CA). The plate temperature was maintained at 37 C for 600 seconds (until the plateau phase was established) while absorbance was recorded every 7 seconds at 313 nm. Lag time before nucleation was calculated as the *x*-intercept of a line tangent to the linear growth phase ($R^2 = 0.99$).

1.5.4 Degradation assay

In order to measure degradation by matrix metalloproteinase 8 (MMP8), 3D Collagen I-DQ matrices were formulated as previously described. Recombinant human MMP–8 (rhMMP-8)

(R&D Biosystems, Catalog #908-MP) was activated at 100 μg mL^{-1} with 1 mM *p*-aminophenylmercuric acetate (APMA) (Sigma, Catalog #A-9563) in TCNB Assay Buffer at 37 °C for 1 hour. Following incubation, activated rhMMP-8 was diluted to 1.0 ng μL^{-1} in TCNB assay buffer and was added on top of each of the gels to a final concentration of 0.45 μg mL^{-1}. Immediately after MMP8 exposure, fluorescence was measured using a Tecan Infinite 200 Pro (Tecan, Männedorf, Switzerland) at the stem cell core of Sanford Consortium of Regenerative Medicine (La Jolla, CA). Fluorescence was measured at excitation (488 nm) and emission (525 nm) wavelengths over a kinetic cycle of 13 hours, with 2-minute intervals.

1.5.5 MMC control experiments

To ensure that the MMC agent PEG was truly inert, we investigated its potential effects separate from changes in matrix architecture. For these experiments, MDA-MB-231 cells were embedded inside of 2.5 mg ml^{-1} collagen gels. After the gels were polymerized, culture media containing 10 mg ml^{-1} PEG was added on top. The MMC molecules were left in the media and allowed to diffuse down into the gel containing the cells. Subsequent media changes also included appropriate amounts of MMC agent to maintain the PEG and concentration in the gel for the week-long experiment.

1.5.6 Time lapse imaging microscopy

Time lapse microscopy was conducted using a Nikon Ti-E inverted microscope, equipped with a stage top incubation system. Time-lapse imaging began at around the 8^{th} hour after the cells were embedded into the collagen gels. For motility, proliferation, and circularity analyses, each gel was imaged at 10× over 6 fields of view (FOV) for a period of 15 h, with images being taken every 2 min.

1.5.7 Cell proliferation assay

Cell viability was assessed using a Live and Dead Cell Assay (Abcam, Cambridge, UK). Intact, viable cells fluoresce green (imaged under FITC channel) while dead cells fluoresce red (imaged under TRITC channel). The average number of live cells, dead cells, and live cell viability percentages were calculated over 4 FOVs per condition. Live cell viability % is defined as the number of live cells/the total number of cells × 100.

1.5.8 Confocal reflection microscopy and matrix analysis

Collagen matrix architecture and topography were investigated by imaging gels using confocal reflection microscopy (CRM) with a Leica SP5 inverted confocal microscope. The microscope was equipped with a 20× immersion objective (NA = 1.0). Collagen fibrils were imaged by exciting with and collecting backscattered light at 488 nm. Confocal reflection imaging is restricted to fibrils that are oriented within 50° of the imaging plane.(Jawerth *et al.*, 2010)

All matrix analyses were done using CRM images (fiber length and pore size) and SEM images (fiber width) of the collagen gels in each condition over 3 FOVs per biological triplicate. Fibril analysis was conducted in CT-FIRE v1.3 by measuring individual fibril length and width as previously published.(Bredfeldt *et al.*, 2014) Minimum fibril length, dangler length threshold (thresh_dang_L), short fibril length threshold (thresh_short_L), distance for linking same-oriented fibrils (thresh_linkd), and minimum length of a free fibril (thresh_flen), were all set to three pixels. Default settings were used for all other fibril extraction parameters and output figure controls. Settings were optimized to detect and analyze discrete fibrils in CRM images on scales of 0.72 μm per pixel. Examples of the fibrils found by CT-FIRE are shown in Supplementary Fig. 1.3D, along with the associated reflection confocal micrographs.

Pore size was calculated using NIS-Elements software (Nikon) as the 2D area encompassed by fibrils. The total pore area (ε') as a 2D approximation of the 3D tissue ultrastructure (ε) can be described as:

$$\varepsilon' = \varepsilon \exp\left(\frac{-\alpha D_{\mathrm{f}}}{4\varepsilon}\right) \quad (1)$$

as long as the stereological assumption is met.(Overby *et al.*, 2001) To verify this assumption, we imaged them from the top and from one of the sides (*XY* and *YZ* planes) using the same imaging settings. Supplementary Fig. 1.3A and B, show that differences in fibril length were negligible. Supplementary Fig. 1.3C shows that a small difference in pore size was detected (<0.5 μm^2 difference). However, this difference is less than the pixel size (0.52 μm^2 per pixel).

Additionally, if the imaging depth of field (D_f) is small enough $\varepsilon' = \varepsilon$. We calculate our D_f from:

$$D_{\mathrm{f}} = \frac{\lambda n}{\mathrm{NA}^2} + \frac{n}{M \cdot \mathrm{NA}} e \quad (2)$$

to be ~0.67 microns. This is smaller than the pixel size in our system and smaller than the expected ε, which makes the fraction in eqn (1) <1 and suggests that $\varepsilon' \cong \varepsilon$ is a valid approximation. These analyses suggest that our 2D confocal micrographs are a sufficiently close representation of the 3D architecture.

Pre-processing of images were conducted by implementing a Gauss-Laplace Sharpen set to a power of 2 and then by using a Rolling Ball Correction with a rolling ball radius of 15.(Haidekker, 2011) The contrasts of all images were equalized, then images were binarized by thresholding to the same range. Next the automated measurement tool was used to measure pore

areas in the binarized images. Single pixel pore values were attributed to speckle noise and removed from all conditions.

1.5.9 Rheometry

Rheological measurements were conducted following established protocols(Fraley *et al.*, 2015) using a hybrid rheometer (DHR-2) from TA Instruments (New Castle, DE). 610 μL PEGylated collagen gels were measured on a cone and plate geometry with a 53 μm gap. Gels were allowed to polymerize in contact with the cone and plate in a humidified incubation chamber for 30 minutes at 37 °C before measurement. For each condition, a strain sweep at frequency of 1 rad s^{-1} was recorded to determine each gel's viscoelastic region. The storage modulus (G') and loss modulus (G'') were recorded over frequencies of 0.1–100 rad s^{-1} within the linear region (0.8%). The storage modulus (G') at 100 rad s^{-1} was reported for each condition. Three independent replicates were performed for each condition tested.

1.5.10 Atomic force microscopy (AFM)

AFM was performed to measure local collagen gel stiffness as previously described.(Engler et al., 2007; Engler, Richert, et al., 2004; Radmacher et al., 1995; Richert et al., 2004) Briefly, nano-indentations were performed using a MFP-3D Bio Atomic Force Microscope (Oxford Instruments) mounted on a Ti-U fluorescent inverted microscope (Nikon Instruments). A pyrex-nitride probe with a pyramid tip (nominal spring constants of 0.08 N m^{-1}, 35° half-angle opening, and tip radius of 10 nm, NanoAndMore USA Corporation, cat # PNP-TR) was first calibrated for the deflection inverse optical lever sensitivity (Defl InvOLS) by indentation in PBS on glass followed by using a thermal noise method provided by the Igor 6.34A software (WaveMetrics) as previously described.(Radmacher et al., 1995) Samples were loaded on the AFM, submersed in phosphate buffered saline (PBS), and indented at a velocity of

2 μm s^{-1}. Samples were indented until the trigger point, 2 nN, was achieved. Five measurements, equally spaced 50 μm apart, were taken per gel. Tip deflections were converted to indentation force for all samples using their respective tip spring constants and Hooke's Law. Elastic modulus was calculated based on a Hertz-based fit using a built-in code written in the Igor 6.34A software. The Hertz model used for a pyramidal tip is:

$$F = \frac{2}{\pi}\tan(\alpha)\frac{E}{1-\nu^2}\delta^2 \quad (3)$$

where F is force, α is the half-angle opening of the tip, ν is the Poisson's ratio, E is elastic modulus and δ is indentation. We assumed a Poisson's ratio of 0.5 (incompressible) for all samples. Curves were only analyzed if at least 80% of the fit curve crossed over the data points. Supplementary Fig. 1.4A shows force-position plots of raw data where the calculated indentation points are indicated and aligned between soft (blue) and stiff curves (red). When the indentation force trigger was met, *e.g.* when the probe is centered over a pore, data is not collected. Supplementary Fig. 1.4B plots an example of the force curve (orange) that would be obtained from a pore, noting that there is no calculable contact point and tip deflection is only the result of drag on the cantilever during tip approach.

1.5.11 Scanning electron microscope (SEM)

Collagen gels were prepared at 2.5 mg mL^{-1} concentration with and without the addition of 10 mg mL^{-1} 8 kDa PEG, then placed in a humidified incubator (37 °C) until fully polymerized as described above. The samples polymerized in the presence of PEG were separated into washed and not washed preparations. To wash the PEG after polymerization, PBS was added on top of the gel and placed in the incubator for 5 minutes 3 times. Next, all samples were fixed with 4% PFA for 1 hour at room temperature and the washed 3× with PBS. The samples were then dehydrated by treating them with increasing concentrations of ethanol (50% to 100%).

Samples immersed in 100% ethanol were subjected to critical point drying (Autosamdri-815, Tousimis, Rockville, MD, USA), coated with a thin layer of Iridium (Emitech K575X, Quorum technologies, Ashford, UK) and imaged using a Zeiss sigma 500 SEM. Gels were cut with a razor blade to expose cross-sections of the material for imaging.

1.5.12 Diffusivity analysis

To analyze the penetration of the PEG crowding agent into the 3D collagen matrices, we conducted diffusion experiments through gels polymerized in microchannels (μ-Slide VI 0.4, IBIDI, Munich, Germany). Collagen gels were prepared as described above and polymerized inside the microchannel for 1 hour at 37 °C. Subsequently an 88 μM solution of 70 kDa fluorescein-conjugated dextran or a 0.31 mM solution of fluorescein-conjugated 8 kDa PEG were added to one end of the microchannel while the equivalent volume of cell growth medium was added to the other end. The microchannel was then imaged in a fluorescent microscope at 1 min intervals for 8.5 hours to track the solute diffusion through the collagen matrix. Images were analyzed using ImageJ and a concentration profile was determined for each time point. The data was fitted to Fick's Second Law for 1-D diffusion (eqn (4)), and the diffusion coefficient, D, was determined for runs with an R-squared value of greater than or equal to 0.90.

$$C(t,X) = C_{\max} \times \left(1 - \operatorname{erf}\left(\frac{X}{2\sqrt{Dt}}\right)\right) \tag{4}$$

where $C_{\max}$ is the initial concentration at the source, erf is the error function, X is length, and t is time.

1.5.13 Cell analysis

Individual cells in the time lapse videos were tracked in Metamorph for motility characterization. Within the 15 h time lapse window, cells were analyzed in terms of the total path length traveled, their average speed, the invasion distance (displacement), and the

persistence of their migration (defined as the invasion distance/the total path length traveled). Cell morphology analysis was conducted using images of the cells during the 11th and 15th hour after seeding in the gel, in terms of circularity:

$$\text{Circularity} = \frac{4\pi A}{P^2} \quad (5)$$

where A is the cross-sectional area and P is cross-sectional perimeter of the cell.

1.5.14 Correlation analysis

Correlations were calculated in terms of the Pearson correlation coefficient using GraphPad software.

1.5.15 RNA isolation and purification

Three independent replicates of 3D collagen I gels were seeded at 50 000 cells per gel per condition tested. RNA was harvested after 7 days by gel homogenization in TRIzol reagent (Thermofisher, Waltham, MA). Total RNA was isolated using a chloroform extraction according to manufacturer's instructions. RNA was subsequently purified using High Pure RNA Isolation Kit (ROCHE, Branford, CT).

1.5.16 Gene expression analysis by qPCR

Following the RNA extraction, cDNA was synthesized using the SuperScript III First-Strand Synthesis System (Thermofisher, Waltham, MA). The TaqMan Array Human Extracellular Matrix & Adhesion Molecules 96-well Plate was utilized to identify genes of interest (Thermofisher, Waltham, MA). Relative mRNA levels were quantified by calculating the ΔCt using ACTB as a reference gene.

1.5.17 Statistics

Data presented in bar graph format was analyzed using one-way analysis of variance (ANOVA) followed by Tukey or Newman–Keuls *post hoc* test in GraphPad Prism (v5).

Correlation plots were analyzed by Pearson Correlation in GraphPad Prism (v5). Pearson *r* correlation coefficient and two-tailed *p* values are reported. $N = 3$ biological replicates for each condition tested. Statistical significance was reported as $p < 0.001$, ***; $p < 0.01$, **; $p < 0.05$, *.

1.5.18 Western blotting from 3D constructs

200 µL 3D collagen constructs were scooped out of their wells into vials containing 1 mL of PBS and immediately spun down at 1500*g* for 5 min. Supernatant per vial was discarded and 200 µL of Pierce IP Lysis Buffer containing proteases and phosphatase inhibitor cocktails was added to the pellets (Thermofisher Scientific, Waltham, MA). Loading buffer containing SDS and DTT was added to achieve a final 1× concentration. The samples were then sonicated on ice for 30 s, then boiled at 95 C for 5 min. Proteins were separated by SDS-PAGE and transferred to a PVDF membrane. Membranes were then probed with antibodies against phosphorylated myosin light chain (Cell Signaling Technology, Danvers, MA) and alpha Tubulin (TU-01, Thermofisher).

1.5.19 Data availability

All relevant data is available within the article and supplementary files, or from the corresponding author upon request.

1.6 Supplementary Material

1.6.1 Supplementary Figures

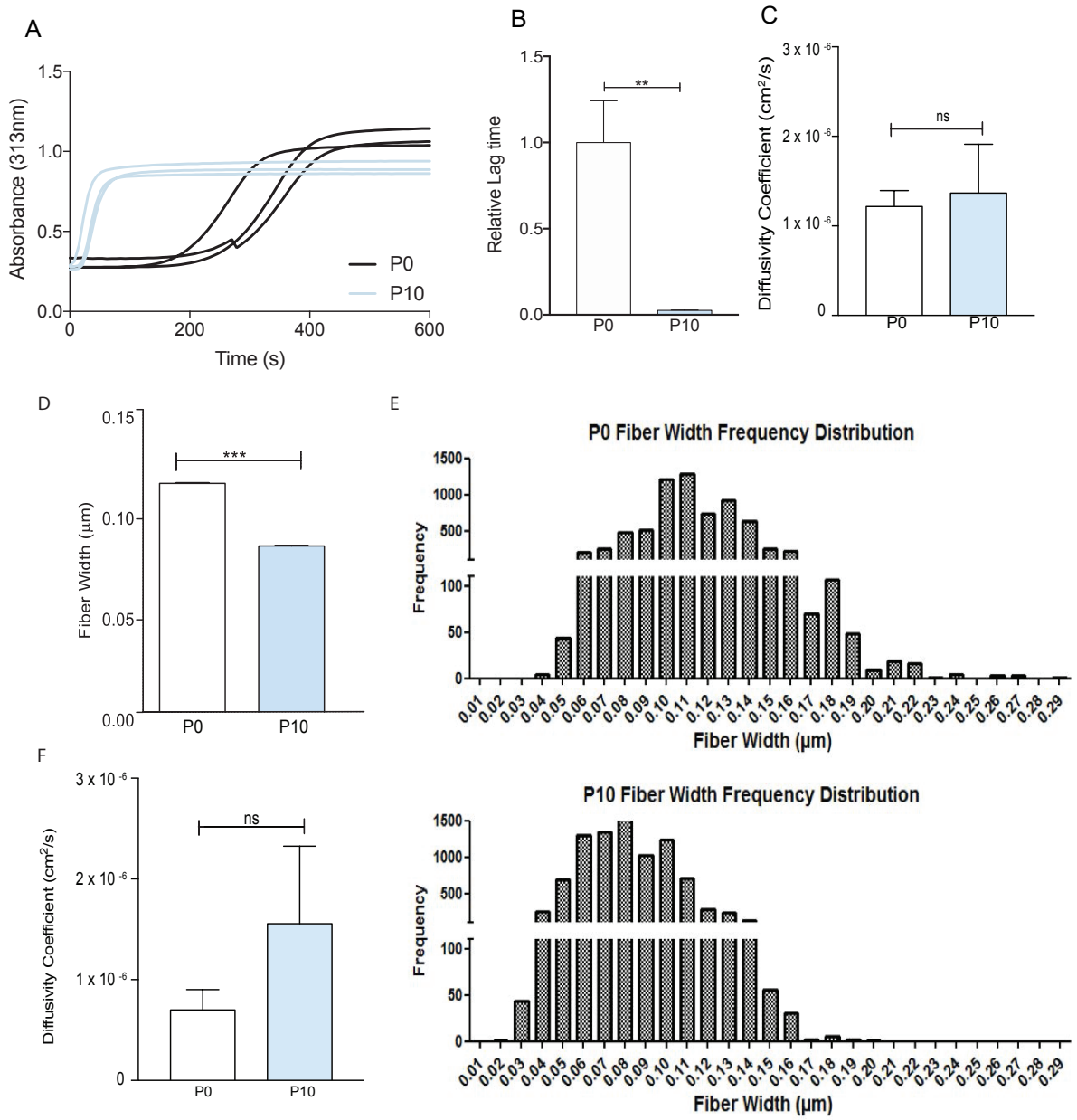


Figure 1.6: Supplementary Figure 1.1. (a) Collagen assembly as shown by turbidimetry (b) Relative lag time before Collagen nucleation of 2.5 mg/ml gels with and without 10 mg/ml PEG added before polymerization (c) Diffusivity of fluorescently labeled PEG through 2.5 mg/ml gel and 2.5 mg/ml gel with 10 mg/ml PEG. (d) Average width of collagen fibers in 2.5 mg/ml collagen polymerized without a molecular crowding agent, P0, and with 10 mg/ml of PEG as a crowding agent added during polymerization, P10. Widths measured by analysis of scanning electron microscopy. (e) Histogram of fiber width measurements in the P0 and P10 conditions show overlapping distributions. (f) Diffusivity of fluorescent dextran through 2.5 mg/ml gel and 2.5 mg/ml gel with 10 mg/ml PEG.

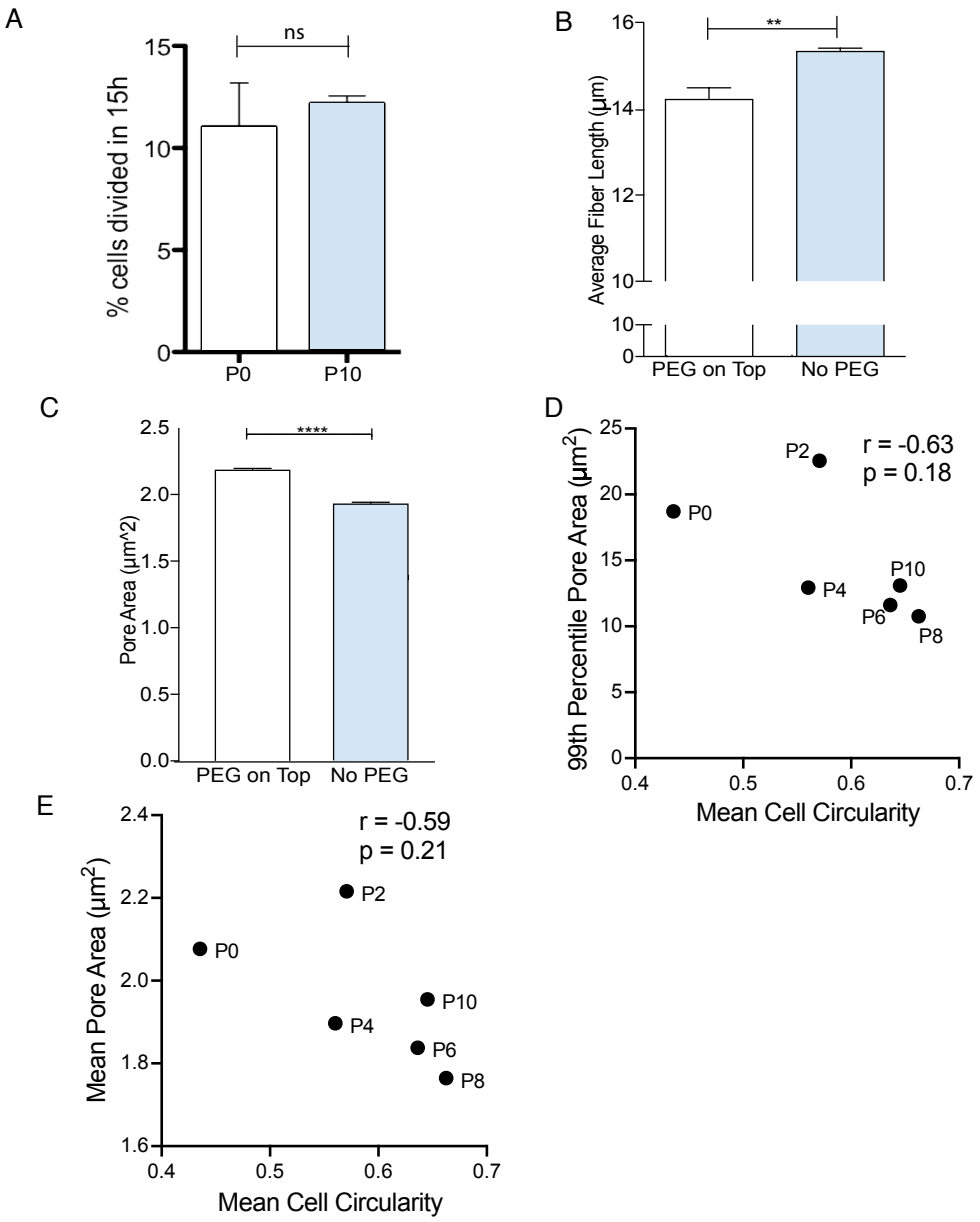


Figure 1.7: Supplementary Figure 1.2. (a) Percent of cells that underwent division during the first 15 hours of culture in the P0 and P10 conditions. (b) Mean fiber length in 2.5 mg/ml and 2.5 mg/ml with 10 mg/ml of PEG added on top after polymerization. Lengths measured by analysis of reflection confocal micrographs. (c) Pore size in 2.5 mg/ml and 2.5 mg/ml with 10 mg/ml of PEG added on top after polymerization. Pores measured by analysis of reflection confocal micrographs. It is important to note that the large number of pores and fibrils analyzed tends to generate statistical significance between conditions, even when differences are small34. (d) The 99th percentile of pore sizes and (e) mean of all pore sizes plotted against mean cell circularity in each matrix condition. N=3 replicates for each condition. At least three fields of view were analyzed per replicate. At least 300 cells were analyzed in each condition. Bar graphs show the mean and standard error of measurements. Statistical significance tested by ANOVA and reported as $p<0.001$, ***; $p<0.01$, **; $p<0.05$, *.

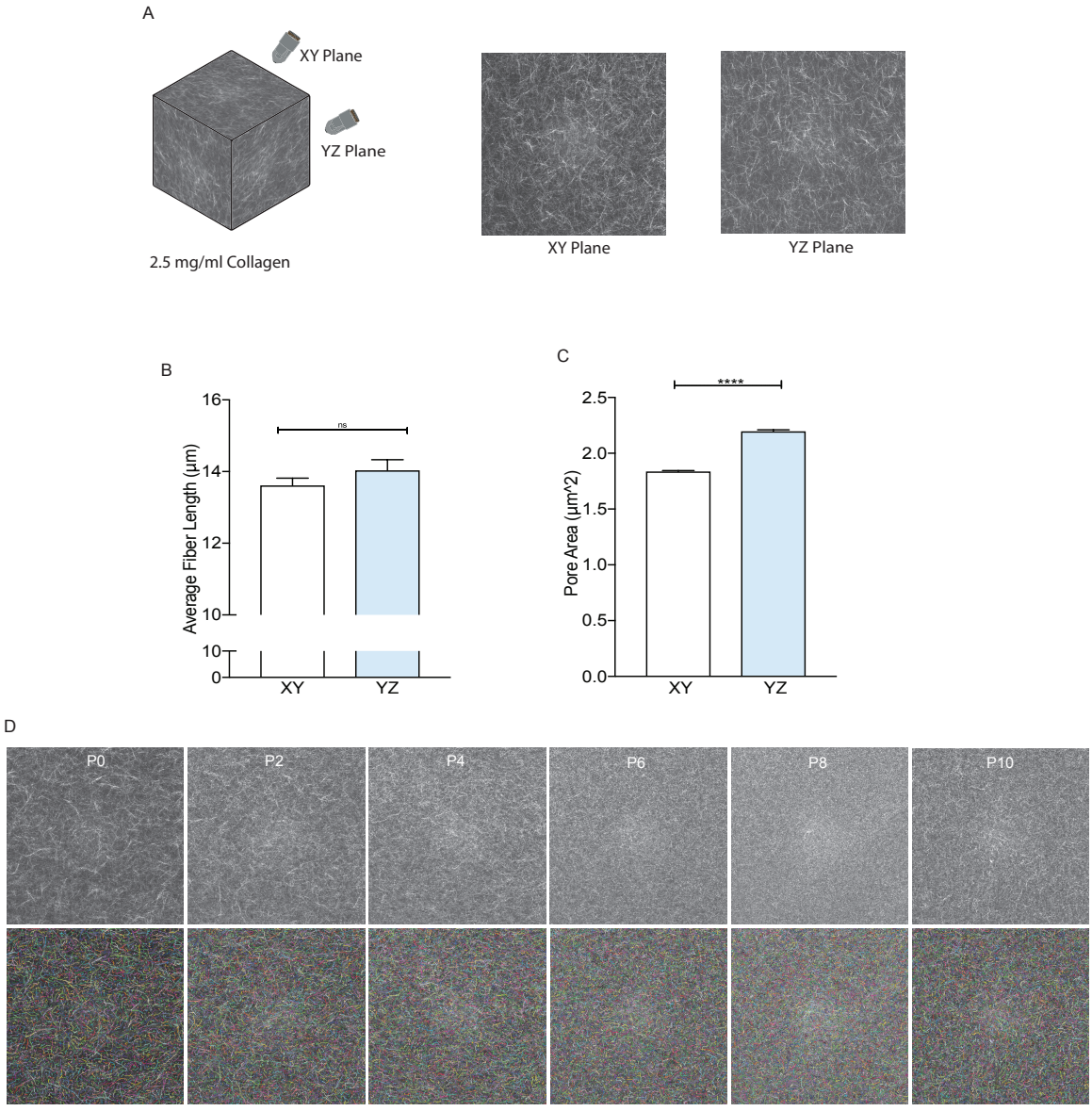


Figure 1.8: Supplementary Figure 1.3. (a) Reflection confocal micrographs of the X-Y plane and Y-Z plane of 2.5 mg/ml collagen polymerized without a molecular crowding agent. Characterization of (b) mean fiber length and (c) pore size as a function of orientation. (d) Visual overlay of fiber analysis conducted in CT-FIRE. N=3 replicates for each condition. At least three fields of view were analyzed per replicate. Bar graphs show the mean and standard error of measurements. Statistical significance tested by ANOVA and reported as $p<0.001$, ***; $p<0.01$, **; $p<0.05$, *.

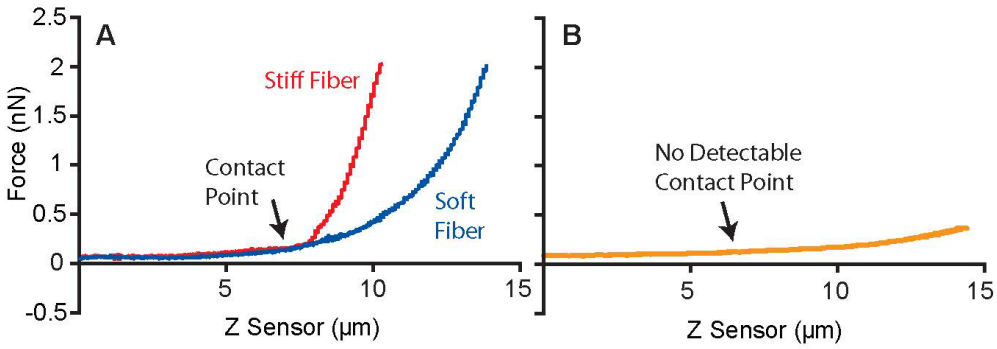


Figure 1.9: Supplementary Figure 1.4. AFM measurements of local fibril stiffness. (a) Force-position plots of raw data where the calculated indentation points are indicated and aligned between soft (blue) and stiff curves (red). When the indentation force trigger was met, e.g. when the probe is centered over a pore, data is not collected. (b) An example of the force curve (orange) that would be obtained from a pore, noting that there is no calculable contact point and tip deflection is only the result of drag on the cantilever during tip approach.

1.7 Acknowledgements

This chapter is a partial reprint of "Macromolecular crowding tunes 3D collagen architecture and cell morphogenesis" as it appears on *Biomaterial Sciences*, 7(2), 618-633. (2019). Ranamukhaarachchi, S. K., Modi, R.N., Han, A., Velez, D.O., Kumar, A., Engler, A.J., Fraley, S.I. Macromolecular crowding tunes 3D collagen architecture and cell morphogenesis. The dissertation author was the primary investigator and co-first author of this paper.

We thank Dr Pedro Cabrales for use of his rheometer. We thank members of the Fraley lab for their technical assistance and insightful comments regarding this work. We thank NSF REU student Tyler Goshia for his assistance in preliminary studies of collagen crowding.

S. F. and lab is supported by a Burroughs Wellcome Fund Career Award at the Scientific Interface (1012027), NSF CAREER Award (1651855), ACS Institutional Research Grant (15-172-45-IRG) provided through the Moores Cancer Center, UCSD, and UCSD CTRI, FISP, and CRES pilot grants. Support was also provided by NIH grants (R01CA206880 to A. J. E.) and by fellowship support *via* NSF GRFP and NIH T32AR060712 (to A. K.).

CHAPTER 2

Distinct matrix remodeling programs drive divergent cell polarization and collective migration modes

2.1 Introduction

Exocrine organs, such as the mammary, salivary, and digestive glands, are composed of suprastructural networks of terminal acini connected to secretory ducts. During glandular organogenesis, epithelial cells undergo collective migration to develop these core subunits, which are described according to their shapes, ranging from round spherical acinar structures to elongated linear or branched ductal structures. Specific collective migration behaviors shape these distinct suprastructures: acini are developed by a persistent coordination of rotational movement while ductal structures are developed by invasive collective movements such as sprouting or branching(Ewald *et al.*, 2008; Tanner *et al.*, 2012; Wang *et al.*, 2013). Furthermore, developmental processes such as lactation and involution of the mammary gland require rapid transformations between these tubular ducts and spherical acinar structures, which require epithelial cells to switch between modes of invasive (ICM) and rotational collective migration (RCM), respectively.(Fernández et al., 2021; Inman et al., 2015) Similar transformations are conserved in developmental programs such as *Drosophila* egg tissue elongation, where switching from rotational to invasive collective migration is a part of normal maturation(Cetera et al., 2014; Haigo & Bilder, 2011; Popkova et al., 2020). Neoplastic epithelial cells can also mimic and aberrantly activate collective migration programs during cancer progression. A prominent manifestation is the hijacking of ICM by neoplastic cells, which can exhibit relatively normal-appearing epithelial architectures with or without expression of cell-cell adherens junctions during collective invasion(Ewald *et al.*, 2008). Interestingly, RCM has not been directly

observed in neoplastic epithelial cells, which has been attributed to their loss of E-Cadherin-based adherens junctions.(Tanner *et al.*, 2012; Wang *et al.*, 2013) However, acinar cell carcinomas of the breast and salivary gland are characterized by an acinar-like morphological arrangement and indolent clinical behavior, which suggests that it is conceivable and possibly favorable for neoplastic cells to undergo RCM.(Conlon et al., 2016; Piscuoglio et al., 2015) Along these lines, we previously made an intriguing observation that within a population of triple-negative breast cancer (TNBC) cells, some cells form structures resembling rounded acinar-like morphologies and others form elongated ductal-like morphologies when seeded in confining, high-density collagen type I.(K. Chen et al., 2021; Ranamukhaarachchi et al., 2019; D. O. Velez et al., 2017; Daniel O. Velez et al., 2019) Here, we use this model system to investigate the migration behaviors and fundamental interactions that give rise to these structures.

While collective movements are diverse and complex, their emergence is thought to arise from the interplay of cell-cell and cell-matrix interactions that is dependent on the position of cells within the collective, as well as the constraints imposed on the cells by the extracellular environment. Our current understanding emphasizes that ICM and RCM programmes are initiated by first establishing a collective front-rear polarity through coordination of the actin cytoskeleton.(Cetera et al., 2014; Glentis et al., 2022; S. Jain et al., 2020) RCM in normal epithelial cells requires strong intercellular cadherin junctions for polarity and movement initiation, while ICM can be orchestrated by polarized cells of higher junctional fluidity.(Friedl et al., 2012; S. Jain et al., 2020) Collective movements also respond to contractile stresses from the matrix. Invasive ductal cells seeded in 3D collagen sense and reinforce anisotropic stress from the extracellular matrix (ECM) during elongation but will initiate rotational migration to

establish terminal acini when tension anisotropy is decreased due to gel detachment(Fernández *et al.*, 2021). Movement within a physically confining ECM also requires actively transforming the surrounding matrix through proteolytic degradation or physical disruption. Proteolytic remodeling, specifically, has been well-studied in the context of ICM, where cells generate macroscopic holes in the matrix by proteolytic removal to direct migration using matrix metalloproteinases (MMPs), such as MMP-14.(Wolf *et al.*, 2007) Physical remodeling, which occurs through bundling or breakage of the matrix, has been observed in protease-independent collectively migrating invasive and rotational cells, but whether it plays a direct role in shaping these core glandular subunits remains largely undefined.(Fernández et al., 2021; Gaggioli et al., 2007) In this study, we use computational modeling and experiments to conduct a comprehensive investigation of how cell-cell and cell-matrix interactions converge to direct ductal versus acinar morphogenesis in both normal and neoplastic epithelial cells through regulation of ICM and RCM.

2.2 Results

2.2.1 RCM and ICM emerge in confining ECM

Neoplastic MDA-MB-231 cells seeded sparsely as single cells in high density collagen type I (6mg ml^{-1}) form clonal structures resembling either elongated duct-like structures or rounded acinar-like structures over the course of 7 days (Fig. 2.1a-c).(K. Chen et al., 2021; Ranamukhaarachchi et al., 2019; D. O. Velez et al., 2017; Daniel O. Velez et al., 2019) We wondered whether ICM and RCM behaviors contributed to the formation of these two structure types. RCM of MDA-MB-231 cells would be particularly surprising given that they do not express E-cadherin (Fig. 2.1d). To link the structures formed at 7 days to early cell migration behaviors, we first imaged cells after ~1 cell division cycle from day 2 through day 7 after

seeding and quantified differences in cluster circularity. By applying a circularity threshold of <0.6 for ductal-like phenotypes and >0.8 for acini-like phenotypes, we found that we could distinguish the phenotypes at early time points based on cellular shapes (Fig. 2.1e). Importantly, elongated cells remained elongated and circular cells remained circular (Fig. 2.1f). In stable cell lines expressing GFP-tagged LifeAct (to visualize the actin cytoskeleton) and mCherry-tagged H2B (to visualize nuclei), we tracked circular and elongated cells every hour for 10 hours at this early 2-cell stage. Live imaging of circular MDA-MB-231 cells revealed active rotations that persisted as cells divided and entered 3- and 4- cell clusters (Fig 2.1g-i, Supplemental Video 2.1-2.2). This finding was rather surprising, as previous work has suggested an inability for neoplastic cells to undergo collective coherent angular rotations.(Tanner *et al.*, 2012; Wang *et al.*, 2013) These cells did not exhibit a directional bias, and occasionally switched chirality. To exclude the possibility that rotational cells were simply undergoing directionless oscillations, we measured the migration coherence using a previously established cell persistence ratio(S. Jain et al., 2020). This metric quantified the proportion of time that cells migrated consistently in a clockwise (CW) or counterclockwise (CCW) radial direction such that a value of 0 or 1 indicated no directionality or completely CW/CCW, respectively. Population-level analysis confirmed that rotational cells migrated coherently (Fig. 2.1j). Conversely, elongated cells collectively invaded, which continued through the 3- and 4- cell stages (Fig 2.1k-m, Supplemental Video 2.3-2.4). The paths of invasively migrating cells were not directionally cohesive, as leader cells intercalated often in an unjammed phase while continuously progressing the invasion front, as has been previously observed with the MDA-MB-231 cell line.(Zhang *et al.*, 2019) The non-cohesive migration of these collectively invading cells is reminiscent of prior observations of reduced next-neighbor coordination in multicellular movements when E-cadherin expression is

diminished.(Ilina *et al.*, 2020) We similarly measured a rectilinear persistence ratio for invasive cells, which quantified the proportion of time cells migrated consistently without changing direction (<90º from previous direction). Population-level analysis showed that invasive cells changed direction more often than rotational cells (Fig. 2.1n).

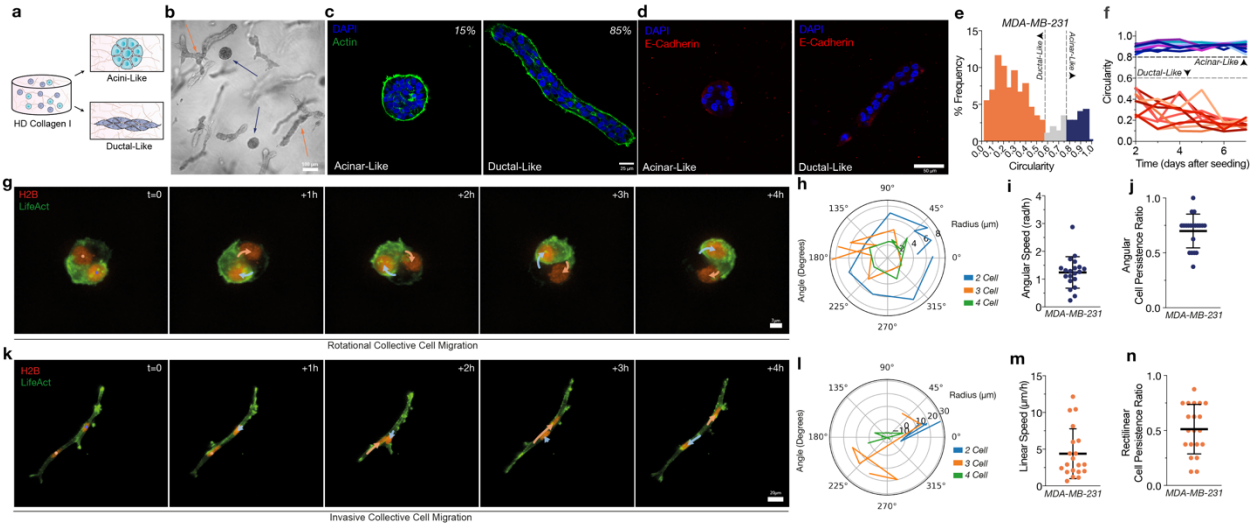


Figure 2.1. RCM and ICM emerge in confining ECM. (a) Cells seeded sparsely as single cells in high density collagen type I (6mg ml^{-1}) form clonal structures resembling either elongated ductal-like structures or rounded acinar-like structures over the course of 7 days. (b) Brightfield images taken 7d after seeding; Orange arrows indicate ductal-like structures (n = 10) and blue arrows indicate acinar-like structures (n = 10). Scale bar, 100μm. (c) Actin cytoskeleton substructure in acinar-like and ductal-like structures. Scale bar, 25μm. (d) E-Cadherin is not expressed at cell-cell junctions in MDA-MB-231 in either acinar-like or ductal-like structures. Scale bar, 50μm. (e) Frequencies of ductal-like and acinar-like morphologies at 7 days in MDA-MB-231 cell lines. A circularity threshold of <0.6 for ductal-like phenotypes and >0.8 for acini-like phenotypes was applied at 7 days (n=342 multicellular structures). (f) Cells were imaged daily from days 2-7 after seeding and quantified for differences in cluster circularity. Applying a circularity threshold of <0.6 for ductal-like phenotypes and >0.8 for acini-like phenotypes is sufficient to distinguish these phenotypes at early time points (n = 10 acinar-like structures and n = 10 ductal-like structures). (g) Kymograph of circular 2-cell clusters of MDA-MB-231 cells reveals persistent active rotations. Scale bar, 7μm. (h) Active rotations persist for cells in 2-, 3- , and 4-cell clusters. (i) Angular speed of rotational MDA-MB-231 cells in 2-cell clusters (n=20 individual cells, n = 10 cell clusters). (j) Cell persistence ratio for MDA-MB-231 rotational 2-cell clusters (n=20 individual cells, n = 10 cell clusters). (k) Kymograph of elongated 2-cell clusters of MDA-MB-231 cells reveals collective invasion. Scale bar, 20μm. (l) Active invasion persists for cells in 2-, 3- , and 4-cell clusters. (m) Rectilinear speed of invasive MDA-MB-231 cells in 2-cell clusters (n=20 individual cells, n = 10 cell clusters). (n) Cell persistence ratio for MDA-MB-231 invasive 2-cell clusters (n=20 individual cells, n = 10 cell clusters). All error bars represent standard deviation from the mean.

2.2.2 RCM and ICM do not require adherens junctions and are associated with laminin deposition

Prior investigations have indicated a role for adherens junctions in facilitating RCM(Fernández et al., 2021; S. Jain et al., 2020; Rappel et al., 1999; Tanner et al., 2012). As such, it was surprising to observe coherent angular rotations in neoplastic cells that lack cadherin-based junctions (Fig. 2.2a). To assess the generality of our findings, we asked whether both ductal-like and acinar-like morphogenic structures could be formed in our confining collagen system by normal epithelial cells with proper E-Cadherin junctions as well as other neoplastic epithelial cells without such cadherin junctions. We cultured normal mammary epithelial cells (MECs), MCF-10As (Fig. 2.2b), which have high junctional E-Cadherin expression (Fig. 2.2c), and malignant hepatocarcinoma cells, SK-HEP-1s (Fig. 2.2d), which lack any junctional cadherin expression (Fig. 2.2e-f), in high density collagen. After 7 days in culture, we found that both cell lines were able to form ductal-like and acinar-like phenotypes with varying frequencies (Fig. 2.2g-h). In comparison to MDA-MB-231, which predominantly formed the invasive ductal-like phenotype (Fig. 2.1e), SK-HEP-1 and MCF-10A predominantly formed the acinar-like phenotype (Fig. 2.2i-j). Importantly, the early rotational and invasive collective cell migration behaviors were conserved in the SK-HEP-1 cells (Fig. 2.2k-m, Supplemental Video 2.5-2.6). In normal MCF-10a, invasive and rotational collective cell migration have both been previously characterized.(Carey et al., 2017; Chaudhuri et al., 2014; Hiraki et al., 2022; Tanner et al., 2012; Wang et al., 2013) Specifically, collective invasion of MCF10a is directed by leader cells with E-Cadherin based cell-cell junctions, which is distinct from the intercalating invasive migration pattern we observe in the MDA-MB-231s absent of cadherens junctions(Carey et al., 2017). RCM in normal MCF-10a is observed during maturation of acini with central, hollow lumen(Ahmed, 2017; Chin et al., 2018; Tanner et al., 2012; Wang et al., 2013). Interestingly, previous studies have indicated that neoplastic epithelial cells that form

rounded structures are unable to establish lumen-like hollowness due to the inability of these cancer cells to undergo RCM. Therefore, it was surprising to find that a few of the MDA-MB-231 rotational cells mature into a hollow or toroidal acinar morphology with a distinct lumen structure (Fig. 2.2n). These structures cannot be described as "normal" acini, given that they lack the key epithelial adhesion molecule E-Cadherin, but this finding does suggest that cancer cells can mimic normal acinar formation through RCM. Altogether, these data demonstrate that both normal and malignant epithelial cells can undergo either rotational and invasive collective cell migration with and without cadherin-based cell-cell adhesions. Therefore, adherens junctions are not essential for the emergence of complex RCM and ICM behaviors within a confining 3D collagen matrix.

Coherent rotational migration of normal mammary acini has been linked to the establishment of apical-basal polarity through the assembly of an endogenous laminin-rich basement membrane(Wang *et al.*, 2013). Likewise, ICM of normal myoepithelial cells during branching morphogenesis of the mammary gland involves degradation of the existing ECM and the secretion of new basement membrane components to form a secondary ECM around new branches(Gudjonsson *et al.*, 2002). This prompted us to ask whether the assembly of an endogenous laminin-rich basement membrane was associated with or a requirement for either migration phenotype. Laminin-332 is an isoform highly expressed in epithelial basement membranes.(Simon & Bromberg, 2017) Immunostaining analyses of Laminin-332 in the neoplastic MDA-MB-231s at 2 days and 7 days after seeding revealed that both acinar-like and ductal-like structures deposit laminin over the course of a week. This deposition is not a unique characteristic of either migration phenotype (Fig. 2.2o-p), suggesting that laminin deposition is not essential for initiation of either migration phenotype and also indicating that neoplastic cells

can deposit laminin. This finding contradicts a previous report that attributes the inability of neoplastic cells to undergo RCM to their failure to deposit a laminin-rich basement membrane.(Wang *et al.*, 2013)

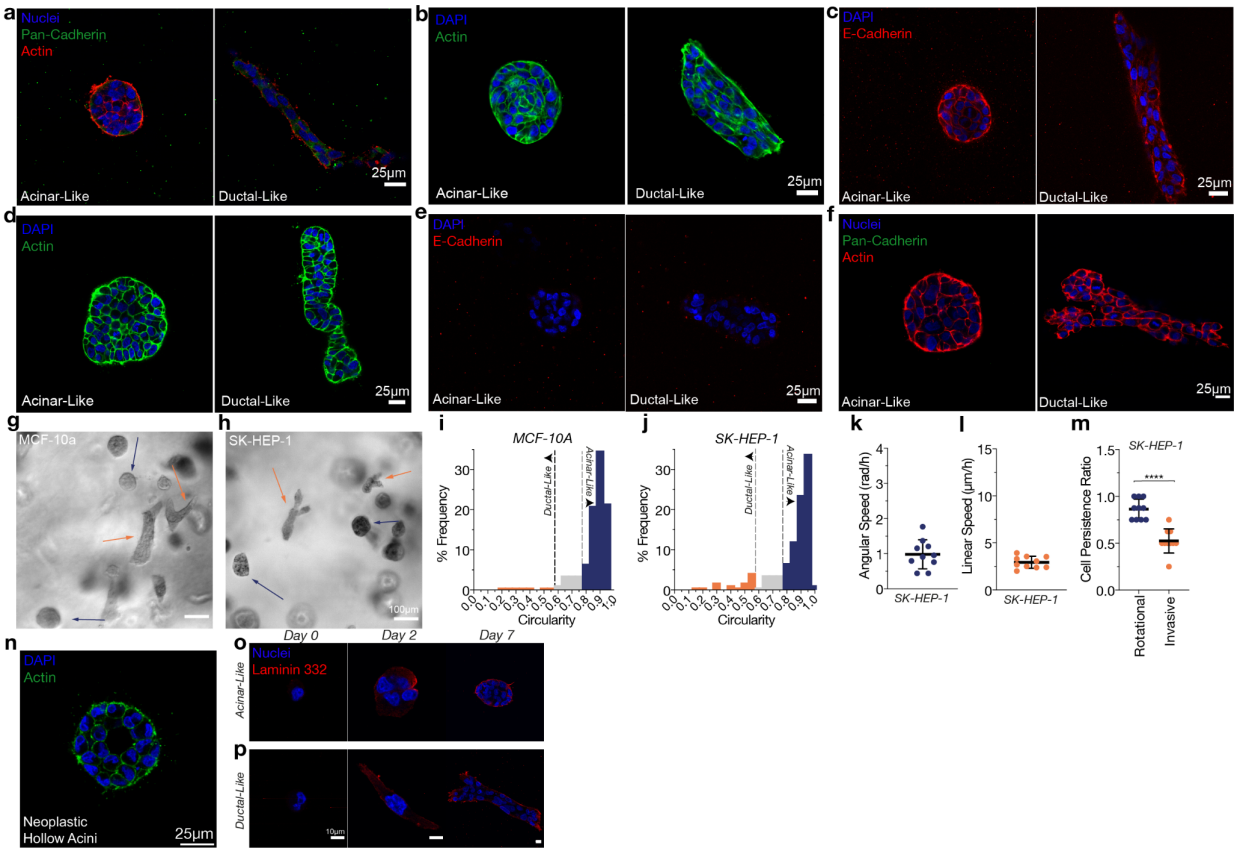


Figure 2.2. RCM and ICM do not require adherens junctions and are associated with laminin deposition. Cadherins are not expressed at cell-cell junctions in MDA-MB-231 in either acinar-like or ductal-like structures, as measured by a pan-cadherin antibody. Scale bar, 25μm. (b) Actin cytoskeleton substructure in MCF-10a acinar-like and ductal-like structures. Scale bar, 25μm. (c) MCF-10A expresses E-Cadherin at cell-cell junctions in both ductal-like and acinar-like phenotypes. Scale bar, 25μm. (d) Actin cytoskeleton substructure in SK-HEP-1 acinar-like and ductal-like structures. Scale bar, 25μm. (e) SK-HEP-1 does not express E-Cadherin at cell-cell junctions in both ductal-like and acinar-like phenotypes. Scale bar, 25μm. (f) Cadherins are not expressed at cell-cell junctions in SK-HEP-1 in either acinar-like or ductal-like structures, as measured by a pan-cadherin antibody. Scale bar, 25μm. Brightfield images taken 7d after seeding for (g) MCF-10a cells and (h) SK-HEP-1 cells; Orange arrows indicate ductal-like structures and blue arrows indicate acinar-like structures. Scale bar, 100μm. Frequencies of ductal-like and acinar-like morphologies at 7 days in (i) MCF-10A (n = 167 multicellular structures) and (j) SK-HEP-1(n = 165 multicellular structures) cell lines. (k) Angular speed of rotational SK-HEP-1 cells in 2-cell clusters (n= 10 individual cells, n = 5 cell clusters). (l) Rectilinear speed of invasive SK-HEP-1 cells in 2-cell clusters (n= 10 individual cells, n = 5 cell clusters). (m) Cell persistence ratio for SK-HEP-1 rotational and invasive 2-cell clusters (n= 10 individual cells per group, n = 5 cell clusters per group). (n) A few MDA-MB-231 mature into a hollow acinar morphology with a distinct lumen structure. Scale bar, 25μm. Laminin-332 is found along the periphery of both (o) acinar-like and (p) ductal-like structures. Scale bar, 10μm. Statistical significance was determined by unpaired two-sided t-test and is indicated as **** for $p \leq 0.0001$. All error bars represent standard deviation from the mean.

2.2.3 A cellular Potts model predicts that RCM and ICM can arise solely from differences in local versus global matrix remodeling

Given the unexpected nature of our findings and the multitude of factors at play in such complex behaviors, we next took a mathematical modeling approach to investigate the emergence of RCM and ICM. Specifically, we sought a modeling framework with which we could ask how cell polarization, cell-cell adhesion, and matrix remodeling can each contribute to the emergence of RCM and ICM in confining ECM conditions. The Cellular Potts Model (CPM) is a computational platform that is particularly versatile in its ability to represent various biological phenomena and incorporate them to examine emergent multicellular behaviors.(Graner & Glazier, 1992) To model cell dynamics, the CPM relies on minimization of the overall energy of the system using the Hamiltonian (H), and in its earliest application, it was used to simulate cell sorting by assuming differential adhesion between different cell types.(Glazier & Graner, 1993; Graner & Glazier, 1992) We built upon these previously described models by incorporating additional terms for cell motility, cell-ECM interactions and proliferation (see Methods for details) (Fig. 2.3a). Notably, we created a cell polarization vector (P) to model polarization of the actin cytoskeleton, where a cell's orientation and propulsion intensity is dependent on the rate of production (k^+) and the rate of degradation (k^-) of the polarization vector. The relationship between the two rates, k^+/k^-, is defined as the polarization persistence (γ), which determines how quickly the direction of the polarization vector is updated. We also defined a matrix-remodeling agent (E) that is active either locally (k_l) in the direction of the polarization vector or globally (k_g) over the whole cell body.

Current dogma suggests that cells require cytoskeletal polarization for ICM and RCM.(Glentis et al., 2022; S. Jain et al., 2020) As such, we first assessed whether varying

polarization persistence while holding all other parameters constant could give rise to both collective behaviors. For this initial simulation, cell-cell ($J_{c,c}$) and cell-ECM($J_{c,e}$) adhesion strengths were set equal, but below the cell-medium interfacial tension ($J_{c,m}$) because setting $J_{c,m}>J_{c,c}$ and $J_{c,m}>J_{c,e}$ is important for matching the cell morphology observed in experimental settings. We also set initial values of local and global degradation constant (k_g=25, k_l=250) at a ratio of 1:100 k_g:k_l to maintain an equivalent initial concentration of matrix-remodeling agent (E) released by k_l and k_g. Our simulations found that in conditions of high polarization persistence ($k^+>k^-$) where the polarization vector degrades slowly, cells migrated linearly and adopted predominantly an ICM behavior (Fig. 2.3b). Conversely, in conditions of lowered γ when degradation ($k^+<k^-$) of the polarization vector dominates, cells changed direction quickly and established RCM. It is important to note that the polarization persistence and local matrix remodeling parameters are coupled, so increasing polarization persistence also increases localized accumulation of the matrix remodeling agent at the tip of the cell. To assess whether varying polarization persistence, in the absence of local matrix degradation, could still give rise to both collective behaviors, we set k_l=0 and k_g=50 to maintain an equivalent initial concentration of matrix-remodeling agent (E) released. Conducting a similar parameter sweep of γ, we found that only RCM could be replicated when k_l was turned off (Fig. 2.3c). In conditions of high polarization persistence ($k^+>k^-$), we now observed that cells failed to exhibit ICM and instead formed rounded non-invasive structures. This suggests that high polarization persistence can give rise to ICM, but only in the presence of localized matrix remodeling. Conversely, RCM

arises at a relatively lower polarization persistence and does not require localized matrix remodeling.

Given these observations, we next investigated whether differences in matrix remodeling play a direct role in directing ICM and RCM behaviors. Selecting a constant polarization persistence in between the two migration behaviors, we systematically varied matrix remodeling parameters (k_g and k_l) and held all other parameters constant. In conditions of high global (k_g) low local (k_l) matrix remodeling, cells underwent RCM and formed acini-like morphologies over the course of 7 day simulations (Fig. 2.3d). Notably, RCM was lost when global matrix degradation was decreased. In contrast, when local remodeling (k_l) took precedence, the cells degraded in the direction of the polarization vector and cellular motion, resulting in ICM behavior and ductal-like morphologies. Quantification of protrusion dynamics from these simulations showed that ICM cells exhibit increased protrusion lifetime as a result of the increased local matrix remodeling (k_l), in comparison to RCM cells (Fig. 2.3e). Together, these simulations predict that ICM and RCM rely on distinct modes of matrix remodeling and that switching from invasive to rotational collective migration requires a shift from local to global matrix remodeling. These findings also suggest that increasing the localization of matrix remodeling can increase protrusion lifetime as well as cell polarization. Lastly, we sought to validate our experimental observation that strong cell-cell junctional strength is not essential for coordinating ICM and RCM. We selected conditions of global (k_g) and local (k_l) remodeling that induced either ICM or RCM and systematically varied the cell-cell adhesion strength ($J_{c,c}$) parameter within the conditions of each respective migration behavior. In agreement with our experimental findings, we found that varying $J_{c,c}$ while holding cell-ECM strength ($J_{c,m}$) and other parameters constant could not inhibit RCM or ICM (Fig. 2.3f). In summary, we found that

our updated CPM model reliably captures the migrational shaping of acini-like and ductal-like morphologies through RCM and ICM, and predicts that distinct modes of matrix remodeling direct RCM and ICM behaviors.

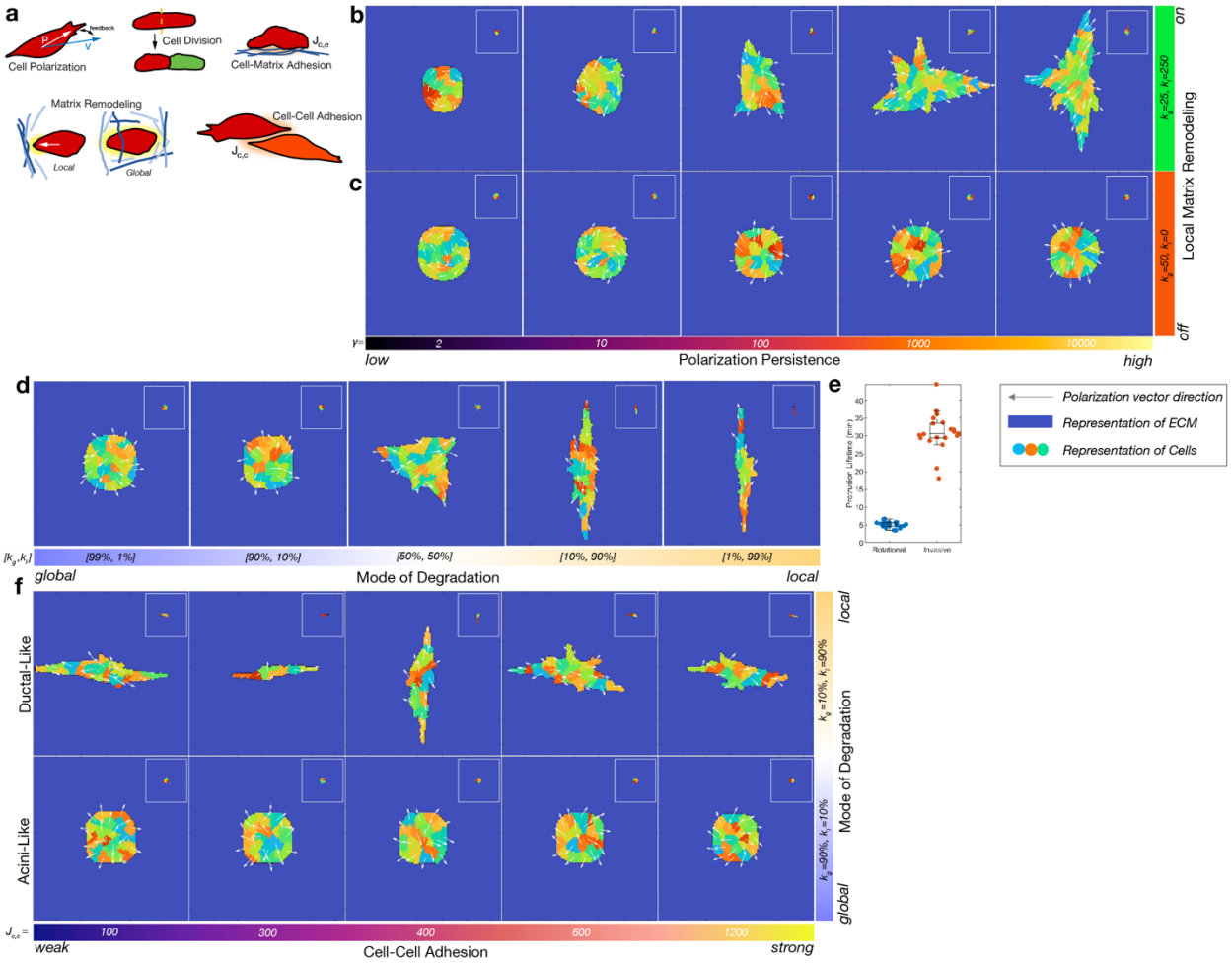


Figure 2.3. A cellular Potts model predicts that RCM and ICM can arise solely from differences in local versus global matrix remodeling. (a) Schematic representation of the additional terms incorporated into the CPM. (b) Simulated 7 day phenotypes of increasing polarization persistence (γ) in the presence of local matrix remodeling (k_l). (c) Simulated 7 day phenotypes of increasing polarization persistence (γ) in the absence of k_l. (d) Simulated 7 day phenotypes of increasing global (left) or local (right) matrix remodeling at constant γ. Quantification of (e) protrusion lifetime from simulations, given constant k_g/k_l values that give rise to either RCM or ICM behaviors (n = 20 multicellular structures). (f) Simulated 7 day phenotypes of increasing cell-cell adhesion ($J_{c,c}$) , given constant k_g/k_l values that give rise to either RCM or ICM behaviors.

2.2.4 Localization of matrix remodeling and polarization distinguish the initiation of RCM and ICM

To assess the relevance of our model predictions, we next characterized the cell-matrix interactions underlying RCM and ICM by performing 3D time-lapse microscopy using a previously established integrated biophysical imaging platform (Fig 2.4a).(Leineweber & Fraley, 2023; Daniel O. Velez et al., 2019) In this system, MDA-MB-231 cells with stable expression of mCherry-LifeAct were generated to visualize F-actin-rich protrusions and give three readouts of *cell protrusion dynamics*: protrusion lifetime, maximum protrusion length, and protrusion rate. Blue fluorescent traction force beads were embedded in the collagen matrix to enable readout of three *cell contractility* measurements: percent (%) bead movers, the maximum bead displacement, and the instantaneous bead displacement (ie. bead speed). Green fluorescent dye-quenched (DQ)-collagen, an indicator of *matrix remodeling*, was incorporated to provide measurement of overall pericellular remodeling (DQ intensity) and remodeling localization (perimeter remodeling (%). Focusing on the timeframe where collective cell migration is initiated, time-lapse microscopy was conducted roughly 36 hours after seeding in dense collagen, when migrating cells were in early ~2-4 cell clusters and could be distinguished by circularity. Mapping these eight biophysical measurements into 2D space using principal component analysis (PCA) separated and clustered the two phenotypes, indicating that our multiplexed biophysical analysis platform effectively captured underlying differences in cell-ECM interactions between RCM and ICM (Fig. 2.4b). A closer look revealed that invasive cell structures generated DQ-collagen signal that was localized primarily to the base of protrusions, while rotationally migrating cells exhibited a global pattern of DQ signal with significantly higher perimeter remodeling (Fig. 2.4a,c). Interestingly, there was no appreciable difference in the overall pericellular DQ intensity, as measured by the average background-normalized DQ fluorescence intensity within a 5 μm band along the periphery of the cell structures (Fig. 2.4d).

This was consistent with model findings that suggested the localization of remodeling was more important for distinguishing these two phenotypes than the overall amount of remodeling (Fig. 2.3b-e). Comparison of protrusion dynamics found that invasively migrating cells had both longer and longer-lived protrusions than rotationally migrating cells, which were instead characterized by short, shorter-lived protrusions (Fig. 2.4e-f, Supplemental Video 2.7-2.8). These matched quantifications of protrusion length and lifetime from simulated ICM and RCM cells with high or low localization of matrix remodeling, respectively (Fig. 2.3d-e). No significant difference was observed in the overall protrusion number (Fig. 2.4g). Tracking of displaced beads also indicated no appreciable differences in cell contractility between these two migration phenotypes, as shown by non-significant differences in all three traction measurements (Fig. 2.4h-j). A Pearson's correlation analyses of the biophysical metrics revealed several interactions, most notably between protrusion dynamics and ECM remodeling (Fig. 2.4k). We found a strong negative correlation between maximum protrusion length and % perimeter remodeling ($r = -0.67$) as well as protrusion lifetime and % perimeter remodeling ($r = -0.77$) (Fig. 2.4l). Linear regression analysis of % perimeter remodeling and protrusion lifetime also demonstrated a moderate level of association between these variables ($r^2 = 59\%$), with invasive and rotational migrating phenotypes separating into two distinct regimes. Overall, this experimental evidence agrees with model predictions that implicate matrix remodeling localization, protrusion length, and protrusion lifetime as key factors that determine ICM and RCM behaviors. The invasive phenotype is initiated by elongated cells with longer-lived protrusions and localized matrix

remodeling that enables cell spreading, while the rotational phenotype is initiated by rounded cells with shorter-lived protrusions and global matrix remodeling.

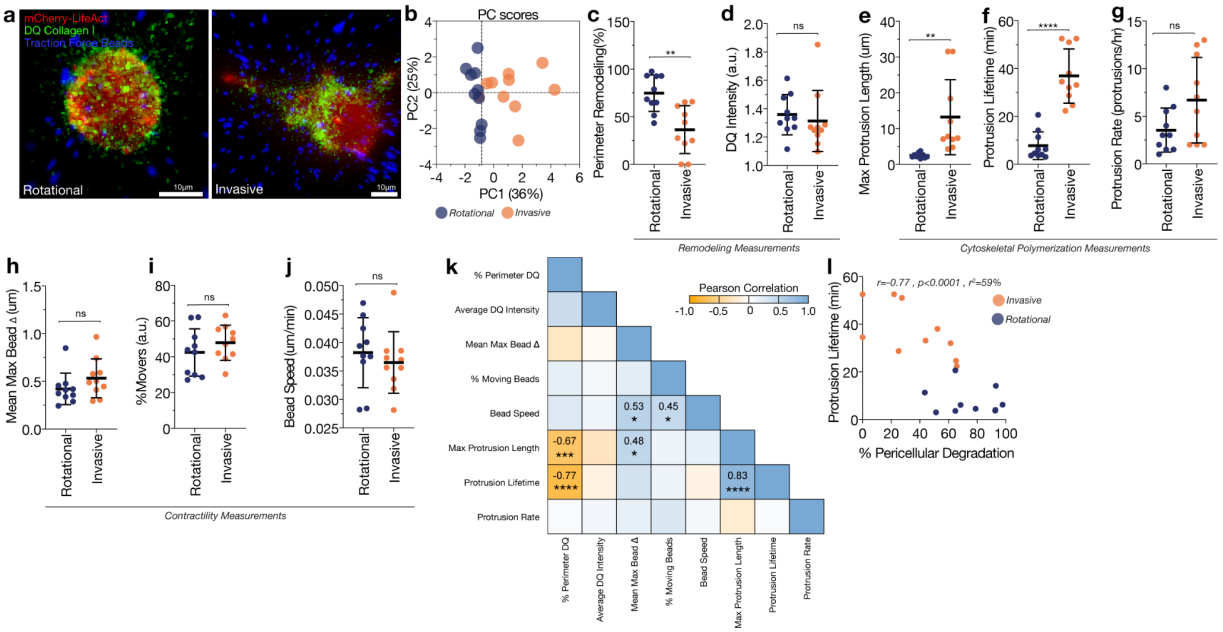


Figure 2.4. Localization of matrix remodeling and polarization distinguish the initiation of RCM and ICM. (a) Micrographs of MDA-MB-231 cells with stable expression of mCherry-LifeAct, blue fluorescent traction force beads, and green fluorescence of DQ-Collagen I incorporated in the surrounding collagen matrix. Scale bar, 10μm. (b) PC1 from PCA of biophysical metrics is sufficient to distinguish between rotational and invasive subpopulations. Quantification of (c) % pericellular matrix remodeling and (d) overall pericellular matrix remodeling intensity, as measured by DQ-Collagen I. Quantification of (e) maximum protrusion length, (f) average protrusion lifetime and (g) protrusion formation rate, as measured by mCherry-LifeAct. Quantification of (h) average maximum bead displacement, (i) average % moving beads, and (j) bead speed, as measured by traction force beads. (k) Several interactions between biophysical modules were found in Pearson's correlation analyses (numbers indicate the Pearson's correlation coefficient of statistically significant interactions). (l) Strong negative correlation found between protrusion lifetime and % perimeter remodeling. For all plots, n = 10 rotationally migrating cell clusters and n = 10 invasively migrating cell clusters. Statistical significance was determined by unpaired two-sided t-test (c-j) and Pearson correlation analysis (k-l) and is indicated as *, **, *** , **** for $p \leq 0.05$, $p \leq 0.01$, $p \leq 0.001$, $p \leq 0.0001$, respectively. All error bars represent standard deviation from the mean.

2.2.5 ICM but not RCM is dependent on proteolytic matrix remodeling

Having established that the formation of acinar-like and ductal-like morphologies originate from distinct patterns of matrix remodeling, we next explored the underlying mechanistic differences regulating these modes. Matrix remodeling is known to occur through both proteolytic and physical mechanisms, and prior work has suggested that DQ-Collagen I may be a readout of both.(Fernández et al., 2021; Gaggioli et al., 2007; Packard et al., 2009; Wolf et

al., 2007) To block proteolytic remodeling, we seeded cells with the broad-spectrum MMP inhibitor (MMPi), Marimastat, and treated daily over the course of a week. MMPi treatment enriched for the formation of the acinar-like phenotype in both MDA-MB-231 and SK-HEP-1 cells (Fig 2.5a, b). Migration tracking at the 2-cell stage revealed that MMPi-treated cells maintained a rounded shape and migrated rotationally with no appreciable differences in angular speed and persistence to the control rotational cells (Fig. 2.5c-g, Supplemental Video 2.9). As a functional readout of MMP inhibition, we compared the DQ-intensity and perimeter localization patterns between control invasive, control rotational, and MMPi rotational cells. Interestingly, MMPi-treated cells generated pericellular DQ signals of similar intensity to both invasive and rotational control cells (Fig. 2.5h,i) with a global remodeling pattern resembling that of control rotational cells (Fig. 2.4b,c). Further investigation using an antibody specific to MMP-cleaved Collagen I showed that control invasive cells exhibited higher MMP-dependent remodeling than control rotational cells, and as expected, MMPi-treated rotational cells exhibited virtually no MMP-dependent remodeling (Fig. 2.5j,k). This data indicates that ICM, but not RCM, is dependent on local proteolytic matrix remodeling. Characterization of protrusion dynamics showed that MMPi-treated rotational cells had significantly lower protrusion length, lifetime and rate compared to invasive cells, suggesting that proteolytic-based matrix remodeling may enable increased protrusion length, lifetime, and polarization (Fig. 2.5l-n). However, MMPs have recently been shown to mediate cleavage of numerous intracellular protein targets involved in cytoskeletal regulation, including α-actinin, talin, and pericentrin (Golubkov et al., 2005; Jobin et al., 2017; Soslau et al., 2014; Sung et al., 2007). As such, treatment of cells with MMPi could have direct effects on the cytoskeleton. To investigate whether the reduced protrusion dynamics and global matrix remodeling pattern observed in MMPi-treated cells could be driven by direct

effects on cytoskeletal protein abundance, we conducted western blot analysis of the known intracellular protein targets of MMPs. No significant changes in abundance were observed in MMPi-treated cells relative to the vehicle control condition (Supplementary Figure 2.1). Altogether, these data demonstrate that ICM, but not RCM, is dependent on local proteolytic matrix remodeling and that proteolytic remodeling may function upstream of actin cytoskeleton activities to regulate cell shape.

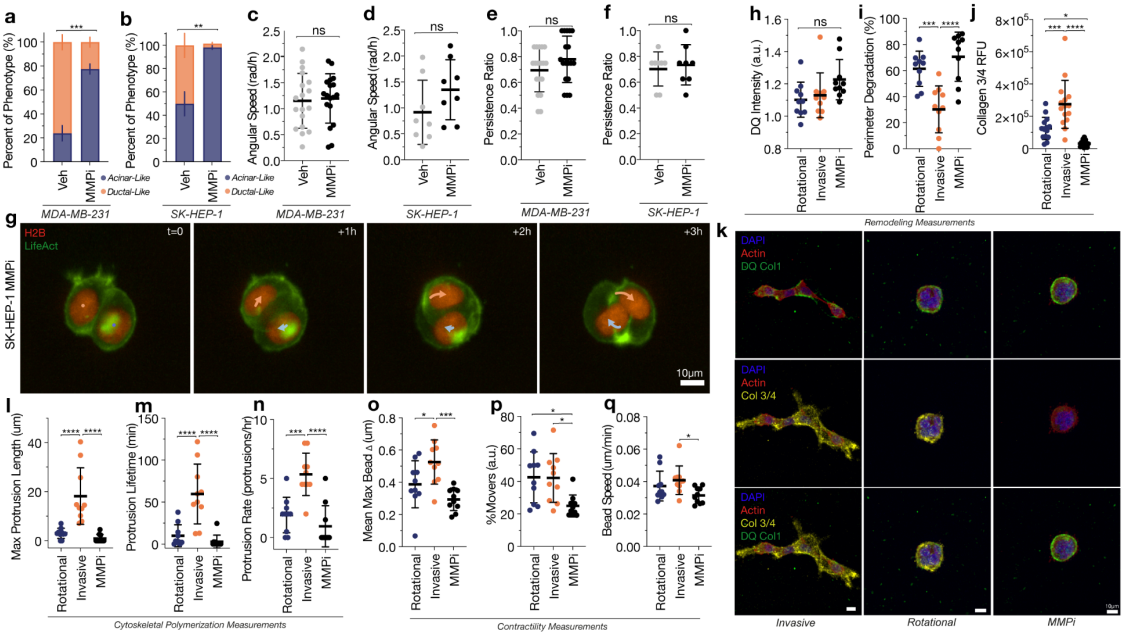


Figure 2.5. ICM but not RCM is dependent on proteolytic matrix remodeling. Frequencies of ductal-like and acinar-like morphologies at 7 days in vehicle- and MMPi-treated (a) MDA-MB-231 (n = 217 multicellular structures and n = 192 multicellular structures for vehicle and MMP-treated conditions, respectively) and (b) SK-HEP-1 cell lines (n = 207 multicellular structures and n = 220 multicellular structures for vehicle and MMP-treated conditions, respectively). Angular speeds of vehicle- and MMPi-treated (c) MDA-MB-231 (n =18 individual cells, n = 9 cell clusters per treatment condition) and (d) SK-HEP-1 cells in 2- cell clusters (n = 8 individual cells, n = 4 cell clusters per treatment condition) . Cell persistence ratio for vehicle- and MMPi-treated (e) MDA-MB-231 (n=18 individual cells, n = 9 cell clusters per treatment condition) and (f) SK-HEP-1 cells in 2- cell clusters (n=8 individual cells, n = 4 cell clusters per treatment condition). (g) Kymograph of circular 2- cell clusters of SK-HEP-1 MMPi-treated cells reveals persistent rotational migration. Scale bar, 10μm. Quantification of (h) overall pericellular matrix remodeling intensity and (i) % pericellular matrix remodeling, as measured by DQ-Collagen I. (j) Quantification of MMP-dependent remodeling, using the Collagen ¾ antibody specific to MMP-cleaved Collagen I (n = 15 cells per condition were analyzed from three independent biological replicates). (k) Representative fluorescent micrographs show matrix remodeling of vehicle-treated invasive and rotational and MMPi-treated rotational MDA-MB-231 cells, as measured by DQ-Collagen I and Collagen ¾ antibody. Scale bar, 10μm. Quantification of (l) maximum protrusion length, (m) average protrusion lifetime, and (n) protrusion formation rate, as measured by mCherry-LifeAct. Quantification of (o) average maximum bead displacement, (p) average % moving beads, and (q) bead speed, as measured by traction force beads. For graphs (h,i, l-q) n =10 cells were analyzed per condition. Statistical significance was determined by unpaired two-sided t-test (a-f) and ordinary one-way ANOVA with Tukey post-hoc tests for multiple comparisons (h-j, l-q) and is indicated as *, **, *** , **** for $p \leq 0.05$, $p \leq 0.01$, $p \leq 0.001$, $p \leq 0.0001$, respectively. All error bars represent standard deviation from the mean.

2.2.6 RCM relies on ITGB1-mediated physical remodeling

Given that MMPi treated cells underwent RCM and maintained the ability to significantly remodel the matrix in an isotropic manner, we hypothesized that RCM may rely on physical mechanisms of remodeling. Tracking of bead displacements during RCM showed that control and MMPi cells maintained comparable, albeit slightly lower traction compared to control ICM cells. This suggested that RCM cells were physically contracting on the matrix (Fig. 2.5o-q, Supplemental Video 2.10) and led us to hypothesize that global remodeling during RCM may be mediated by adhesion-based traction forces on the matrix. Integrin-β1 (ITGβ1) is the canonical cell adhesion receptor for collagen I. To assess the relevance of ITGβ1-dependent adhesion to physical remodeling by rotational cells, we performed ITGβ1 deletion using CRISPR–Cas9 in the MDA-MB-231 cell line (crITGB1, Fig. 2.6a). Similar to previous ITGB1-blocking studies, we found that crITGB1 promoted a rounded phenotype and enrichment of acinar-like structures 7 days after seeding (Fig. 2.6b)(Levental *et al.*, 2009). Analysis of pericellular DQ intensity showed that crITGB1 cells and crITGB1 cells treated with MMPi had similar levels of diminished matrix remodeling (Fig. 2.6c,d). ITGB1 is an important effector for MMP trafficking to the membrane(Grafinger *et al.*, 2020), so we assessed whether crITGB1 may have indirectly caused the reduced matrix remodeling signal. Analysis of matrix remodeling with the Col¾ antibody showed that crITGB1 cells generated similar levels of MMP-cleaved collagen to WT rotational cells, and this diminished only when co-treated with MMPi (Fig. 2.6e). Altogether, this suggested that rotationally migrating cells physically remodeled the matrix through ITGβ1-dependent adhesions. To identify whether adhesion-based matrix remodeling is required for coherent rotational migration, we tracked crITGB1 cells every hour for 10 hours at the 2-cell stage. Surprisingly, we found that rotational migration was abrogated. Cells failed to undergo

coherent rotations and exhibited diminished angular speeds (Fig. 2.6f, g, Supplemental Video 2.11). Taken together, these data demonstrate that physical matrix remodeling via ITGβ1-dependent adhesions is essential for RCM within a confining 3D collagen matrix.

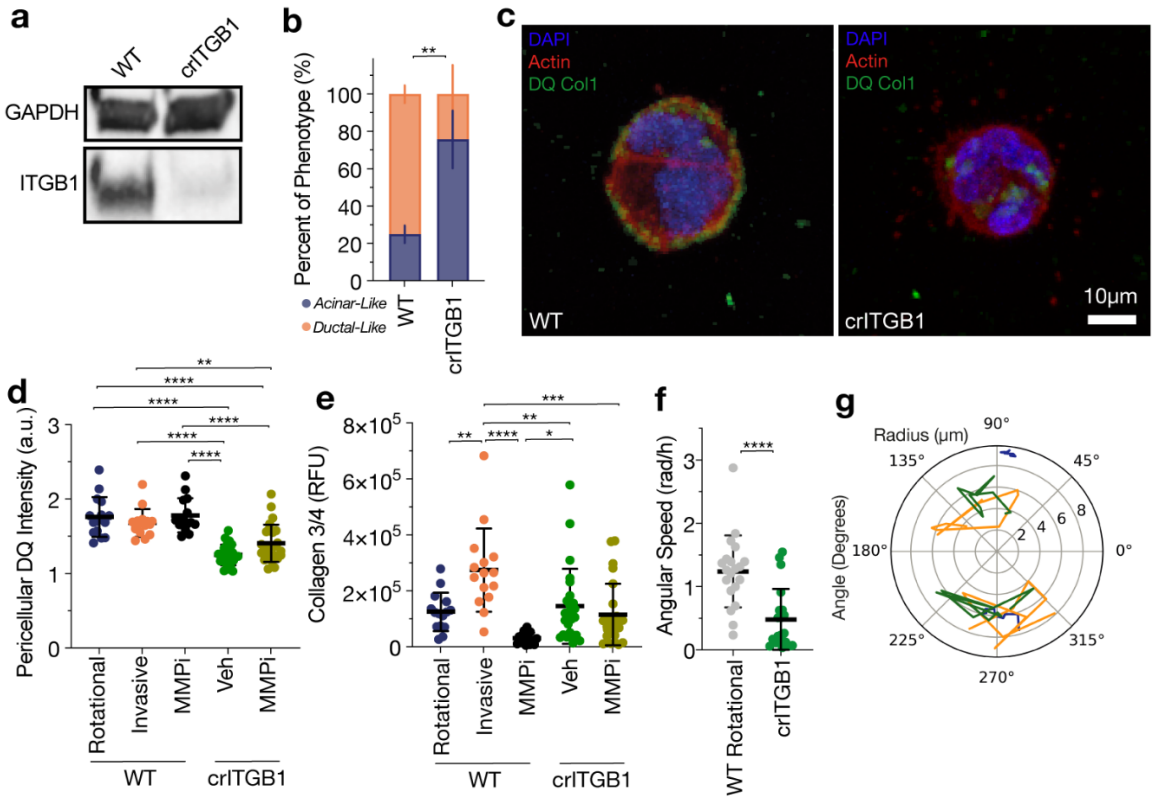


Figure 2.6. RCM relies on ITGB1-mediated physical remodeling. (a) Western blot assessment of *ITGB1* depletion in MDA-MB-231 cell line. (b) Frequencies of ductal-like and acinar-like morphologies at 7 days in WT and crITGB1 MDA-MB-231 cells (n = 139 multicellular structures and n = 141 multicellular structures for WT and crITGB1 cell lines, respectively). (c) Representative fluorescent micrographs show matrix remodeling localization at 48h of rounded WT and crITGB1 MDA-MB-231 cells, as measured by DQ-Collagen I. Scale bar, 10μm. (d) Quantification of overall pericellular matrix remodeling intensity, as measured by DQ-Collagen I (n = 15 cells for all WT conditions, n = 25 for all crITGB1 conditions). (e) Quantification of MMP-dependent remodeling, using the Collagen ¾ antibody specific to MMP-cleaved Collagen I. (n = 15 cells for all WT conditions, n = 25 for all crITGB1 conditions). (f) Angular speed of rotational MDA-MB-231 WT cells and non-rotational MDA-MB-231 crITGB1 cells in 2-cell clusters (n = 20 individual cells, n = 10 cell clusters for each cell line). (g) Polar plots of rounded 2-cell clusters of MDA-MB-231 crITGB1 cells reveals non-rotational migration (n = 6 individual cells, n = 3 cell clusters, Color indicates cluster pair). Statistical significance was determined by unpaired two-sided t-test (b,f) and ordinary one-way ANOVA with Tukey post-hoc tests for multiple comparisons (d-e) and is indicated as *, **, *** , **** for $p \leq 0.05$, $p \leq 0.01$, $p \leq 0.001$, $p \leq 0.0001$, respectively. All error bars represent standard deviation from the mean.

2.3 Methods

2.3.1 Cell culture and cell transfection

MDA-MB-231 breast cancer cells were purchased from ATCC and SK-HEP-1

hepatocellular carcinoma cells were provided by Jason Sicklick. All MDA-MB-231 and SK-HEP-1 cell lines were cultured in high glucose Dubecco's modified Eagle's medium (DMEM, Gibco), supplemented with 10% fetal bovine serum (FBS, Corning) and 0.1% gentamicin (Thermo Fisher Scientific). MCF-10A breast epithelial cells (ATCC) were maintained in DMEM/F12 medium (Invitrogen) supplemented with 5% horse serum (Invitrogen), 20 ng/mL epidermal growth factor (Peprotech), 0.5 µg/mL hydrocortisone (Sigma-Aldrich), 100 ng/mL cholera toxin (Sigma-Aldrich), 10 µg/mL insulin (Sigma-Aldrich), and 0.1% gentamicin (Thermo Fisher Scientific). All cell lines were maintained at 37°C and 5% CO_2 in a humidified environment.

To generate cells that express H2B-mCherry (pHIV-H2BmRFP, Addgene #18982), LifeAct-GFP (Dendra2-Lifeact-7, Addgene #54694) and mCherry-LifeAct (mCherry-LifeAct-7, Addgene #54491), we generated viral particles by transfecting plasmids into lentiX 293T cells (Clonetech) along with the psPAX2 packaging vector (Addgene #12260) and the pMD2.G envelope vector (Addgene #12259). Viral particles were collected by removing culture medium 24 and 48 hours after transfection and filtering through a 0.45 µm filter. Transduced cells were treated with 10 µg/mL Polybrene reagent (Sigma-Aldrich) and a titration of viral particles for 24 hours. Fluorescent cells with the appropriate expression levels of H2B-mCherry, LifeAct-GFP and mCherry-LifeAct were expanded for FACS sorting. For positive selection via FACS, cells were centrifuged at 1400 rpm for 4 minutes before resuspending in FACS buffer (1% BSA, 0.5 mM EDTA in PBS). Samples were sorted at the stem cell core of Sanford Consortium of Regenerative Medicine (La Jolla, CA) on a BD Influx cell sorter (BD Biosciences). Fluorescent samples were compared to unstained WT controls of each respective cell line.

2.3.2 Treatment with pharmacological inhibitors

Matrix metalloproteinases were inhibited using broad-spectrum MMP inhibitor Marimastat

(Abcam) at a concentration of 1μM. As a vehicle control, cells were treated with 0.01% dimethyl sulfoxide (Sigma-Aldrich). Pharmacological inhibitor containing medium was refreshed daily.

2.3.3 CRISPR-Cas9 mediated gene suppression of ITGB1

Genetic knockdown of ITGB1 was performed as described previously(D. O. Velez et al., 2017). In brief, small guide RNAs targeting the ITGB1 gene were cloned into lentiCRISPR v2 plasmid (Addgene #52961) following instructions from Feng Zhang, the plasmid supplier. The sg_RNA sequences were obtained from the GECKO human library A, and were as followed: ITGB1 sg_RNA1 (5′-TGCTGTGTGTTTGCTCAAAC-3′), ITGB1 sg_RNA2 (5′-ATCTCCAGCAAAGTGAAACC-3′). For this study, we used the sg_RNA1. The lentiCRISPR v2 vectors containing the cloned sgRNA were verified by sequencing and were used to generate viral particles via transfection into lentiX293 T cells (Clonetech) along with packaging expressing plasmid (psPAX2, Addgene #12260) and envelope expressing plasmid (pMD2.G, Addgene #12259). After 48h of transfection, viral particles were collected and purified by filtering with a 0.45 μm filter. MDA-MB-231 cells were transduced with viral particles and polybrene (Allele Biotechnology). Following overnight incubation, media was changed and cells were left in normal growth media (DMEM supplemented with 10% FBS and 0.1% gentamicin) for 24-48h. Subsequently, media was changed to selection media containing 2.5 μg/mL puromycin for at least 7d.

To select for knockout cells, MDA-MB-231 ITGB1 sg_RNA1 cells were expanded in a tissue culture to ~80% confluency and harvested. Cells were centrifuged at 350xg and 4°C for 5 minutes before resuspending in 2% HI-FBS in PBS. Cells were incubated for 20 minutes at 4°C with the following antibody: PE anti-human CD-29 (1/40, 303004, Biolegend, San Diego, CA), followed by 2x 2% HI-FBS/PBS washes. Samples were sorted at the stem cell core of Sanford

Consortium of Regenerative Medicine (La Jolla, CA) on a BD Influx cell sorter (BD Biosciences, Franklin Lakes, NJ) and gated using unstained negative and stained MDA WT positive controls.

2.3.4 3D culture in high density collagen I matrices

Cells suspended in culture medium were embedded in 3D collagen I matrices by mixing with 10x reconstitution buffer (1:1 v/v) and high concentration, rat tail acid extracted type I collagen (Corning) to a final collagen I concentration of 6 mg/mL and final seeding density of 100,000 cells/mL. The pH was adjusted using 1 N sodium hydroxide, and the mixture was added to 48-well culture plates at a final volume of 200 µL. The mixture was polymerized by incubating at 37°C for 30 min, and an equal volume of culture media was added to the top of the gels. For labeling of remodeled collagen, dye-quenched (DQ) collagen type I (Thermo Fisher Scientific) was mixed into collagen hydrogels at a final working concentration of 100 µg/mL, prior to pH neutralization and gel polymerization. For WT 7 day phenotype studies, media was replenished every other day. For 7 day phenotype studies using pharmacological inhibitors, media was replenished every day.

2.3.5 7 day phenotype structure imaging and quantification

Following 7 days in 3D culture, cell structures were imaged at 10x magnification using a Nikon Ti-Eclipse Epifluorescent Inverted Microscope. For each biological replicate (n=3), three fields of view (FOV) were selected and z-stacks from the bottom to the top of the collagen gel (50 µm step-size) were taken under brightfield illumination. Images were exported as .tif files and opened in ImageJ (NIH) for analysis. Structures that were at least 100 µm away from the top and bottom of the gel were selected, manually traced using the “Freehand selections” tool, and their circularity was determined using the “Shape descriptors” measurement output. For each FOV, a

minimum of 25 structures were traced. A circularity threshold of <0.6 and >0.8 was set to define ductal-like phenotypes and acini-like phenotypes, respectively.

For long-term phenotype tracking, collagen gels were prepared in triplicate as described above. After 2 days in culture, cell structures were imaged at 10x magnification using a Nikon Ti-Eclipse Epifluorescent Inverted Microscope. Five fields of view (FOV) at least 100 μm away from the top and bottom were selected across the three biological replicates. The same FOVs were imaged daily until 7 days after seeding. Structures were manually traced and their circularity was determined in ImageJ (NIH), as described above.

2.3.6.1 Immunofluorescence staining

Cells embedded in 3D collagen I matrices were washed twice with 1x phosphate buffered saline (PBS, Gibco) briefly and fixed with 4% paraformaldehyde (Electron Microscopy Services) diluted in 1x PBS for 30 min at room temperature. Prior to fixation, the collagen gels were washed three times with 1x PBS for 5 min each, followed by three, 5 min rinses with 100mM glycine solution prepared in 1x PBS. Subsequently, the collagen gels were scooped, transferred to 24-well culture plates and blocked overnight at 4°C with a 1x PBS solution containing 1% w/v bovine serum albumin (BSA, Sigma-Aldrich), 2.5% v/v goat serum, 2.5% v/v FBS (Corning), and varying concentrations of Triton-X-100 (0.02-0.2% v/v, Thermo Fisher Scientific). After blocking, gels were three times with 1x PBS for 5 min. Primary antibody was diluted in antibody dilution buffer, which is composed of 1x PBS with 1% w/v BSA (Sigma Aldrich), 2.5% v/v goat serum, 2.5% v/v FBS (Corning), and 0.02% v/v Triton-X-100 (Thermo Fisher Scientific). Collagen hydrogels were covered with diluted primary antibodies and incubated for 2 days at 4°C. Following primary antibody incubation, gels were washed three times with 1x PBS, 15 min each. Subsequently, hydrogels were incubated with diluted secondary antibodies for 1 day at 4°C. After secondary

antibody labeling, the gels were washed three times with 1x PBS, 15 min each. For F-actin visualization, gels were incubated in phalloidin diluted in 1x PBS for 1-2 h at room temperature, protected from light with aluminum foil. Samples were washed with 1x PBS three times for 15 min each. To stain cell nuclei, DAPI (Thermo Fisher Scientific) was added for 10 min. All steps were done with constant agitation on an orbital shaker. Primary and secondary antibodies used for immunofluorescence staining are listed below.

2.3.6.2 Primary antibodies

Mouse monoclonal anti-E-cadherin (clone SHE78-7) – 13-5700, dilution 1:250, Invitrogen

Mouse monoclonal anti-Laminin-5, γ2 chain (clone D4B5) – MAB19562, dilution 1:100, Sigma-Aldrich

Rabbit monoclonal anti-pan-cadherin (clone EPR1792Y) – ab51034, dilution 1:200 , Abcam

Rabbit polyclonal anti-collagen type 1 (3/4 fragment) – AG-25T-0116-C025, dilution 1:100, Adipogen

Mouse monoclonal anti-integrin beta 1 (clone P5D2) - ab24693, dilution 1:250, Abcam

Mouse monoclonal anti-human MMP-14 (clone 128527) - MAB9181100, dilution 1:100 , R&D Systems

2.3.6.3 Secondary antibodies

Alexa Fluor 488 conjugated goat anti-rabbit IgG Fab2 – 4412S, dilution 1:1000, Cell Signaling Technologies

Alexa Fluor 546 conjugated goat anti-mouse IgG – A11003, dilution 1:1000, Invitrogen

Alexa Fluor 546 conjugated goat anti-rabbit IgG – A11035, dilution 1:1000, Invitrogen

Alexa Fluor 594 conjugated goat anti-mouse IgG Fab2 – 8890S, dilution 1:1000, Cell Signaling Technologies

Alexa Fluor 647 conjugated goat anti-rabbit IgG – A21245, dilution 1:1000, Invitrogen

For F-actin labeling:

- Alexa Fluor Plus 405 Phalloidin – A30104, dilution 1:200, Invitrogen
- Alexa Fluor 488 Phalloidin – 8878S, dilution 1:20, Cell Signaling Technologies
- Alexa Fluor Plus 647 Phalloidin – A30107, dilution 1:200, Invitrogen
- Alexa Fluor 647 Phalloidin – A22287, dilution 1:200, Invitrogen

For nuclei staining, DAPI – 62248, dilution 1:1000, Thermo Fisher Scientific

2.3.7 Biophysical gel culture, imaging, and quantitative analysis of cell-ECM interactions

2.3.7.1 Biophysical gel 3D culture

MDA-MB-231 mCherry-LifeAct cells were suspended in culture medium (WT - complete DMEM, Vehicle - 0.01% DMSO in complete DMEM, MMPi - 1 μM Marimastat in complete DMEM) and were mixed 1:1 v/v with 1x reconstitution buffer to achieve a final concentration of 100,000 cells/mL. Next, 1 μm diameter, blue carboxylated microspheres (Thermo Fisher Scientific) were added to the cell-buffer mixture at a final concentration 1:50 (v/v) of the final gel volume (200 μL). Dye-quenched (DQ) collagen type I (Thermo Fisher Scientific) was added to the cell-buffer solution at a final working concentration of 100 μg/mL. Lastly, the cell-buffer solution was mixed into high concentration, rat tail acid extracted type I collagen (Corning) to reach the desired final collagen concentration of 6 mg/mL. Subsequently, the pH was adjusted to 7.0 using 1 N sodium hydroxide and the cell-gel solution was added to custom made PDMS wells mounted on 35mm, glass bottom dishes (FluoroDish, World Precision Instruments) following thorough mixing. Collagen gels were polymerized at 37°C in a humidified incubator for at least 30 min prior to covering the gel with culture medium.

2.3.7.2 Biophysical imaging

After 33-39 hours in culture, cells were transferred to a Tokai Hit stage-top incubator on a Nikon Ti-Eclipse Epifluorescent Inverted Microscope. Multichannel z-stacks with an axial displacement of 37 μm (1 μm step size) were acquired every 2 minutes for 2 hours using an oil-immersion 40x objective (NA 1.5). For each time interval, z-stacks through the cell body were taken in three channels (blue, green, and red), to visualize the fluorescent beads, DQ collagen, and mCherry-LifeAct, respectively. Invasive and rotational cells at the ~2-4-cell stage whose primary axis of spreading was along the XY plane were selected for quantitation.

2.3.7.3 Biophysical imaging analysis

Maximum intensity projections (MIPs) of the z-stacks were generated for each time point to generate 2D time series for each channel of the cell selected for analysis. Biophysical Imaging Analysis Multichannel z-stacks and MIPs were saved as .tif files and opened in ImageJ (NIH) for processing and analysis.

2.3.7.4 Quantification of protrusion dynamics

For cell protrusion dynamics analysis, protrusions were manually tracked in ImageJ using MIP time series of the mCherry-LifeAct expressing cells. In order to determine the time duration or protrusion lifetime, each protrusion was tracked frame-by-frame from initial protrusion extension to complete protrusion retraction. Protrusions longer than 2 μm were included in analysis and a protrusion was considered fully retracted when their length was below this threshold. The mean maximum protrusion length and time duration of the protrusion (ie. “protrusion lifetime”) was calculated for each cell. The number of protrusions greater than 2 μm observed over the course of the 2 hr imaging period was used to determine the “protrusion rate”. For cells that did not form any protrusions greater than 2 μm in length during imaging, the mean maximum protrusion length and protrusion lifetime were both zero.

2.3.7.5 Quantification of matrix remodeling

In order to quantify the degree of collagen degradation, the fluorescence intensity of a 5 μm band surrounding the cell, as defined by the mCherry-LifeAct channel, was measured at each time frame for each slice of the z-stack. The total fluorescence intensity (integrated density) values were summed and divided by the total area of the band in order to get mean fluorescence intensity. This value was divided by the mean fluorescence intensity of the background to get the signal/ background ratio, referred to as DQ Intensity. To determine the localization of matrix remodeling, binary masks of MIPs of the DQ channel at the first time point (t = 1/61) were generated by applying a binary threshold to distinguish signal from background. Next, 1 μm bands along the cell perimeter were generated from MIPs of the cell channel. Lastly, the percent of the band area covered by DQ signal was determined using the Area Fraction measurement in ImageJ. This measurement is referred to as the "Perimeter Remodeling (%)".

For quantifying matrix remodeling on confocal images, the phalloidin channel was used to define the cell ROI for each slice of the z-stack. For the confocal dataset, a 3 μm band was used due to reduced scattering of out-of-plane light. Quantification of DQ intensity was conducted as described above.

2.3.7.6 Quantification of cell contractility using traction force beads

Bead tracking was done using MIPs of the blue channel using the Mosaic plugin in ImageJ, as previously described(Leineweber & Fraley, 2023; Daniel O. Velez et al., 2019). The resulting table containing XY coordinates for each bead in the 165μm x 165μm field of view for each timepoint was saved and analyzed using a custom MATLAB script that identifies beads that moved during time-lapse imaging. First, a filter was applied to only analyze the trajectories of beads that were tracked at all time points. After filtering, the displacement at each time point from the initial

point was determined for each bead. In order to distinguish beads that were actively being pulled from those moving due to Brownian motion, a moving standard deviation approach was employed. The trajectories of beads not removed by filtering were measured resulting in the "mean instantaneous bead speed" and "mean maximum displacement". The "% movers" metric corresponds to the percent of total beads in the field of view that satisfy this criteria.

2.3.8 Image acquisition and analyses for migrational tracking

MDA-MB-231 H2B-LifeAct, SK-HEP-1 H2B-LifeAct and MDA-MB-231 crITGB1 H2B-LifeAct cells were embedded in a 200µL 6mg/mL Collagen I gel with 100,000 cells in a glass bottom 48-well plate, polymerized for 30 min at 37°C, and 200µL of culture medium was added on top. Following 24 hours of culture, the plate was transferred to a microscope stage top incubator on a Nikon Ti-E inverted microscope and z-stacks with an axial displacement of 35 µm (1.5 µm stepsize) were acquired at 40x magnification every 1 hour for 18-24 hours. Invasive and rotational cells at the two-cell stage were selected for speed quantification and all dividing cells were excluded, as determined by the H2B-mCherry channel. Given the presence of dividing cells, we quantified 10 hours of consecutive frames for speed and cell persistence calculations. Migrational tracking was conducted within the Bitplane Imaris software. First, background subtraction was performed on both the LifeAct-GFP and H2B-mCherry channels by setting threshold values to 5 and 10, respectively, using the built-in image processing plugin. Nuclei tracking was conducted using the Imaris object tracking plugin. Center of mass for calculating angular velocities was determined by generating a reference frame using the surface rendering of the LifeAct-GFP channel. The positions of all tracked cells over time were then exported as Excel sheets and analyzed for speed and cell persistence ratios. Invasive speeds were automatically calculated by the Imaris software. Angular speeds for rotational cells were calculated from the XY coordinates

of nuclei relative to the LifeAct center of mass.

Cell persistence ratio, modified from the previously described metric to describe both rectilinear and angular migration, can be represented as the following equation(S. Jain et al., 2020):

$$\Sigma_0^{n=frame} \frac{1\ if\ vector\ in\ same\ direction\ as\ previous\ frame, 0\ if\ direction\ changes}{n}$$

We redefine the metric here to quantify the likelihood that a cell's angular or rectilinear velocity vector remained We redefine the metric here to quantify the likelihood that a cell's angular or rectilinear velocity vector remained in the same direction between consecutive imaging frames over the course of the 10 hours that rectilinear or angular speeds were calculated. Briefly, for rotational migration, we quantified the proportion of time that cells migrated consistently in a clockwise (CW) or counterclockwise (CCW) radial direction such that a value of 0 indicated directionless, oscillatory motion and a value of 1 indicates CW/CCW motion without a change in direction. A similar rectilinear persistence ratio for invasive cells is quantified as the proportion of time cells migrated consistently without changing direction (<90º from previous direction), using the formula for calculating the angle between two rectilinear vectors: $cos(\theta) = \frac{v_i \cdot v_f}{|v_i||v_f|}$ where v_i and v_f represent the initial and final velocity vectors.

2.3.9 Confocal microscopy

Immunostained confocal images were acquired using a Leica SP8 inverted confocal microscope. The microscope was equipped with a 40x water immersion objective. Samples were excited at the appropriate excitation wavelength for the fluorophore(s) of interest.

2.3.10 Cellular Potts model simulations

The CPM relies on minimization of an energy term, the Hamiltonian (H), to model cell dynamics on a connected square lattice. Our Hamiltonian consists of four terms: contact energy, a cell size constraint, actin polarization, ECM confinement:

$$H = H_{contact} + H_{size} + H_{polarization} + H_{ECM\ confinement}$$

$$H_{contact} = \sum_{i,j\ neighbors} J_{\tau(\sigma_i),\tau(\sigma_j)}(1 - \delta_{\sigma_i,\sigma_j})$$

$$H_{size} = \lambda_a(a(\sigma_{cell}) - A)^2$$

$$H_{polarization} = -\lambda_p P \cdot \sum_{i,j\epsilon\sigma_{cell}} r_{i,j}$$

$$H_{ECM\ confinement} = \lambda_{ECM} P \cdot \sum_{i,j\epsilon\sigma_{cell}} S_{i,j}$$

The coupling strength (*J*) of the contact energy term is dependent on the types (τ(σ)) of interacting lattice sites, where *Jc*,*c* models cell-cell adhesion strength, Jc,e represents cell-ECM adhesion strength and Jc,m corresponds to cell-medium interfacial tension. The cell size constraint accounts for the energy cost for a cell to deviate from its optimal size, where *A* is the target cell area and *a*(σ*i*) is the area of the cell with label *i.* The cell polarization vector (P) models polarization of the actin cytoskeleton, and is governed by:

$$\frac{dP_x}{dt} = k_+ \frac{v_x}{|v|}(1 - |P|) - k_P_x$$

$$\frac{dP_y}{dt} = k_+ \frac{v_y}{|v|}(1 - |P|) - k_P_y$$

These equations simulate the positive feedback between cell motion (v) and actin polarization dynamics, where a cell's orientation and propulsion intensity is dependent on rate of production (k+) and the rate of degradation (k-) of the polarization vector (P). We can also define the polarization persistence, γ=*k*+/*k*- , as the ratio between the two rates to determine how quickly the direction of the polarization vector is updated. To capture ECM remodeling, we incorporated

the fact that remodeling can occur through both proteolytic cleavage and physical disruption (Fernández et al., 2021; Gaggioli et al., 2007; Hall et al., 2016; Wyckoff et al., 2006). Consistently, we incorporated a matrix-remodeling agent (E) that can be produced either locally or globally, given by:

$$\frac{dE}{dt} = D\nabla^2 E + k_g \delta_{\sigma_{i,j},\sigma_{cell}} + k_l \delta_{\sigma_{i,j},\sigma_{cell,tip}} - k_d E - k_r ES$$

$$\frac{dS}{dt} = -k_r ES$$

$$\sigma_{cell,tip} = \sigma_{cell} \cap [\, P_{i,j} \geq \ 0.99 \times max(\sum_{\forall i,j} \quad r_{i,j} \cdot P)]$$

where D is the diffusion coefficient, δ is the kronecker delta, kg and kl are the respective rates of global and local agent production, kd is the auto-degradation rate of the agent and kr is the reaction rate of the agent with the ECM. For local remodeling, each individual cell only releases the agent locally at the tip of the cell, as determined by the direction of the polarization vector (P) and only when the cell element is in contact with an ECM element. In the mode of global remodeling, the agent release is non-directional and over the whole cell body. We capture physical confinement by the ECM as an ECM penetration penalty where the penetration cost is proportional to the concentration of the ECM (S) and the parameter that indicates the strength of the ECM (λECM). Lastly, we simulated proliferation by modeling cell growth followed by division. Cells grow to a target size A(t) increased by the growth rate G(t) as a function of time. As the number of cells in a 2D cross-section actually corresponds to a larger number of cells in 3D, we incorporated a term, k >1, in our proliferation model to account for the differences between experiment and simulation.

This simulated cell growth be summarized as:

$$\frac{dA(t)}{dt} = G(t) = \frac{G_0}{k^t}$$

We then employed a stochastic approach to model division such that when the cell area exceeds a threshold value (*Athres = pAmax*, with p equals 0.85 in our model), it divides into two smaller cells with a fixed probability at each simulation step.

2.3.11 Collagen ¾ R.F.U. Quantification

MDA-MB-231 WT and MDA-MB-231 crITGB1 cells were embedded in a 200µL 6mg/mL Collagen I gel at a seeding density of 50,000 cells and treated immediately with 0.01% DMSO (Vehicle) or 1uM Marimastat (MMPi) for 48h. Immunostained z-stack confocal images were acquired using a Leica SP8 inverted confocal microscope. Quantification of collagen ¾ R.F.U. was conducted as following in ImageJ. First, z-stack images were projected using the sum intensity method. Second, an ROI around signal region was drawn. Third, the sum of pixel intensity (integrated density) within a structure was measured. Fourth, the average background signal intensity was measured using an ROI of same area to that of the signal region. Fifth, we normalized the pixel intensity within a structure to the background signal intensity and the # of nuclei within a structure (to account for cell count differences within a structure) using the following:

$$¾\ Collagen\ Intensity = \frac{Integrated\ Density\ -\ (Area\ of\ Structure * Average\ Fluorescence\ of\ background)}{\#\ of\ Nuclei}$$

2.3.12.1 Western blot analysis

MDA-MB-231 WT and MDA-MB-231 crITGB1 cells were embedded in a 400µL 6mg/mL rat tail acid extracted type collagen I gel at a seeding density of 500,000 cells/mL.

Following neutralization with 1 N sodium hydroxide, the mixture was cast into a 24-well plate, and polymerized at 37°C for 30 min. Following polymerization, an equal volume of culture media was added to the top of the gel. After 24h and 48h in culture, the 3D collagen I gels were digested using 10 mg/mL collagenase (Sigma-Aldrich) at 37°C for 20 min, and filtered through a 35µm filter. After washing once with 1x PBS, cells were lysed using 200µL RIPA lysis buffer (Thermo Fisher Scientific) supplemented with 1x Halt Protease and Phosphatase Inhibitor Cocktail (Thermo Fisher Scientific). Cell lysates were kept on ice, vortexed every 5 min for a total of 30 min, and stored long-term at -20°C. Protein content was determined using a Pierce Micro BCA Protein Assay Kit (Thermo Fisher Scientific), according to the manufacturer's instructions. Samples were prepared by mixing 12-20µg of protein lysates with 4x Bolt LDS Sample Buffer (Invitrogen) and 10x NuPAGE Sample Reducing Agent (Invitrogen). Samples were then boiled at 95°C for 5 min and resolved on 10-12% SDS-PAGE gels with appropriate running buffer. Following gel electrophoresis, protein was transferred onto a 0.45µm PVDF membrane (Millipore) and blocked with 5% BSA in 1x TBST for 1h at RT. Membranes were then incubated overnight at 4°C with appropriate primary antibodies. Membranes were washed three times with 1x TBST for 5 min, and then incubated with the appropriate HRP-conjugated secondary antibody for 1h at room temperature. After washing with 1x TBST, the signal was developed by incubating the membranes in Clarity ECL Western Blotting Substrate (Biorad). Densitometry quantification was performed using ImageJ software (NIH). Primary and secondary antibodies used for Western blotting are listed below.

2.3.12.2 Primary antibodies

Rabbit polyclonal anti-alpha-actinin – #3134, dilution 1:500, Cell Signaling Technologies

Rabbit polyclonal anti-integrin β1 – #4706, dilution 1:500, Cell Signaling Technologies

Rabbit monoclonal GAPDH (clone 14C10) – #2118, dilution 1:1000, Cell Signaling Technologies

Rabbit polyclonal anti-pericentrin – ABT59, dilution 1:500, Sigma-Aldrich

Mouse monoclonal anti-talin 1 and 2 (clone 8D4) – ab11188, dilution 1:500, Abcam

2.3.12.3 Secondary antibodies

Anti-rabbit IgG, HRP-linked antibody – #7074, dilution 1:1000, Cell Signaling Technologies

Anti-mouse IgG, HRP-linked antibody – #7076, dilution 1:1000, Cell Signaling Technologies

2.3.13 Statistical analysis

Principal component analysis (PCA) and all statistical tests were performed using Graphpad Prism. PCA analysis of the biophysical imaging data was performed by z-normalizing the eight cell-ECM measurements for rotational and invasive cells analyzed in the wild-type dataset using the Graphpad Prism PCA tool. Student t-tests were used to perform the means of two populations. One-way ANOVA analyses were performed followed by Tukey post-hoc tests for multiple comparisons were performed to compare the mean of three or more populations. See figure captions for specific details of statistical analyses and number of replicates analyzed.

2.4 Funding

Support for this study was provided by National Science Foundation CAREER award MCB-1651855 to S.I.F., National Science Foundation grant DMS-1953469 to W-J.R. and S.I.F., and American Cancer Society Research Scholar Grant RSG-21-033-01-CSM to S.I.F.. We would like to thank the UC San Diego School of Medicine Microscopy Core, which is supported by the National Institute of Neurological Disorders and Stroke grant P30NS047101.

2.5 Author contributions

S.R., A.W., W.D.L., M.T., W-J. R. and S.I.F. designed the experiments. S.R. and A.W. performed all wet lab experiments and analysis. S.L. performed 7 day structure analysis. M.T.

performed all computational experiments and analysis. S.R., A.W., W.D.L., M.T., W-J. R. and S.I.F contributed to data interpretation as well as writing and editing of the manuscript.

2.6 Supplementary Material

2.6.1 Supplementary Figures

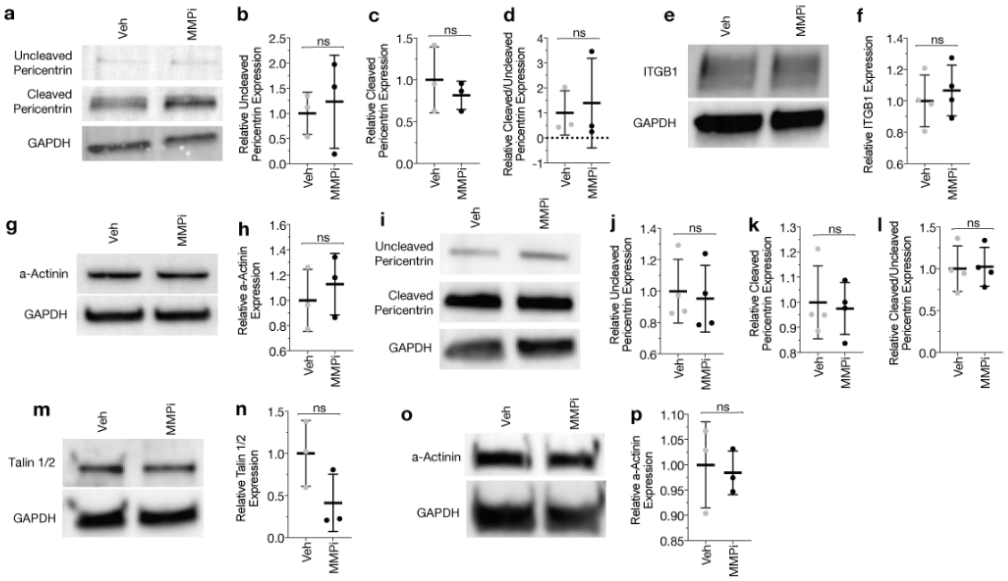


Figure 2.7. Supplementary Figure 2.1 Western blot of cytoskeletal proteins susceptible to MMP-mediated cleavage. (a) Western blot assessment of cleaved and uncleaved Pericentrin in MDA-MB-231 treated with vehicle or MMPi for 24 hours. Quantifications of (b) uncleaved, (c) uncleaved, and (d) relative cleaved/uncleaved Pericentrin in MDA-MB-231 treated with vehicle or MMPi for 24 hours. (e) Western blot assessment of ITGB1 in MDA-MB-231 treated with vehicle or MMPi for 24 hours. (f) Quantification of relative ITGB1 in MDA-MB-231 treated with vehicle or MMPi for 24 hours. (g) Western blot assessment of a-Actinin in MDA-MB-231 treated with vehicle or MMPi for 24 hours. (h) Quantification of relative a-Actinin in MDA-MB-231 treated with vehicle or MMPi for 24 hours. (i) Western blot assessment of cleaved and uncleaved Pericentrin in MDA-MB-231 treated with vehicle or MMPi for 48 hours. Quantifications of (j) uncleaved, (k) uncleaved, and (l) relative cleaved/uncleaved Pericentrin in MDA-MB-231 treated with vehicle or MMPi for 48 hours. (m) Western blot assessment of Talin 1/2 in MDA-MB-231 treated with vehicle or MMPi for 48 hours. (n) Quantification of relative Talin 1/2 in MDA-MB-231 treated with vehicle or MMPi for 48 hours. (o) Western blot assessment of a-Actinin in MDA-MB-231 treated with vehicle or MMPi for 48 hours. (p) Quantification of relative a-Actinin in MDA-MB-231 treated with vehicle or MMPi for 48 hours. Statistical significance was determined by unpaired two-sided t-test and is indicated as *, **, *** , **** for $p \leq 0.05$, $p \leq 0.01$, $p \leq 0.001$, $p \leq 0.0001$, respectively. All error bars represent standard deviation from the mean.

2.6.2 Supplementary Videos

Supplemental Video 2.1. MDA-MB-231 cells undergoing RCM at the 2 cell stage.

Supplemental Video 2.2. MDA-MB-231 cells undergoing RCM at the 3-4 cell stage.

Supplemental Video 2.3. MDA-MB-231 cells undergoing ICM at the 2 cell stage.

Supplemental Video 2.4. MDA-MB_231 cells undergoing ICM at the 3-4 cell stage.

Supplemental Video 2.5. SK-HEP-1 cells undergoing RCM at the 2 cell stage.

Supplemental Video 2.6. SK-HEP-1 cells undergoing ICM at the 2 cell stage.

Supplemental Video 2.7. Rotationally migrating MDA-MB-231 cells have shorter and more short-lived protrusions.

Supplemental Video 2.8. Invasively migrating MDA-MB-231 cells have longer and more long-lived protrusions.

Supplemental Video 2.9. MMPi-treated MDA-MB-231 cells undergoing RCM at the 2-cell stage.

Supplemental Video 2.10. MMPi-treated MDA-MB-231 cells physically contracting their surrounding matrix.

Supplemental Video 2.11. CRISPR-mediated knockdown of ITGB1 prevents coherent RCM.

2.7 Acknowledgements

Chapter 2, in part is currently being prepared for submission for publication of the material. Ranamukhaarachchi, S. K., Walker, A., Tang, M.H., Leineweber, W.D., Lam, S., Rappel, W.J., Fraley, S.I. The dissertation author was the co-primary investigator and co-first author of this paper.

We thank members of the Fraley lab for their technical assistance and insightful comments regarding this work.

CHAPTER 3

Therapeutic differentiation of CSCs in preclinical models of Triple Negative Breast Cancer

3.1 Introduction

Triple Negative Breast Cancer (TNBC) is a subtype of breast cancer that is a highly aggressive, lacks targeted therapy options, and is associated with a higher risk of early metastasis and poorer outcomes than other breast cancer subtypes.(S.-Y. Park et al., 2019) Defined by an absence of estrogen receptor (ER), progesterone receptor (PR) and human epidermal growth factor receptor 2 (HER2) expression, TNBC has the highest mortality of all clinically defined subtypes due to its lack of targeted or hormonal therapies.(Bauer *et al.*, 2007) As such, for most TNBC patients, chemotherapy remains the standard.(Gennari *et al.*, 2021) Nonetheless, this systemic treatment method remains flawed, primarily due to the tumor cell niche known as cancer stem cells (CSCs) that resist chemotherapy and thereby become enriched within tumors following treatment.(Bleau et al., 2009; M. K. Kang et al., 2008; Peitzsch et al., 2013) As such, the development of CSC-targeted therapeutics holds significant promise for improving survival and quality of life in patients with TNBC.

Enrichment of the CSC phenotype and the degree of chemo-resistance found within a tumor is also directly linked to enrichment of the Epithelial-to-Mesenchymal Transition (EMT) programme, a key component of metastatic intravasation(Lambert & Weinberg, 2021). EMT is a conserved process by which epithelial cells disassemble their strong cell-cell junctions, lose polarity and transdifferentiate into invasive mesenchymal cells with a newly upregulated migratory machinery(Dongre & Weinberg, 2019). In recent years, it has become abundantly clear that EMT and the reverse process of Mesenchymal-to-Epithelial Transition (MET) are not binary events, but rather fluid programmes used by cells to interact with their environment. During collective cancer invasion, clusters of cells with distinct individual “hybrid” E/M states

coordinate their movement through cell-cell and cell-ECM interactions in order to lead collective cancer invasion(Grasset *et al.*, 2022). Thus, inhibition of the EMT programme may be one mechanism by which the development of CSC-targeted therapeutic strategies may hold significant promise for improving survival and quality of life in patients with TNBC.

Two strategies have been envisioned to target CSCs(Dingli & Michor, 2006): (1) target features of CSCs to induce cytotoxicity, (2) induce MET in CSCs such that they exit the more mesenchymal tumor-initiating state and enter into an epithelial non-stemlike state, slowing growth and making them more susceptible to conventional therapies. In the first category, the majority of currently available CSC-targeting strategies inhibit developmental signaling pathways that regulate the maintenance and survival of both normal stem cells (SCs) and CSCs, e.g. Notch, Wnt, Hedgehog(Yang *et al.*, 2020).

Taking the second approach and combining differentiation therapy with traditional cytolytic agents has been shown to increase the susceptibility of tumor cells, thereby avoiding enrichment of cells with multi-drug resistance (MDR)(de Thé, 2018). Previous work in pre-clinical models have demonstrated that reverting cells from a “stem-like” mesenchymal phenotype to a more “differentiated” epithelial phenotype can render cells more sensitive to a range of chemotherapeutics, including doxorubicin, paclitaxel, HSP90 inhibitors, methotrexate, and EGFR-MAPK pathway inhibitors(Pattabiraman *et al.*, 2016). While such differentiation therapy has been successfully implemented in acute promyelocytic leukemia (APL) with the combination of retinoic acid (RA) and arsenic, there has been limited success in the clinic for solid tumors(de Thé, 2018). The absence of differentiation therapies for solid tumors may be due to pathological differences versus APL and other leukemias, such as the presence of multiple oncogenic drivers or a more complex tumor microenvironment (TME).(de Thé, 2018)

Alternatively, current screening methods for identifying differentiation therapies may inaccurately model such complexities, resulting in false negatives and an early termination in the discovery process of a potential therapeutic.

In this study, we find that high-density Collagen I (HD Col1) induces TNBC cells into a distinct Notch activation state that regulates collective cell invasion (CCI). By conducting a phenotypic screen using migrational and molecular readouts of differentiation, we identify a novel small molecule with CSC differentiation activity unique to this 3D model system.

3.2 Results

3.2.1 Notch activation regulates collective invasion in TNBC

In prior work, we found that a 3D high density collagen 1 (6 mg/ml) (HD Col1) culture system induces multiple solid tumor cell types to adopt phenotypic and transcriptional states that are representative of aggressive clinical disease(K. Chen et al., 2021; Ranamukhaarachchi et al., 2019; D. O. Velez et al., 2017; Daniel O. Velez et al., 2019; Zheng et al., 2021). This includes the formation of collagen-induced collective cell invasion in MDA-MB-231 TNBC cells (MDAs), which are considered highly enriched for CSCs, with over 90% of the total population expressing $CD44^{+}/CD24^{low/-}$ (Fig. 3.1a).(Fillmore & Kuperwasser, 2008) A small percentage of MDAs formed non-invasive spheroids, revealing phenotypic heterogeneity that was not observed in other *in vitro* model systems (Fig. 3.1b). Gene ontology analysis of the collective invasion cell state revealed enrichment of genes involved in several biological processes, including blood vessel development and regulation of migration(D. O. Velez et al., 2017). Within these two process categories, and relevant to cancer stemness, were several Notch pathway members. Expression of RBPJ, JAG1, LFNG, NOTCH1, NOTCH2, and HES1 in HD Col1 was distinct compared to other typical culture systems (Fig. 3.1c). Together, this data suggests that HD Col1

induces a distinctive Notch state that is associated with more aggressive clinical disease(D. O. Velez et al., 2017). Based on these findings, we next asked how collagen-induced CCI was distinctly regulated by Notch. γ-secretase inhibitors (GSIs), which effectively inhibit Notch activation, have previously entered phase I/II clinical trials for patients with advanced or metastatic breast cancer targeted at the small population of highly invasive cancer stem cells (CSCs). However, the clinical efficacy of these inhibitors has been modest to null so far(Yang *et al.*, 2020). To assess how cells responded in HD Col1 to GSI, MDAs were treated with two distinct GSIs, DAPT and MK-0752, and assessed for migrational differences ~48 hours after seeding. Rather surprisingly, cells exhibited increased maximum invasion distances in both GSI treatments (Fig. 3.1d). Consistently, GSI treatment increased collective cell invasion after 7 days in culture (Fig. 3.1e). Notch inhibition via GSI was validated by downregulation of HES1 with 24 hours of treatment (Fig. 3.1f). These data demonstrate that Notch pathway inhibition can promote the acquisition of an increased collective invasion phenotype.

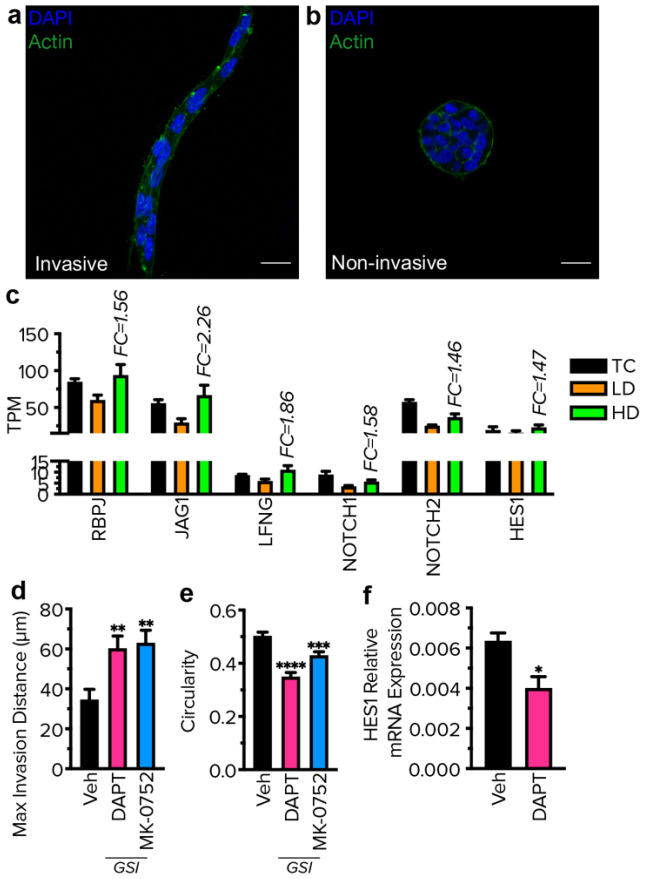


Figure 3.1. MDAs seeded in HD Col1 undergo both (a) invasive collective migration and (b) non-invasive collective migration over the course of 7 days. Scale bar, 25μm. (c) Comparison of Notch pathway gene expression in MDAs cultured on tissue culture plastic (TC), in low density collagen 1 (LD Col1), or in high density collagen 1 (HD Col1). Fold-Change (FC) is calculated in the HD Col1 with respect to the LD Col1 condition. (d) Maximum invasion distance of MDAs in HD Col1 treated with vehicle (0.1% DMSO) or GSIs DAPT and MK0752. (e) Circularity of collectively invading structures of MDAs in HD Col1 treated with vehicle (0.1% DMSO) or GSIs DAPT and MK0752 for 7 days. (f) RT-qPCR of HES1 relative expression in MDAs treated with vehicle or DAPT for 24 hours in HD Col1.

3.2.2 Targeting the HD Collagen-induced cancer cell state for differentiation and MET.

Previous work has shown that multipotent notch-activated adult stem cells respond to isoxazole derivatives by driving key differentiation programs across various normal cell types and biological processes.(Russell et al., 2012; Schneider et al., 2008, 2012) We explored if isoxazole derivatives could similarly induce differentiation of CSCs occupying the clinically relevant notch-activated state that our HD Col1 model system confers (Fig. 3.1c). Numerous commercially available lead-like Isoxazole analogs (labeled CR1-CR8) were profiled for their

potential to differentiate TNBC CSCs in HD Collagen I. We approached the screening by using mRNA expression changes to the CSC marker *CD24* as the primary molecular readout and collective invasion as a secondary phenotypic assay. MDAs were seeded as single cells in HD Col1 in a 96-well plate, treated with test compounds daily for 7 days, and measured for mRNA expression changes. Screening of Isoxazole derivatives for their ability to induce a minimum 2-fold upregulation of CD24 after 48 hours yielded two hits, CR-1 and CR-8, which were able to induce a ~7-fold and ~21-fold upregulation of *CD24,* respectfully (Fig. 3.2a). To validate that the drug response does not result from off-target cytotoxicity, we multiplexed CellTiter-Fluor™ and CytoTox-Fluor™ assays, which measure metabolic activity and cytotoxicity, respectively (Fig. 3.2b). In MDAs treated with CR-8 in 2D, there was an upregulation of CD24 mRNA without any observable increase in cytotoxicity for a concentration range between 1-40μM. Between concentrations of 10-40μM, there was also a decrease in metabolic activity without an equivalent increase in cytotoxicity, which is consistent with cell cycle arrest from cell differentiation. Given that the drug response did not result from off-target cytotoxicity, we next assessed the generality of our findings. Treatment screening of several different TNBC cell lines with CR-8 in 2D for 48h yielded four responders, as determined by CD24 mRNA expression (Fig. 3.2c). The BT-549 (FC~12.6), MDA-MB-436 (FC~7.1), MDAs (FC~31.6) and SUM149 (FC~2.7) all showed significant upregulation of CD24, but the MDA-MB-468 (FC~0.6) showed a significant but small downregulation of CD24. Interestingly, the two cell lines with the least response to CR-8, SUM149 and MDA-MB-468, contain Notch1 mutations that would be expected to change the functionality of the protein.(*DepMap: The cancer dependency map project at broad institute*, n.d.) As a secondary phenotypic readout, we assessed whether isoxazole derivatives were capable of abrogating the collective invasion of MDAs in HD Col1. Tumor cells were seeded

individually and treated daily with a compound titration. The invasion responses were measured by the Feret diameter of the structures, with increased diameters representing increased invasion of collective architectures. The results of this screen also found that CR-8 was able to significantly diminish the invasive capacity of TNBC cells (Fig 3.2d, e). We next asked how the Notch pathway responded to CR-8 treatment. MDAs treated with CR-8 for 24h in HD Col1 significantly increased their expression of Notch pathway genes (Fig. 3.2f). Based on the Notch expression profiles of MDAs in our model system (Fig. 3.1c), we hypothesized that Notch1 could be involved in this response. Immunofluorescent staining for activated Notch1, i.e. the cleaved intracellular domain, showed strong nucleolar localization in CR-8 treated cells compared to vehicle treated cells, even in 2D culture (Fig. 3.2g). These results suggest that two distinct isoxazole derivatives may have the capacity to differentiate TNBC tumor cells and that Notch1 activation contributes to the response.

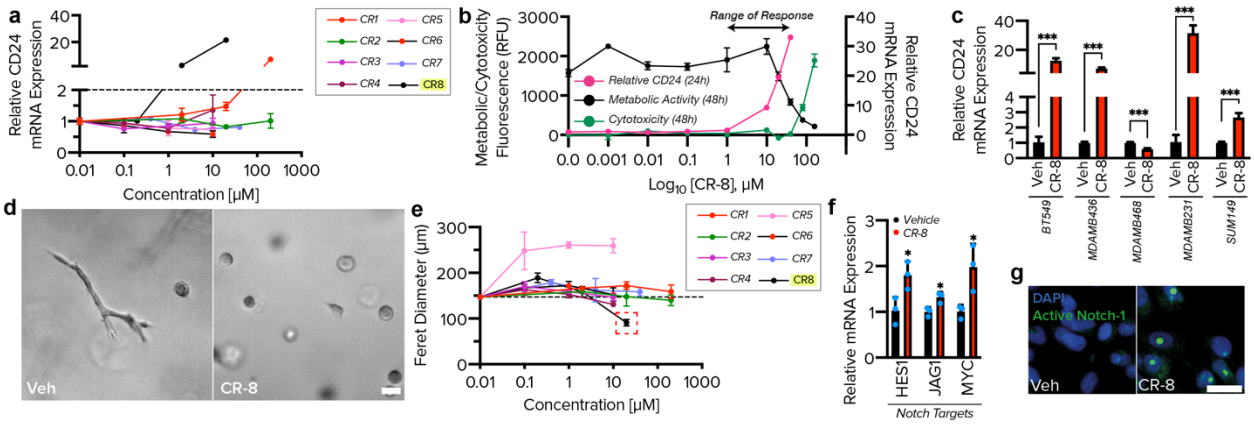


Figure 3.2. (a) Screening of Isoxazole analogs for MDA differentiation, as measured by upregulation of CD24 mRNA (FCthreshold=2.0). (b) Metabolic activity, cytotoxicity, and relative CD24 expression dose-response to CR-8. (c) CD24 expression in 2D across several TNBC cell lines when treated with CR-8. (d) Brightfield microscopy images of MDAs at 7 days of culture in HD Col1 treated with vehicle or CR-8. Scale bar, 50μm. (e) Screening of Isoxazole analogs for loss of collective invasion, as measured by average feret diameter. (f) RT-qPCR gene expression analysis of Notch target genes in vehicle and CR-8 treated MDAs. (g) Immunofluorescence staining of cell nuclei (blue) and cleaved intracellular domain of Notch1 (green) in vehicle and CR8 treated MDAs. Scale bar, 25μm.

3.2.3 CR8 induces MET and chemo-sensitivity in HD Col1 but not in 2D culture

Given that HD Col1 induced a distinctive Notch state in comparison to 2D tissue culture and 3D 2.5 mg/ml (LD Col1) culture, we next investigated if there may be any differences in the CR8 treatment response between cells in these culture conditions. We first assessed the populational expression of $CD44^{+}/CD24^{-}$ CSC cells in response to CR-8 treatment. Cells in 2D tissue culture and HD Col1 were treated with CR-8 daily for 7 days, dissociated and flow-sorted. Fluorescence-activated cell sorting (FACS) analysis showed that cells treated in 2D and HD Collagen I were able to upregulate $CD24^{+}$ expression, thereby reducing the population of $CD44^{+}/CD24^{-}$ CSCs (Fig. 3.3a-c). To understand whether CR-8 treatment could induce MET, we first performed western blotting (WB) for the epithelial marker E-Cadherin (E-Cad) and the Mesenchymal marker Vimentin (Vim) on 2D and HD Collagen-treated tumor cells (Fig. 3.3d). CR-8 induced an increase in E-Cadherin and decrease in Vimentin in HD Col1-treated cells. Rather surprisingly, there was no effect on either MET marker in 2D-treated cells. To determine whether induction of MET was specific to the HD Collagen I condition or generally applicable to all CR-8-treated cells in a 3D Collagen condition, we flow-sorted CDH1+ cells in 2D, and in increasing densities of 3D Collagen I (1 mg/mL, 2.5 mg/mL, and 6 mg/mL Col1) (Fig. 3.3e, f). In good accordance with the WB data, cells in the HD (6mg/mL) Col1 condition had the highest population of $CDH1^{+}$ cells when treated with CR-8, while CR-8 treatment of cells on 2D had a small effect to $CDH1^{+}$ cells. We further assessed CR-8-treated cells in 1 mg/mL and 2.5mg/mL Col1 conditions for $CDH1^{+}$ induction and found cells were unable to re-express $CDH1^{+}$ to similar levels as the 6 mg/mL condition. These data demonstrate that the HD Collagen I condition renders cells into a distinct state that allows for increased sensitivity to differentiation treatment with CR-8.

Differentiation therapy renders CSCs more sensitive to a range of chemotherapeutics(Pattabiraman *et al.*, 2016), and has been successfully implemented in acute promyelocytic leukemia with the combination of retinoic acid and arsenic(de Thé, 2018). To determine whether CR-8 can be used in a similar therapeutic function, MDA cells were treated with vehicle or CR-8 for 7d in 2D and HD Col1, followed by doxorubicin for 3 days and MTS assay to quantify viable cells (Fig. 3.3g, h). MDAs exhibited a ~14.5-fold decrease in IC_{50} to doxorubicin in HD Col1, but exhibited a negligent increase in 2D-treated cells. These findings suggest a utility for CR-8 as a means to increase sensitivity to traditional chemotherapy, and also suggest that these on-target effects may be context-dependent.

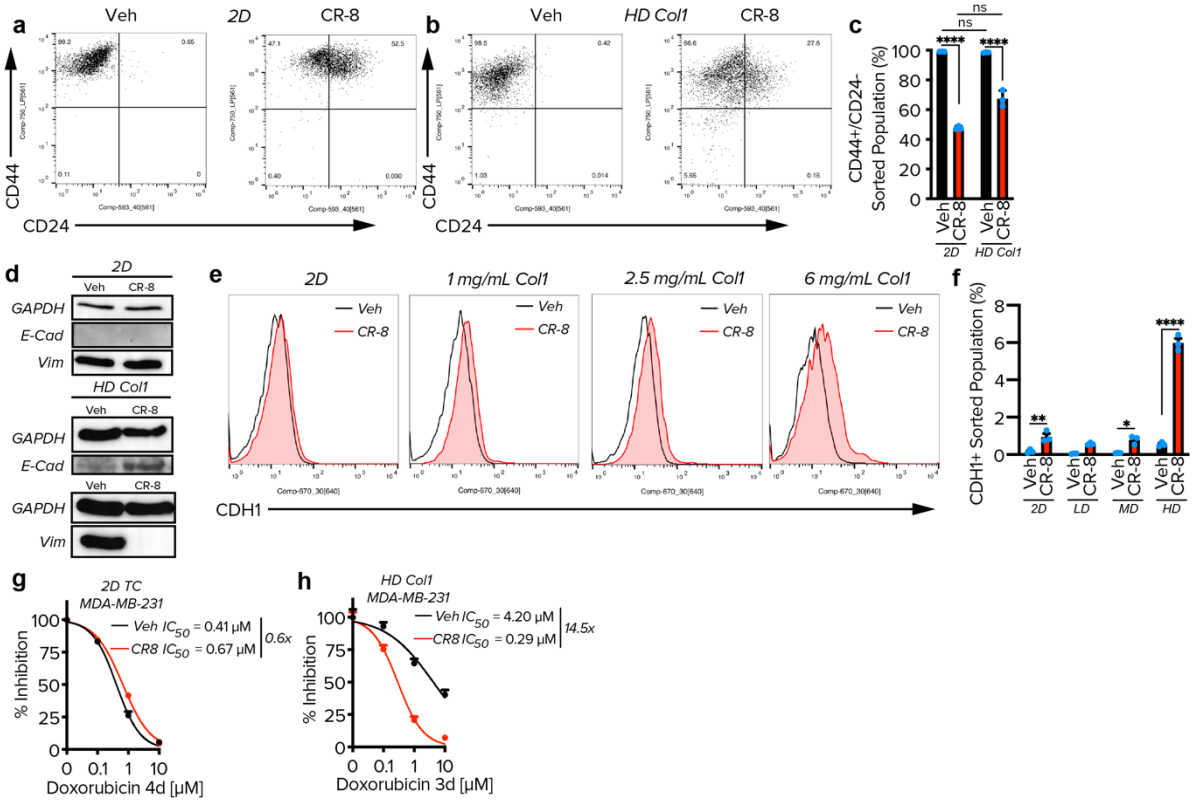


Figure 3.3. Fluorescence profiles of CD44/CD24 in MDAs treated with vehicle or CR-8 for 7 days in (a) 2D TC or (b) HD Col1. (c) Flow cytometry analysis of $CD44^+/CD24^-$ MDA cells treated with vehicle or CR-8. (d) Western blot analysis of EMT markers E-cadherin and Vimentin in MDAs treated with vehicle or CR-8 for 7 days in 2D TC or HD Col1. (e) Fluorescence profiles of CDH1 in MDAs treated with vehicle or CR-8 for 7 days in 2D TC, 1 mg/mL Col1, 2.5 mg/mL Col1, or 6 mg/mL Col1 (HD) conditions. (f) Flow cytometry analysis of $CDH1^+$ MDA cells treated with vehicle or CR-8 in 2D TC, 1 mg/mL Col1, 2.5 mg/mL Col1, or 6 mg/mL Col1 (HD) conditions. Sensitivity to treatment with doxorubicin in (g) 2D TC-cultured or (h) HD Col1-cultured MDAs pre-treated with vehicle or CR-8 for 7 days.

3.3 Future Directions

3.3.1 CR8 activates Notch, but is not essential for differentiation in HD Col1

We also asked whether the Notch pathway was essential for the differentiation response with CR-8 treatment. We first pretreated MDAs with DAPT in 2D culture for 6, 12, 24 and 48 hours and identified via WB that a significant reduction in activated Notch1 was found after 48 hours of pretreatment (Fig. 3.4a). Pretreated DAPT and vehicle cells were then embedded in HD Col1 and co-treated with either vehicle or CR-8 for 7 days in 4 total treatment conditions: Veh, CR-8, DAPT, DAPT+CR-8 (Fig. 3.4b). Surprisingly, we found that pretreatment with DAPT was insufficient in inhibiting the CR8-induced increase in $CDH1^{+}$ cells (Fig. 3.4c-d). Given its suggested role in breast cancer and upregulation in HD Col1, we next interrogated the function of Notch1 in promoting CCI.(Stylianou et al., 2006) We conducted knockouts of Notch1 in MDA-MB-231 cells and found that consistent with GSI treatment, shNotch1 cells formed more invasive collective morphologies in comparison to no template control (NTC) cells (Fig. 3.4e-g). Interestingly, treatment with CR-8 was unable to rescue this increase in collective invasion (Fig. 3.4h). However, we also treated NTC and shNotch1 MDAs with vehicle or CR8 and found that knockdown of Notch1 was also unable to inhibit the CR8-induced increase in CDH1+ cells (Fig. 3.4i-j). These data suggested that canonical Notch signaling is not an essential component for the CR8-induced MET response. Nonetheless, evidence suggests that non-canonical Notch signaling is also possible, including crosstalk with the Wnt signaling pathway(Andersen *et al.*, 2012). In future work, we plan to continue to identify the mechanism of action (MOA) of CR-8 induced differentiation, including identifying the drug target(s). Given the multiple interaction points in the Notch signaling pathway, we propose to conduct an unbiased chemoproteomics approach for identification of the molecular target(s) of CR-8. Briefly, we will explore the use of quantitative

proteomics in combination with affinity enrichment to identify proteins that bind to the lead compound(Ong et al., 2009; Szardenings et al., 2004). Follow-up CRISPR knockout screens of proteomics-identified binding partners may be conducted, if deemed necessary.

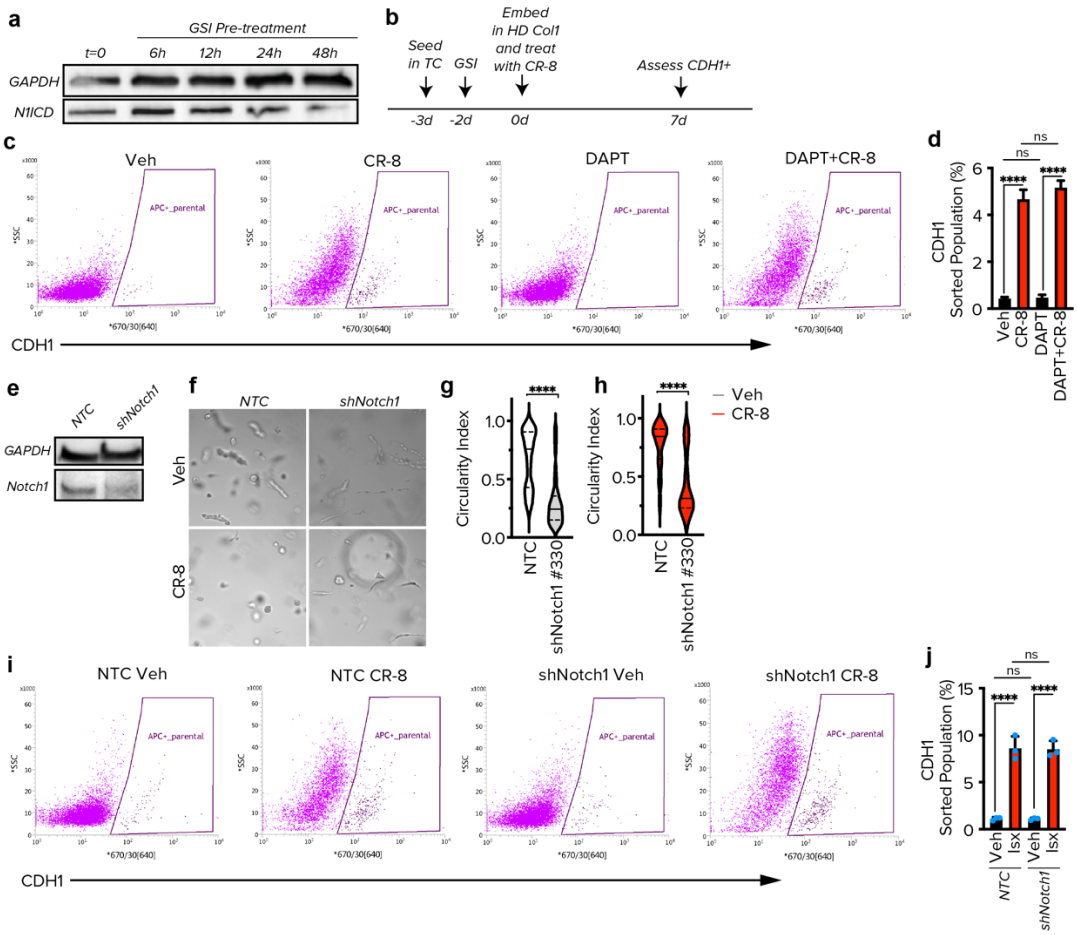


Figure 3.4. (a) WB assessment of active Notch1 (N1ICD) in MDAs pretreated with DAPT in 2D culture for 6, 12, 24 and 48 hours. (b) Experimental schematic of DAPT pretreatment in 2D followed by CR-8 treatment in HD Col1. Flow cytometry (c) fluorescence profiles and (d) analysis of CDH1+ cells in 4 total treatment conditions: Veh, CR-8, DAPT, DAPT+CR-8. (e) WB validation of Notch1 knockout in MDAs with shRNA. (f) Brightfield microscopy images of NTC or shNotch1 cells at 7 days of culture in HD Col1 treated with vehicle or CR-8. Violin plots of circularity of collectively invading structures of NTC or shNotch1 MDAs in HD Col1 treated with (g) vehicle or (h) CR-8 for 7 days. Flow cytometry (i) fluorescence profiles and (j) analysis of CDH1+ cells in NTC or shNotch1 MDAs in HD Col1 treated with vehicle or CR-8 for 7 days.

3.3.2 3D High Density Collagen mimics aggressive TNBC by shifting the EMT differentiation state of cells

To better characterize how our *in vitro* model may predict patient response to differentiation therapy with CR-8, we plan to also explore how toggling Collagen I density may

induce distinct hybrid E/M transcriptional states that match that of distinct TNBC patient samples. We have conducted some preliminary investigations of mesenchymal-like TNBC MDA-MB-231 (MDAs) embedded in three Collagen I densities mimicking the ranges found within normal to cancerous breast tissue: 1.0 mg ml^{-1}(LD), 2.5 mg ml^{-1}(MD), and 6 mg ml^{-1}(HD).(Fraley et al., 2015; Kumar & Weaver, 2009) Briefly, global changes in gene expression were measured by RNA-Sequencing (RNA-Seq) of MDAs embedded as single cells for 24 hours in Collagen I gel conditions and on a 2D tissue culture plate. To identify enriched transcriptional programs, we built a co-expression network from the 3000 most variable genes across all samples using a weighted gene co-expression network analysis (WGCNA) (Fig 3.5a). We identified six co-expression modules from this network, performed gene ontology (GO) and selected the top two GO terms for each module. Of the 12 GO terms across 6 modules, the only notable hallmarks relating to CSCs was an enrichment for the Epithelial-to-Mesenchymal Transition, identified by MSigDB, which was found across three modules (Fig. 3.5b, labeled as Brown, Green, Yellow). To assess how these modules enriched for the Col1 conditions, we calculated correlations between each module's representative eigengene and each density (Fig. 3.5c). Notably, the HD condition was significantly correlated with eigengenes for all three modules enriched for EMT, while the only enrichment within the LD and MD conditions was a negative correlation between the LD and brown module. To further investigate how HD Col1 shifted MDAs along the E/M spectrum, we compared the HD vs 2D gene expression using a published set of pan-cancer EMT markers labeled for epithelial or mesenchymal states (Fig. 3.5d). We generally observed that E/M genes were differentially expressed between 2D and HD conditions, but surprising we did not observe a trend towards epithelial or mesenchymal enrichment. A closer evaluation of differentially expressed genes using DeSeq2 revealed that in

contrast to 2D-plated tumor cells, HD Col1 tumor cells presented a strong upregulation of many mesenchymal genes – including Vim, Snai1 – as well as upregulation of many epithelial genes – including Cldn4, Krt14 and Krt17 (Fig. 3.5e).(Love et al., 2014) Similarly, 2D-plated tumor cells expressed a high level of mesenchymal genes (such as ZEB1, CDH11), while continuing to express a high level of epithelial genes (such as CLDN1, LAMA5), when compared to HD Col1 tumor cells. These data suggested to us that TNBC cells in 2D and HD Col1 occupied distinct hybrid E/M states. Given our understanding of MDAs responsiveness to CR-8 in HD Col1 versus all other conditions, our observations suggest that this distinct hybrid E/M states may represent the native state of an aggressive hybrid "mesenchymal" TNBC tumor. In follow-up studies, we would like to explore whether we may be able to map the hybrid E/M states *in vitro* to specific transcriptional states of TNBC tumors.

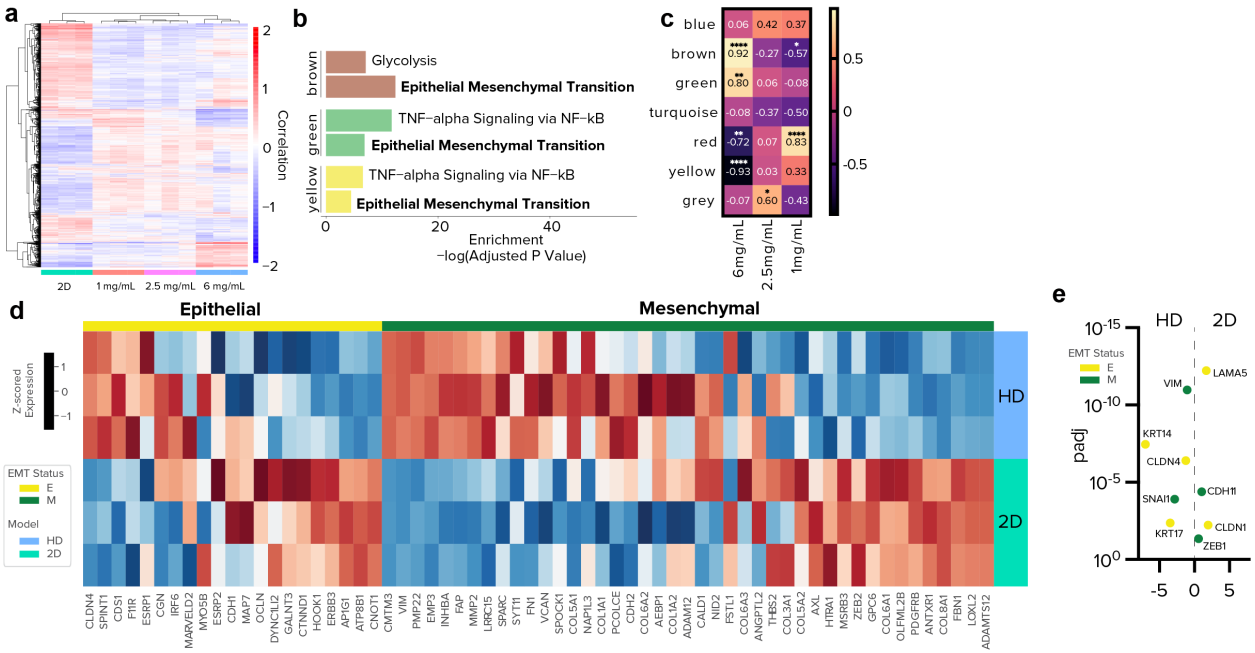


Figure 3.5. (a) Hierarchical clustering dendrograms of samples by transcriptomes. (b) Top two GO terms enriched in brown, green and yellow gene modules from WGCNA include Epithelial Mesenchymal Transition. (c) Correlation coefficients between each module's representative eigengene and each respective Collagen I matrix condition. (d) Heatmap comparison of epithelial- and mesenchymal-labeled relative mRNA expression in HD Col1 (top 3) and 2D TC (bottom 3) conditions. (e) Quantification of differentially-expressed EMT genes identified by DE-Seq2 analysis of HD Col1 vs. 2D TC conditions.

3.3.3 Preliminary data suggests CR-8 responsiveness in pancreatic ductal adenocarcinoma

Similar to TNBC, pancreatic ductal adenocarcinoma (PDAC) is a highly aggressive form of cancer with a characteristic abundant stroma.(Hosein et al., 2020) Evidence suggests that PDAC tumor samples with this "active" stromal subtype is prognostic of worse survival.(Moffitt *et al.*, 2015) Given the similarities in the stromal tumor environment between these two highly aggressive forms of cancer, TNBC and PDAC, we also explored whether CR-8 may induce differentiation of PDAC cells. Preliminary evidence in the murine R40P PDAC cell line suggests that treatment with CR-8 for 7 days in HD Col1 showed significant abrogation of the CCI capability of cells (Fig. 3.6a). Given the strong phenotypic changes induced by CR-8 in HD Col1, we proceeded to assess the differentiation activity of CR-8 by characterizing Epithelial-to-Mesenchymal (EMT) status using western blot (WB) analysis of E-cadherin and vimentin levels. Fig. 3.6b shows that CR-8 treatment increased E-cadherin expression and reduced vimentin expression after 7 days in HD Col1, suggesting that CR-8 induced MET and differentiation. To determine whether CR-8 can be used in a similar therapeutic function, R40P cells were treated with vehicle or CR-8 for 7d in HD Col1, followed by chemotherapy for 3d and MTS assay to quantify viable cells. R40Ps showed increases in chemo-sensitivity to gemcitabine, when normalized to the vehicle control (Fig. 3.6c). These findings provide a strong groundwork for follow-up studies exploring in parallel both the relevance of CR-8 treatment in patient-derived PDAC samples, as well as, identification of whether the MOA is similar to TNBC. Given the limited treatment options for PDAC and 12% 5-year overall survival in the USA, all possible new therapeutic options for this disease should be explored.(*Cancer Facts & Figures 2023*, n.d.)

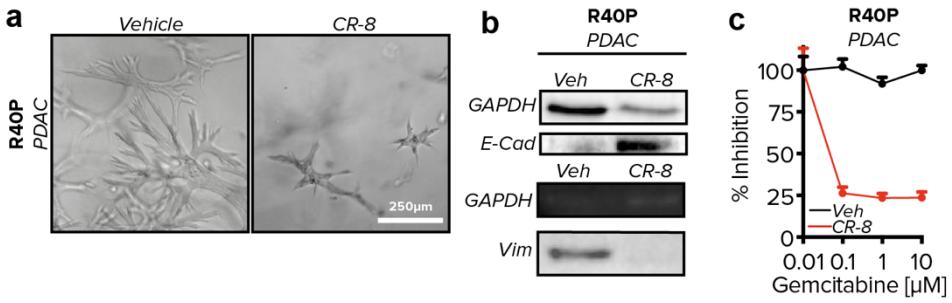


Figure 3.6. (a) Brightfield microscopy images of R40P PDAC cell line at 7 days of culture in HD Col1 treated with vehicle or CR-8. Scale bar = 250um. (b) Western blot analysis of EMT markers E-cadherin and Vimentin in R40Ps treated with vehicle or CR-8 for 7 days in HD Col1. (c) CR8-treated R40Ps acquire increased sensitivity to 3 days of treatment with gemcitabine when pretreated with CR-8 in HD Col1 for 7 days.

3.4 Methods

3.4.1 Cell Culture

MDA-MB-231 TNBC cells were purchased from ATCC. MDA-MB-468 and BT-549 cells were provided by Richard Kolodner (UCSD). SUM-149 and MDA-MB-436 cells were provided by Gene Yeo (UCSD). R40P cells were provided by David Cheresh (UCSD). MDA-MB-231, MDA-MB-468, and R40P were cultured in high glucose Dulbecco's modified Eagle's medium (DMEM, Gibco), supplemented with 10% fetal bovine serum (FBS, Corning) and 0.1% gentamicin (Thermo Fisher Scientific). MDA-MB-436 were cultured in high glucose Dulbecco's modified Eagle's medium (DMEM, Gibco), supplemented with 10% fetal bovine serum (FBS, Corning), 10μg/mL insulin (Sigma Aldrich) and 0.1% gentamicin (Thermo Fisher Scientific). SUM-149 were cultured in Ham's F-12 medium (Gibco), supplemented with 5% fetal bovine serum (FBS, Corning), 5μg/mL insulin (Sigma Aldrich), 1μg/mL hydrocortisone (Sigma-Aldrich) and 0.1% gentamicin (Thermo Fisher Scientific). BT-549 were cultured in RPMI 1640 medium (Gibco), supplemented with 10% fetal bovine serum (FBS, Corning) and 0.1% gentamicin (Thermo Fisher Scientific). All cell lines were maintained at 37°C and 5% CO_2 in a humidified environment.

3.4.2 3D Culture in Collagen I Matrices

Cells suspended in culture medium were embedded in 3D collagen I matrices by mixing with 10x reconstitution buffer (1:1 v/v) and high concentration, rat tail acid extracted type I collagen (Corning) to a final collagen I concentration of 1mg/mL, 2.5mg/mL or 6 mg/mL. The pH was adjusted using 1 N sodium hydroxide, and the mixture was added to 48-well culture plates at a final volume of 200 µL or to 96-well culture plates at a final volume of 60 µL. The mixture was polymerized by incubating at 37℃ for 30 min, and an equal volume of culture media was added to the top of the gels. For 7-day phenotype studies, media was replenished every other day or daily when treated with small molecules.

3.4.3 Cell Phenotypic Analysis

Cells embedded in HD collagen I gels 7 days after seeding were imaged on a Nikon Ti-Eclipse Epifluorescent Inverted Microscope. Brightfield z-stacks from the bottom to the top of the gel in 50 µm step sizes were acquired in 3 fields of view (FOV) per gel. Individual structures were traced and analyzed for Feret's diameter and/or circularity in ImageJ using the measurement tool as a readout of collective cell invasion.

3.4.4 RNA Isolation and Purification

RNA was harvested by homogenization in TRIzol reagent (Thermofisher, Waltham, MA) from 3D collagen I gels or 2D tissue culture plates according to manufacturer's instructions. Total RNA was isolated using a chloroform extraction according to manufacturer's instructions. RNA was purified using High Pure RNA Isolation Kit (ROCHE, Branford, CT) or PureLink RNA Mini Kit (Thermofisher, Waltham, MA).

3.4.5 RNA Sequencing

Bulk RNA-Sequencing data is from previous work conducted in our lab.(D. O. Velez et al., 2017) Briefly, MDAs were embedded in 3D Collagen I densities of 1mg/mL, 2.5mg/mL and

6mg/mL and harvested for RNA 24 hours after seeding. MDAs from 2D tissue culture were also harvested for comparison. Bulk RNA-Sequencing was performed using the Illumina MiSeq platform at a depth of >25 million reads per sample and aligned using Bowtie2 and streamed to eXpress for transcript abundance quantification. We used transcripts per million (TPMs) as a measurement of gene expression. For our differential expression workflow, we used DeSeq2 using the TPMs as input.(Love et al., 2014)

3.4.6 High-Throughput Drug Screen

Three independent replicates of 3D collagen I gels were seeded in a 96-well plate at 100,000 MDAs per gel per condition tested. Cells were seeded individually in HD Col1 in a 96-well plate, treated with test compounds daily for 7 days, and measured for mRNA expression changes. High-throughput RT-qPCR was conducted to assess CD24 expression relative to a negative (vehicle) control. Dose response plots were generated by applying each compound to cells at four different concentrations ranging from 0nM to 200μM, with a minimum 100-fold concentration range. The highest concentration was selected based on the max solubility of the compound in DMSO, without exceeding a final DMSO concentration of 0.2%.

3.4.7 Quantitative Real-Time PCR (RT-qPCR)

We extracted RNA and performed synthesis of cDNA using the SuperScript III first-strand synthesis system (Thermofisher, Waltham, MA). Relative abundances were calculated using the TaqMan assay system by normalizing first to the housekeeping control gene GAPDH, and then to the control sample (Thermofisher, Waltham, MA). The TaqMan assays used include: *GAPDH* (Hs02758991_g1)*, HES1, CD24* (Hs02379687_s1), *JAG1* (Hs01070032_m1)*, MYC,* and *CDH1* (Hs01023895_m1) (Thermofisher, Waltham, MA).

3.4.8 Fluorescence-Activated Cell Sorting (FACS)

3D Collagen I gels were digested using Collagenase at 37°C for 20 minutes, and filtered through a 35μm filter. Cells were centrifuged at 350xg and 4°C for 5 minutes before resuspending in 2% HI-FBS in PBS. Cells were incubated for 20 minutes at 4°C with the following antibodies: PE anti-human CD24 (1/40, 311105, Biolegend, San Diego, CA), PE/Cyanine7 anti-mouse/human CD44 (1/40, 103029 , Biolegend, San Diego, CA), and APC anti-mouse/human E-Cadherin (1/40, 147311, Biolegend, San Diego, CA). Following 2x 2% HI-FBS/PBS washes, cells were incubated for 10 minutes with DAPI (62248, Thermofisher, Waltham, MA), which was used as a dead cell dye. Samples were sorted at the stem cell core of Sanford Consortium of Regenerative Medicine (La Jolla, CA) on a BD Influx cell sorter (BD Biosciences, Franklin Lakes, NJ) and the data was analyzed within the FlowJo software. Experimental samples were compared to unstained and single stain controls.

3.4.9 Immunofluorescence imaging

Cells were fixed with 4% paraformaldehyde (Electron Microscopy Services) diluted in 1x PBS for 30 min at room temperature. Collagen gels were blocked overnight at 4℃ with a 1x PBS solution containing 1% w/v bovine serum albumin (BSA, Sigma-Aldrich), 2.5% v/v goat serum, 2.5% v/v FBS (Corning), and varying concentrations of Triton-X-100 (0.02-0.2% v/v). Primary antibody was diluted in antibody dilution buffer, which composed of 1x PBS with 1% w/v BSA (Sigma Aldrich), 2.5% v/v goat serum, 2.5% v/v FBS (Corning), and 0.02% v/v Triton-X-100 and incubated with hydrogels for 2 days at 4℃. Following PBS washes, Collagen gels were incubated with diluted secondary antibodies for 1 day at 4℃. For F-actin visualization, gels were incubated in phalloidin (1/20, 8878S, Cell Signaling Technologies) diluted in 1x PBS for 1-2 h at room temperature, protected from light with aluminum foil. DAPI (1/1000, 62248,

Thermo Fisher Scientific) was added for 10 min to counterstain nuclei. Primary antibodies: Anti-activated Notch1 antibody (1/250, ab52301, Abcam).

3.4.10 Western Blotting

3D Collagen I gels were digested using collagenase at 37°C for 20-30 minutes, and filtered through a 35µm filter. After a 1x PBS wash, cells were lysed using 200µL of RIPA lysis buffer (89900, Thermofisher, Waltham, MA) with 1x Halt Protease and Phosphatase Inhibitor Cocktail (78440, Thermofisher, Waltham, MA). 2D samples from a 6-well plate were also lysed using the same solution volumes and scraped thoroughly. Cell lysates were kept on ice and shaken every 5 minutes for a total of 30 minutes and kept in long-term storage at -20°C. Samples were prepared with 1x Bolt LDS Sample Buffer (NP0009, Thermofisher, Waltham, MA) and 1x NuPAGE Sample Reducing Agent (NP0009, Thermofisher, Waltham, MA) before loading. Antibodies that were used are GAPDH (1:1000, 2118s, Cell Signaling Technology, Danvers, MA), E-Cadherin (1:500, 13-5700, Thermofisher, Waltham, MA), Vimentin (1:250, ab92547, Abcam, Cambridge, UK), Anti-activated Notch1 antibody (1/500, ab52301, Abcam), Anti-Notch1 antibody (1/1000, ab52627, Abcam).

3.4.11 Cell Transfection

To generate MDA-MB-231 cells with stable Notch1 shRNA knockdown, we transfected the transfer plasmid into lentiX293 T cells (632180, Clonetech, Mountain View, CA.) along with the envelope expressing plasmid (pMD2.G, Addgene #11259) and the packaging expressing plasmid (psPAX2, Addgene #11260). The sample supernatant containing the viral particles were collected 48 hours after transfection and purified by filtration through a 0.45µm filter. MDA-MB-231 cells were transduced for 24 hours with the virus in the presence of 10µg/mL Polybrene reagent (TR-1003-G, Millipore Sigma). Selection of stably transduced cells was carried out by

supplementing with puromycin (4µg/mL) for at least 5 days. The target sequence of Notch1 shRNA (TRCN0000350330, Sigma Aldrich) was: CCGGGACATCACGGATCATAT.

3.4.12 Maximum Invasion Distance Analyses

MDA cells in a seeding density of 25,000 were embedded in HD Collagen I in a 48-well plate and immediately treated with vehicle, 20µM DAPT or 1µM MK-0752. Following 44 hours of culture, the plate was transferred to a microscope stage top incubator on a Nikon Ti-E inverted microscope and live cell brightfield imaging was performed with images acquired using a 10x objective at 10 minute intervals for 48 hours. We analyzed cell coordinates using Metamorph Software (Molecular Devices) to generate xy-trajectories and calculated the maximum linear distance traveled from the cell's starting position to any point within the timelapse video.

3.4.13 Drug Treatments

For GSI experiments, cells were treated with 20µM DAPT (Cell Signaling Technology), 1µM MK-0752 (MedChemExpress), or 0.1% DMSO daily in HD Collagen I. For 2D and HD Collagen I differentiation treatments with CR-8, cells were treated with either 0.025% DMSO or 20µM CR-8 for 7 days. Cells in 2D culture were split at a ratio of 1:3-1:4 every 2-3 days during CR-8 drug treatment. For induction of chemosensitivity cells were treated with gemcitabine or doxorubicin in a 4-point dose response for 3 days following 7 days of 20µM CR-8 treatment. CR-8 was removed from cells during chemotherapy treatment.

3.4.14 Statistical Analyses

Statistical significance was determined by unpaired two-sided t-test and ordinary one-way ANOVA with Tukey post-hoc tests for multiple comparisons and is indicated as *, **, *** , **** for $p \leq 0.05$, $p \leq 0.01$, $p \leq 0.001$, $p \leq 0.0001$, respectively. All error bars represent standard error of the mean.

3.5 Acknowledgements

Chapter 3, in part is currently being prepared for submission for publication of the material. Ranamukhaarachchi, S. K., Klie, A., Turner, J., Simon, J., Lam, S., Ghosh, P., Carter, H., Fraley, S.I. The dissertation author was the primary researcher and author of this material.

We thank members of the Fraley lab for their technical assistance and insightful comments regarding this work.

REFERENCES

& Others. Global Health Estimates 2020: Deaths by Cause, Age, Sex, by Country and by Region. (2000). World Health Organization.

Ahmed, K. M. (2017). Three-Dimensional Culture. In M. Schwab (Ed.), *Encyclopedia of Cancer* (pp. 4511–4518). Springer Berlin Heidelberg.

Andersen, P., Uosaki, H., Shenje, L. T., & Kwon, C. (2012). Non-canonical Notch signaling: emerging role and mechanism. *Trends in Cell Biology*, *22*(5), 257–265.

Antman-Passig, M., Levy, S., Gartenberg, C., Schori, H., & Shefi, O. (2017). Mechanically oriented 3D collagen hydrogel for directing neurite growth. *Tissue Engineering. Part A*, *23*(9–10), 403–414.

Aragona, M., Panciera, T., Manfrin, A., Giulitti, S., Michielin, F., Elvassore, N., Dupont, S., & Piccolo, S. (2013). A mechanical checkpoint controls multicellular growth through YAP/TAZ regulation by actin-processing factors. *Cell*, *154*(5), 1047–1059.

Banerjee, P., Lenz, D., Robinson, J. P., Rickus, J. L., & Bhunia, A. K. (2008). A novel and simple cell-based detection system with a collagen-encapsulated B-lymphocyte cell line as a biosensor for rapid detection of pathogens and toxins. *Laboratory Investigation; a Journal of Technical Methods and Pathology*, *88*(2), 196–206.

Bao, M., Xie, J., Piruska, A., & Huck, W. T. S. (2017). 3D microniches reveal the importance of cell size and shape. *Nature Communications*, *8*(1). https://doi.org/10.1038/s41467-017-02163-2

Bateman, J. F., Cole, W. G., Pillow, J. J., & Ramshaw, J. A. (1986). Induction of procollagen processing in fibroblast cultures by neutral polymers. *The Journal of Biological Chemistry*, *261*(9), 4198–4203.

Bauer, K. R., Brown, M., Cress, R. D., Parise, C. A., & Caggiano, V. (2007). Descriptive analysis of estrogen receptor (ER)-negative, progesterone receptor (PR)-negative, and HER2-negative invasive breast cancer, the so-called triple-negative phenotype: a population-based study from the California cancer Registry. *Cancer*, *109*(9), 1721–1728.

Bezrukov, S. M., Vodyanoy, I., & Parsegian, V. A. (1994). Counting polymers moving through a single ion channel. *Nature*, *370*(6487), 279–281.

Bleau, A.-M., Hambardzumyan, D., Ozawa, T., Fomchenko, E. I., Huse, J. T., Brennan, C. W., & Holland, E. C. (2009). PTEN/PI3K/akt pathway regulates the side population phenotype and ABCG2 activity in glioma tumor stem-like cells. *Cell Stem Cell*, *4*(3), 226–235.

Braun, S., & Naume, B. (2005). Circulating and disseminated tumor cells. *Journal of Clinical Oncology: Official Journal of the American Society of Clinical Oncology*, *23*(8), 1623–1626.

Bray, F., Laversanne, M., Weiderpass, E., & Soerjomataram, I. (2021). The ever-increasing importance of cancer as a leading cause of premature death worldwide. *Cancer*, *127*(16), 3029–3030.

Bredfeldt, J. S., Liu, Y., Pehlke, C. A., Conklin, M. W., Szulczewski, J. M., Inman, D. R., Keely, P. J., Nowak, R. D., Mackie, T. R., & Eliceiri, K. W. (2014). Computational segmentation of collagen fibers from second-harmonic generation images of breast cancer. *Journal of Biomedical Optics*, *19*(1), 16007.

Cancer Facts & Figures 2023. (n.d.). Retrieved June 1, 2023, from https://www.cancer.org/research/cancer-facts-statistics/all-cancer-facts-figures/2023-cancer-facts-figures.html

Carey, S. P., Martin, K. E., & Reinhart-King, C. A. (2017). Three-dimensional collagen matrix induces a mechanosensitive invasive epithelial phenotype. *Scientific Reports*, *7*(1), 42088.

Ceballos, D., Navarro, X., Dubey, N., Wendelschafer-Crabb, G., Kennedy, W. R., & Tranquillo, R. T. (1999). Magnetically aligned collagen gel filling a collagen nerve guide improves peripheral nerve regeneration. *Experimental Neurology*, *158*(2), 290–300.

Cetera, M., Ramirez-San Juan, G. R., Oakes, P. W., Lewellyn, L., Fairchild, M. J., Tanentzapf, G., Gardel, M. L., & Horne-Badovinac, S. (2014). Epithelial rotation promotes the global alignment of contractile actin bundles during Drosophila egg chamber elongation. *Nature Communications*, *5*, 5511.

Chaudhuri, O., Koshy, S. T., Branco da Cunha, C., Shin, J.-W., Verbeke, C. S., Allison, K. H., & Mooney, D. J. (2014). Extracellular matrix stiffness and composition jointly regulate the induction of malignant phenotypes in mammary epithelium. *Nature Materials*, *13*(10), 970–978.

Chen, C., Loe, F., Blocki, A., Peng, Y., & Raghunath, M. (2011). Applying macromolecular crowding to enhance extracellular matrix deposition and its remodeling in vitro for tissue engineering and cell-based therapies. *Advanced Drug Delivery Reviews*, *63*(4–5), 277–290.

Chen, K., Ozturk, K., Contreras, R. L., Simon, J., McCann, S., Chen, W. J., Carter, H., & Fraley, S. I. (2021). Phenotypically supervised single-cell sequencing parses within-cell-type heterogeneity. *IScience*, *24*(1), 101991.

Chin, A. S., Worley, K. E., Ray, P., Kaur, G., Fan, J., & Wan, L. Q. (2018). Epithelial Cell Chirality Revealed by Three-Dimensional Spontaneous Rotation. *Proceedings of the National Academy of Sciences of the United States of America*, *115*(48), 12188–12193.

Choi, C. K., Vicente-Manzanares, M., Zareno, J., Whitmore, L. A., Mogilner, A., & Horwitz, A. R. (2008). Actin and alpha-actinin orchestrate the assembly and maturation of nascent adhesions in a myosin II motor-independent manner. *Nature Cell Biology*, *10*(9), 1039–1050.

Conklin, M. W., Eickhoff, J. C., Riching, K. M., Pehlke, C. A., Eliceiri, K. W., Provenzano, P. P., Friedl, A., & Keely, P. J. (2011). Aligned collagen is a prognostic signature for survival in human breast carcinoma. *The American Journal of Pathology*, *178*(3), 1221–1232.

Conlon, N., Sadri, N., Corben, A. D., & Tan, L. K. (2016). Acinic cell carcinoma of breast: morphologic and immunohistochemical review of a rare breast cancer subtype. *Human Pathology*, *51*, 16–24.

Coughlin, M. F., & Stamenović, D. (1998). A tensegrity model of the cytoskeleton in spread and round cells. *Journal of Biomechanical Engineering*, *120*(6), 770–777.

Das, A., Monteiro, M., Barai, A., Kumar, S., & Sen, S. (2017). MMP proteolytic activity regulates cancer invasiveness by modulating integrins. *Scientific Reports*, *7*(1). https://doi.org/10.1038/s41598-017-14340-w

de Thé, H. (2018). Differentiation therapy revisited. *Nature Reviews. Cancer*, *18*(2), 117–127.

Depalle, B., Qin, Z., Shefelbine, S. J., & Buehler, M. J. (2015). Influence of cross-link structure, density and mechanical properties in the mesoscale deformation mechanisms of collagen fibrils. *Journal of the Mechanical Behavior of Biomedical Materials*, *52*, 1–13.

DepMap: The cancer dependency map project at broad institute. (n.d.). Retrieved September 14, 2022, from https://depmap.org/portal/

Dewavrin, J.-Y., Hamzavi, N., Shim, V. P. W., & Raghunath, M. (2014). Tuning the architecture of three-dimensional collagen hydrogels by physiological macromolecular crowding. *Acta Biomaterialia*, *10*(10), 4351–4359.

Dingli, D., & Michor, F. (2006). Successful therapy must eradicate cancer stem cells. *Stem Cells (Dayton, Ohio)*, *24*(12), 2603–2610.

Dongre, A., & Weinberg, R. A. (2019). New insights into the mechanisms of epithelial-mesenchymal transition and implications for cancer. *Nature Reviews. Molecular Cell Biology*, *20*(2), 69–84.

Dubey, N., Letourneau, P. C., & Tranquillo, R. T. (2001). Neuronal contact guidance in magnetically aligned fibrin gels: effect of variation in gel mechano-structural properties. *Biomaterials*, *22*(10), 1065–1075.

Dupont, S., Morsut, L., Aragona, M., Enzo, E., Giulitti, S., Cordenonsi, M., Zanconato, F., Le Digabel, J., Forcato, M., Bicciato, S., Elvassore, N., & Piccolo, S. (2011). Role of YAP/TAZ in mechanotransduction. *Nature*, *474*(7350), 179–183.

Engler, A. J., Griffin, M. A., Sen, S., Bönnemann, C. G., Sweeney, H. L., & Discher, D. E. (2004). Myotubes differentiate optimally on substrates with tissue-like stiffness: pathological implications for soft or stiff microenvironments. *The Journal of Cell Biology*, *166*(6), 877–887.

Engler, A. J., Rehfeldt, F., Sen, S., & Discher, D. E. (2007). Microtissue Elasticity: Measurements by Atomic Force Microscopy and Its Influence on Cell Differentiation. In *Methods in Cell Biology* (Vol. 83, pp. 521–545). Academic Press.

Engler, A. J., Richert, L., Wong, J. Y., Picart, C., & Discher, D. E. (2004). Surface probe measurements of the elasticity of sectioned tissue, thin gels and polyelectrolyte multilayer films: Correlations between substrate stiffness and cell adhesion. *Surface Science*, *570*(1), 142–154.

Engler, A. J., Sen, S., Sweeney, H. L., & Discher, D. E. (2006). Matrix elasticity directs stem cell lineage specification. *Cell*, *126*(4), 677–689.

Evani, S. J., Prabhu, R. G., Gnanaruban, V., Finol, E. A., & Ramasubramanian, A. K. (2013). Monocytes mediate metastatic breast tumor cell adhesion to endothelium under flow. *FASEB Journal: Official Publication of the Federation of American Societies for Experimental Biology*, *27*(8), 3017–3029.

Ewald, A. J., Brenot, A., Duong, M., Chan, B. S., & Werb, Z. (2008). Collective epithelial migration and cell rearrangements drive mammary branching morphogenesis. *Developmental Cell*, *14*(4), 570–581.

Fang, M., Yuan, J., Peng, C., & Li, Y. (2014). Collagen as a double-edged sword in tumor progression. *Tumour Biology: The Journal of the International Society for Oncodevelopmental Biology and Medicine*, *35*(4), 2871–2882.

Fernández, P. A., Buchmann, B., Goychuk, A., Engelbrecht, L. K., Raich, M. K., Scheel, C. H., Frey, E., & Bausch, A. R. (2021). Surface-tension-induced budding drives alveologenesis in human mammary gland organoids. *Nature Physics*, *17*, 1130–1136.

Fillmore, C. M., & Kuperwasser, C. (2008). Human breast cancer cell lines contain stem-like cells that self-renew, give rise to phenotypically diverse progeny and survive chemotherapy. *Breast Cancer Research: BCR*, *10*(2), R25.

Fraley, S. I., Feng, Y., Giri, A., Longmore, G. D., & Wirtz, D. (2012). Dimensional and temporal controls of three-dimensional cell migration by zyxin and binding partners. *Nature Communications*, *3*(1), 719.

Fraley, S. I., Feng, Y., Krishnamurthy, R., Kim, D.-H., Celedon, A., Longmore, G. D., & Wirtz, D. (2010). A distinctive role for focal adhesion proteins in three-dimensional cell motility. *Nature Cell Biology*, *12*(6), 598–604.

Fraley, S. I., Wu, P.-H., He, L., Feng, Y., Krisnamurthy, R., Longmore, G. D., & Wirtz, D. (2015). Three-dimensional matrix fiber alignment modulates cell migration and MT1-MMP utility by spatially and temporally directing protrusions. *Scientific Reports*, *5*, 14580.

Friedl, P., Locker, J., Sahai, E., & Segall, J. E. (2012). Classifying collective cancer cell invasion. *Nature Cell Biology*, *14*(8), 777–783.

Gaggioli, C., Hooper, S., Hidalgo-Carcedo, C., Grosse, R., Marshall, J. F., Harrington, K., & Sahai, E. (2007). Fibroblast-led collective invasion of carcinoma cells with differing roles for RhoGTPases in leading and following cells. *Nature Cell Biology*, *9*(12), 1392–1400.

Gennari, A., André, F., Barrios, C. H., Cortés, J., de Azambuja, E., DeMichele, A., Dent, R., Fenlon, D., Gligorov, J., Hurvitz, S. A., Im, S.-A., Krug, D., Kunz, W. G., Loi, S., Penault-Llorca, F., Ricke, J., Robson, M., Rugo, H. S., Saura, C., … ESMO Guidelines Committee. Electronic address: clinicalguidelines@esmo.org. (2021). ESMO Clinical Practice Guideline for the diagnosis, staging and treatment of patients with metastatic breast cancer. *Annals of Oncology: Official Journal of the European Society for Medical Oncology / ESMO*, *32*(12), 1475–1495.

Glazier, J. A., & Graner, F. (1993). Simulation of the differential adhesion driven rearrangement of biological cells. *Physical Review. E, Statistical Physics, Plasmas, Fluids, and Related Interdisciplinary Topics*, *47*(3), 2128–2154.

Glentis, A., Blanch-Mercader, C., Balasubramaniam, L., Saw, T. B., d'Alessandro, J., Janel, S., Douanier, A., Delaval, B., Lafont, F., Lim, C. T., Delacour, D., Prost, J., Xi, W., & Ladoux, B. (2022). The emergence of spontaneous coordinated epithelial rotation on cylindrical curved surfaces. *Science Advances*, *8*(37), eabn5406.

Golubkov, V. S., Boyd, S., Savinov, A. Y., Chekanov, A. V., Osterman, A. L., Remacle, A., Rozanov, D. V., Doxsey, S. J., & Strongin, A. Y. (2005). Membrane type-1 matrix metalloproteinase (MT1-MMP) exhibits an important intracellular cleavage function and causes chromosome instability. *The Journal of Biological Chemistry*, *280*(26), 25079–25086.

Grafinger, O. R., Gorshtein, G., Stirling, T., Brasher, M. I., & Coppolino, M. G. (2020). β1 integrin-mediated signaling regulates MT1-MMP phosphorylation to promote tumor cell invasion. *Journal of Cell Science*, *133*(9). https://doi.org/10.1242/jcs.239152

Graner, F., & Glazier, J. A. (1992). Simulation of biological cell sorting using a two-dimensional extended Potts model. *Physical Review Letters*, *69*(13), 2013–2016.

Grasset, E. M., Dunworth, M., Sharma, G., Loth, M., Tandurella, J., Cimino-Mathews, A., Gentz, M., Bracht, S., Haynes, M., Fertig, E. J., & Ewald, A. J. (2022). Triple-negative breast cancer metastasis involves complex epithelial-mesenchymal transition dynamics and requires vimentin. *Science Translational Medicine*, *14*(656), eabn7571.

Gudjonsson, T., Rønnov-Jessen, L., Villadsen, R., Rank, F., Bissell, M. J., & Petersen, O. W. (2002). Normal and tumor-derived myoepithelial cells differ in their ability to interact with luminal breast epithelial cells for polarity and basement membrane deposition. *Journal of Cell Science*, *115*(Pt 1), 39–50.

Guo, Y. P., Martin, L. J., Hanna, W., Banerjee, D., Miller, N., Fishell, E., Khokha, R., & Boyd, N. F. (2001). Growth factors and stromal matrix proteins associated with mammographic densities. *Cancer Epidemiology, Biomarkers & Prevention: A Publication of the American Association for Cancer Research, Cosponsored by the American Society of Preventive Oncology*, *10*(3), 243–248.

Habel, L. A., Dignam, J. J., Land, S. R., Salane, M., Capra, A. M., & Julian, T. B. (2004). Mammographic density and breast cancer after ductal carcinoma in situ. *Journal of the National Cancer Institute*, *96*(19), 1467–1472.

Haeger, A., Krause, M., Wolf, K., & Friedl, P. (2014). Cell jamming: collective invasion of mesenchymal tumor cells imposed by tissue confinement. *Biochimica et Biophysica Acta*, *1840*(8), 2386–2395.

Haidekker, M. (2011). *Advanced Biomedical Image Analysis* (1st ed.) [EPUB]. John Wiley & Sons.

Haigo, S. L., & Bilder, D. (2011). Global tissue revolutions in a morphogenetic movement controlling elongation. *Science*, *331*(6020), 1071–1074.

Halder, G., Dupont, S., & Piccolo, S. (2012). Transduction of mechanical and cytoskeletal cues by YAP and TAZ. *Nature Reviews. Molecular Cell Biology*, *13*(9), 591–600.

Hall, M. S., Alisafaei, F., Ban, E., Feng, X., Hui, C.-Y., Shenoy, V. B., & Wu, M. (2016). Fibrous nonlinear elasticity enables positive mechanical feedback between cells and ECMs. *Proceedings of the National Academy of Sciences of the United States of America*, *113*(49), 14043–14048.

Hiraki, H. L., Matera, D. L., Wang, W. Y., Prabhu, E. S., Zhang, Z., Midekssa, F., Argento, A. E., Buschhaus, J. M., Humphries, B. A., Luker, G. D., Pena-Francesch, A., & Baker, B. M. (2022). Fiber density and matrix stiffness modulate distinct cell migration modes in a

3D stroma mimetic composite hydrogel. *Acta Biomaterialia*. https://doi.org/10.1016/j.actbio.2022.09.043

Hosein, A. N., Brekken, R. A., & Maitra, A. (2020). Pancreatic cancer stroma: an update on therapeutic targeting strategies. *Nature Reviews. Gastroenterology & Hepatology*, *17*(8), 487–505.

Hou, J.-M., Krebs, M. G., Lancashire, L., Sloane, R., Backen, A., Swain, R. K., Priest, L. J. C., Greystoke, A., Zhou, C., Morris, K., Ward, T., Blackhall, F. H., & Dive, C. (2012). Clinical significance and molecular characteristics of circulating tumor cells and circulating tumor microemboli in patients with small-cell lung cancer. *Journal of Clinical Oncology: Official Journal of the American Society of Clinical Oncology*, *30*(5), 525–532.

Huang, W.-C., Chan, S.-T., Yang, T.-L., Tzeng, C.-C., & Chen, C.-C. (2004). Inhibition of ICAM-1 gene expression, monocyte adhesion and cancer cell invasion by targeting IKK complex: molecular and functional study of novel alpha-methylene-gamma-butyrolactone derivatives. *Carcinogenesis*, *25*(10), 1925–1934.

Ilina, O., Gritsenko, P. G., Syga, S., Lippoldt, J., La Porta, C. A. M., Chepizhko, O., Grosser, S., Vullings, M., Bakker, G.-J., Starruß, J., Bult, P., Zapperi, S., Käs, J. A., Deutsch, A., & Friedl, P. (2020). Cell–cell adhesion and 3D matrix confinement determine jamming transitions in breast cancer invasion. *Nature Cell Biology*, *22*(9), 1103–1115.

Ingber, D. E., Wang, N., & Stamenovic, D. (2014). Tensegrity, cellular biophysics, and the mechanics of living systems. *Reports on Progress in Physics. Physical Society (Great Britain)*, *77*(4), 046603.

Inman, J. L., Robertson, C., Mott, J. D., & Bissell, M. J. (2015). Mammary gland development: cell fate specification, stem cells and the microenvironment. *Development* , *142*(6), 1028–1042.

Jain, N., Iyer, K. V., Kumar, A., & Shivashankar, G. V. (2013). Cell geometric constraints induce modular gene-expression patterns via redistribution of HDAC3 regulated by actomyosin contractility. *Proceedings of the National Academy of Sciences of the United States of America*, *110*(28), 11349–11354.

Jain, S., Cachoux, V. M. L., Narayana, G. H. N. S., de Beco, S., D'Alessandro, J., Cellerin, V., Chen, T., Heuzé, M. L., Marcq, P., Mège, R.-M., Kabla, A. J., Lim, C. T., & Ladoux, B. (2020). The role of single-cell mechanical behaviour and polarity in driving collective cell migration. *Nature Physics*, *16*(7), 802–809.

Jawerth, L. M., Münster, S., Vader, D. A., Fabry, B., & Weitz, D. A. (2010). A blind spot in confocal reflection microscopy: the dependence of fiber brightness on fiber orientation in imaging biopolymer networks. *Biophysical Journal*, *98*(3), L1-3.

Jiang, G., Huang, A. H., Cai, Y., Tanase, M., & Sheetz, M. P. (2006). Rigidity sensing at the leading edge through alphavbeta3 integrins and RPTPalpha. *Biophysical Journal*, *90*(5), 1804–1809.

Jimenez, S. A., & Bashey, R. I. (1977). Identification of collagen α1(I) trimer in embryonic chick tendons and calvaria. *Biochemical and Biophysical Research Communications*, *78*(4), 1354–1361.

Jobin, P. G., Butler, G. S., & Overall, C. M. (2017). New intracellular activities of matrix metalloproteinases shine in the moonlight. *Biochimica et Biophysica Acta, Molecular Cell Research*, *1864*(11 Pt A), 2043–2055.

Kang, M. K., Hur, B. I., Ko, M. H., Kim, C. H., Cha, S. H., & Kang, S. K. (2008). Potential identity of multi-potential cancer stem-like subpopulation after radiation of cultured brain glioma. *BMC Neuroscience*, *9*(1), 15.

Kang, Y., & Pantel, K. (2013). Tumor cell dissemination: emerging biological insights from animal models and cancer patients. *Cancer Cell*, *23*(5), 573–581.

Khetan, S., Guvendiren, M., Legant, W. R., Cohen, D. M., Chen, C. S., & Burdick, J. A. (2013). Degradation-mediated cellular traction directs stem cell fate in covalently crosslinked three-dimensional hydrogels. *Nature Materials*, *12*(5), 458–465.

Kumar, S., & Weaver, V. M. (2009). Mechanics, malignancy, and metastasis: the force journey of a tumor cell. *Cancer Metastasis Reviews*, *28*(1–2), 113–127.

Kuznetsova, I. M., Turoverov, K. K., & Uversky, V. N. (2014). What macromolecular crowding can do to a protein. *International Journal of Molecular Sciences*, *15*(12), 23090–23140.

Ladoux, B., & Mège, R.-M. (2017). Mechanobiology of collective cell behaviours. *Nature Reviews. Molecular Cell Biology*, *18*(12), 743–757.

Lambert, A. W., & Weinberg, R. A. (2021). Linking EMT programmes to normal and neoplastic epithelial stem cells. *Nature Reviews. Cancer*, *21*(5), 325–338.

Lang, N. R., Münster, S., Metzner, C., Krauss, P., Schürmann, S., Lange, J., Aifantis, K. E., Friedrich, O., & Fabry, B. (2013). Estimating the 3D pore size distribution of biopolymer networks from directionally biased data. *Biophysical Journal*, *105*(9), 1967–1975.

Lareu, R. R., Subramhanya, K. H., Peng, Y., Benny, P., Chen, C., Wang, Z., Rajagopalan, R., & Raghunath, M. (2007). Collagen matrix deposition is dramatically enhanced in vitro when crowded with charged macromolecules: the biological relevance of the excluded volume effect. *FEBS Letters*, *581*(14), 2709–2714.

Lee, M. H., Goralczyk, A. G., Kriszt, R., Ang, X. M., Badowski, C., Li, Y., Summers, S. A., Toh, S.-A., Yassin, M. S., Shabbir, A., Sheppard, A., & Raghunath, M. (2016). ECM

microenvironment unlocks brown adipogenic potential of adult human bone marrow-derived MSCs. *Scientific Reports*, *6*(1), 21173.

Leineweber, W. D., & Fraley, S. I. (2023). Adhesion tunes speed and persistence by coordinating protrusions and extracellular matrix remodeling. *Developmental Cell*, *0*(0). https://doi.org/10.1016/j.devcel.2023.05.013

Levental, K. R., Yu, H., Kass, L., Lakins, J. N., Egeblad, M., Erler, J. T., Fong, S. F. T., Csiszar, K., Giaccia, A., Weninger, W., Yamauchi, M., Gasser, D. L., & Weaver, V. M. (2009). Matrix crosslinking forces tumor progression by enhancing integrin signaling. *Cell*, *139*(5), 891–906.

Liu, G., Li, Y., Yang, L., Wei, Y., Wang, X., Wang, Z., & Tao, L. (2017). Cytotoxicity study of polyethylene glycol derivatives. *RSC Advances*, *7*(30), 18252–18259.

Lo, C. M., Wang, H. B., Dembo, M., & Wang, Y. L. (2000). Cell movement is guided by the rigidity of the substrate. *Biophysical Journal*, *79*(1), 144–152.

Love, M. I., Huber, W., & Anders, S. (2014). Moderated estimation of fold change and dispersion for RNA-seq data with DESeq2. *Genome Biology*, *15*(12), 550.

Lutolf, M. P., & Hubbell, J. A. (2005). Synthetic biomaterials as instructive extracellular microenvironments for morphogenesis in tissue engineering. *Nature Biotechnology*, *23*(1), 47–55.

Magno, V., Friedrichs, J., Weber, H. M., Prewitz, M. C., Tsurkan, M. V., & Werner, C. (2017). Macromolecular crowding for tailoring tissue-derived fibrillated matrices. *Acta Biomaterialia*, *55*, 109–119.

McKenzie, A. J., Hicks, S. R., Svec, K. V., Naughton, H., Edmunds, Z. L., & Howe, A. K. (2018). The mechanical microenvironment regulates ovarian cancer cell morphology, migration, and spheroid disaggregation. *Scientific Reports*, *8*(1). https://doi.org/10.1038/s41598-018-25589-0

Moffitt, R. A., Marayati, R., Flate, E. L., Volmar, K. E., Loeza, S. G. H., Hoadley, K. A., Rashid, N. U., Williams, L. A., Eaton, S. C., Chung, A. H., Smyla, J. K., Anderson, J. M., Kim, H. J., Bentrem, D. J., Talamonti, M. S., Iacobuzio-Donahue, C. A., Hollingsworth, M. A., & Yeh, J. J. (2015). Virtual microdissection identifies distinct tumor- and stroma-specific subtypes of pancreatic ductal adenocarcinoma. *Nature Genetics*, *47*(10), 1168–1178.

Ng, W. L., Goh, M. H., Yeong, W. Y., & Naing, M. W. (2018). Applying macromolecular crowding to 3D bioprinting: fabrication of 3D hierarchical porous collagen-based hydrogel constructs. *Biomaterials Science*, *6*(3), 562–574.

Oliveira, A. L., Sun, L., Kim, H. J., Hu, X., Rice, W., Kluge, J., Reis, R. L., & Kaplan, D. L. (2012). Aligned silk-based 3-D architectures for contact guidance in tissue engineering. *Acta Biomaterialia*, *8*(4), 1530–1542.

Ong, S.-E., Schenone, M., Margolin, A. A., Li, X., Do, K., Doud, M. K., Mani, D. R., Kuai, L., Wang, X., Wood, J. L., Tolliday, N. J., Koehler, A. N., Marcaurelle, L. A., Golub, T. R., Gould, R. J., Schreiber, S. L., & Carr, S. A. (2009). Identifying the proteins to which small-molecule probes and drugs bind in cells. *Proceedings of the National Academy of Sciences of the United States of America*, *106*(12), 4617–4622.

Overby, D., Ruberti, J., Gong, H., Freddo, T. F., & Johnson, M. (2001). Specific hydraulic conductivity of corneal stroma as seen by quick-freeze/deep-etch. *Journal of Biomechanical Engineering*, *123*(2), 154–161.

Packard, B. Z., Artym, V. V., Komoriya, A., & Yamada, K. M. (2009). Direct visualization of protease activity on cells migrating in three-dimensions. *Matrix Biology: Journal of the International Society for Matrix Biology*, *28*(1), 3–10.

Park, G.-S., & Kim, J.-H. (2015). LPS up-regulates ICAM-1 expression in breast cancer cells by stimulating a MyD88-BLT2-ERK-linked cascade, which promotes adhesion to monocytes. *Molecules and Cells*, *38*(9), 821–828.

Park, S.-Y., Choi, J.-H., & Nam, J.-S. (2019). Targeting cancer stem cells in triple-negative breast cancer. *Cancers*, *11*(7), 965.

Parkinson, J., Kadler, K. E., & Brass, A. (1995). Simple physical model of collagen fibrillogenesis based on diffusion limited aggregation. *Journal of Molecular Biology*, *247*(4), 823–831.

Parsegian, V. A., Rand, R. P., & Rau, D. C. (2000). Osmotic stress, crowding, preferential hydration, and binding: A comparison of perspectives. *Proceedings of the National Academy of Sciences of the United States of America*, *97*(8), 3987–3992.

Paszek, M. J., Zahir, N., Johnson, K. R., Lakins, J. N., Rozenberg, G. I., Gefen, A., Reinhart-King, C. A., Margulies, S. S., Dembo, M., Boettiger, D., Hammer, D. A., & Weaver, V. M. (2005). Tensional homeostasis and the malignant phenotype. *Cancer Cell*, *8*(3), 241–254.

Pattabiraman, D. R., Bierie, B., Kober, K. I., Thiru, P., Krall, J. A., Zill, C., Reinhardt, F., Tam, W. L., & Weinberg, R. A. (2016). Activation of PKA leads to mesenchymal-to-epithelial transition and loss of tumor-initiating ability. *Science*, *351*(6277), aad3680.

Peitzsch, C., Kurth, I., Kunz-Schughart, L., Baumann, M., & Dubrovska, A. (2013). Discovery of the cancer stem cell related determinants of radioresistance. *Radiotherapy and Oncology: Journal of the European Society for Therapeutic Radiology and Oncology*, *108*(3), 378–387.

Piscuoglio, S., Hodi, Z., Katabi, N., Guerini-Rocco, E., Macedo, G. S., Ng, C. K. Y., Edelweiss, M., De Mattos-Arruda, L., Wen, H. Y., Rakha, E. A., Ellis, I. O., Rubin, B. P., Weigelt, B., & Reis-Filho, J. S. (2015). Are acinic cell carcinomas of the breast and salivary glands distinct diseases? *Histopathology*, *67*(4), 529–537.

Popkova, A., Stone, O. J., Chen, L., Qin, X., Liu, C., Liu, J., Belguise, K., Montell, D. J., Hahn, K. M., Rauzi, M., & Wang, X. (2020). A Cdc42-mediated supracellular network drives polarized forces and Drosophila egg chamber extension. *Nature Communications*, *11*(1), 1921.

Provenzano, P. P., Inman, D. R., Eliceiri, K. W., & Keely, P. J. (2009). Matrix density-induced mechanoregulation of breast cell phenotype, signaling and gene expression through a FAK-ERK linkage. *Oncogene*, *28*(49), 4326–4343.

Provenzano, Paolo P., Eliceiri, K. W., Campbell, J. M., Inman, D. R., White, J. G., & Keely, P. J. (2006). Collagen reorganization at the tumor-stromal interface facilitates local invasion. *BMC Medicine*, *4*(1), 38.

Provenzano, Paolo P., Eliceiri, K. W., Inman, D. R., & Keely, P. J. (2010). Engineering three-dimensional collagen matrices to provide contact guidance during 3D cell migration. *[Current Protocols in Cell Biology]*, *Chapter 10*(1), Unit 10.17.

Provenzano, Paolo P., Inman, D. R., Eliceiri, K. W., Knittel, J. G., Yan, L., Rueden, C. T., White, J. G., & Keely, P. J. (2008). Collagen density promotes mammary tumor initiation and progression. *BMC Medicine*, *6*, 11.

Radmacher, M., Fritz, M., & Hansma, P. K. (1995). Imaging soft samples with the atomic force microscope: gelatin in water and propanol. *Biophysical Journal*, *69*(1), 264–270.

Ranamukhaarachchi, S. K., Modi, R. N., Han, A., Velez, D. O., Kumar, A., Engler, A. J., & Fraley, S. I. (2019). Macromolecular crowding tunes 3D collagen architecture and cell morphogenesis. *Biomaterials Science*, *7*(2), 618–633.

Rappel, W.-J., Nicol, A., Sarkissian, A., Levine, H., & Loomis, W. F. (1999). Self-organized Vortex State in Two-Dimensional Dictyostelium Dynamics. *Physical Review Letters*, *83*(6), 1247–1250.

Rashid, R., Lim, N. S. J., Chee, S. M. L., Png, S. N., Wohland, T., & Raghunath, M. (2014). Novel use for polyvinylpyrrolidone as a macromolecular crowder for enhanced extracellular matrix deposition and cell proliferation. *Tissue Engineering. Part C, Methods*, *20*(12), 994–1002.

Ray, A., Slama, Z. M., Morford, R. K., Madden, S. A., & Provenzano, P. P. (2017). Enhanced Directional Migration of Cancer Stem Cells in 3D Aligned Collagen Matrices. *Biophysical Journal*, *112*(5), 1023–1036.

Richert, L., Engler, A. J., Discher, D. E., & Picart, C. (2004). Elasticity of native and cross-linked polyelectrolyte multilayer films. *Biomacromolecules*, *5*(5), 1908–1916.

Rubinson, K. A., & Krueger, S. (2009). Poly(ethylene glycol)s 2000–8000 in water may be planar: A small-angle neutron scattering (SANS) structure study. *Polymer*, *50*(20), 4852–4858.

Russell, J. L., Goetsch, S. C., Aguilar, H. R., Coe, H., Luo, X., Liu, N., van Rooij, E., Frantz, D. E., & Schneider, J. W. (2012). Regulated expression of pH sensing G Protein-coupled receptor-68 identified through chemical biology defines a new drug target for ischemic heart disease. *ACS Chemical Biology*, *7*(6), 1077–1083.

Salvalaggio, P. R. O., Deng, S., Ariyan, C. E., Millet, I., Zawalich, W. S., Basadonna, G. P., & Rothstein, D. M. (2002). Islet filtration: a simple and rapid new purification procedure that avoids ficoll and improves islet mass and function. *Transplantation*, *74*(6), 877–879.

Schnauß, J., Händler, T., & Käs, J. A. (2016). Semiflexible biopolymers in bundled arrangements. *Polymers*, *8*(8), 274.

Schneider, J. W., Gao, Z., Li, S., Farooqi, M., Tang, T.-S., Bezprozvanny, I., Frantz, D. E., & Hsieh, J. (2008). Small-molecule activation of neuronal cell fate. *Nature Chemical Biology*, *4*(7), 408–410.

Schneider, J. W., Goetsch, S. C., Leng, X., Ludwig, S. M., Russell, J. L., Yang, C.-P., & Zhang, Q.-J. (2012). Coupling hippocampal neurogenesis to brain pH through proneurogenic small molecules that regulate proton sensing G protein-coupled receptors. *ACS Chemical Neuroscience*, *3*(7), 557–568.

Schröder, C., Witzel, I., Müller, V., Krenkel, S., Wirtz, R. M., Jänicke, F., Schumacher, U., & Milde-Langosch, K. (2011). Prognostic value of intercellular adhesion molecule (ICAM)-1 expression in breast cancer. *Journal of Cancer Research and Clinical Oncology*, *137*(8), 1193–1201.

Silver, F. H., & Birk, D. E. (1983). Kinetic analysis of collagen fibrillogenesis: I. Use of turbidity--time data. *Collagen and Related Research*, *3*(5), 393–405.

Simon, T., & Bromberg, J. S. (2017). Regulation of the Immune System by Laminins. *Trends in Immunology*, *38*(11), 858–871.

Sokol, E. S., Miller, D. H., Breggia, A., Spencer, K. C., Arendt, L. M., & Gupta, P. B. (2016). Growth of human breast tissues from patient cells in 3D hydrogel scaffolds. *Breast Cancer Research: BCR*, *18*(1), 19.

Soslau, G., Mason, C., Lynch, S., Benjamin, J., Ashak, D., Prakash, J. M., Moore, A., Bagsiyao, P., Albert, T., Mathew, L. M., & Jost, M. (2014). Intracellular matrix metalloproteinase-2

(MMP-2) regulates human platelet activation via hydrolysis of talin. *Thrombosis and Haemostasis*, *111*(1), 140–153.

Stylianou, S., Clarke, R. B., & Brennan, K. (2006). Aberrant activation of notch signaling in human breast cancer. *Cancer Research*, *66*(3), 1517–1525.

Sung, M. M., Schulz, C. G., Wang, W., Sawicki, G., Bautista-López, N. L., & Schulz, R. (2007). Matrix metalloproteinase-2 degrades the cytoskeletal protein alpha-actinin in peroxynitrite mediated myocardial injury. *Journal of Molecular and Cellular Cardiology*, *43*(4), 429–436.

Szardenings, K., Li, B., Ma, L., & Wu, M. (2004). Fishing for targets: novel approaches using small molecule baits. *Drug Discovery Today. Technologies*, *1*(1), 9–15.

Tanner, K., Mori, H., Mroue, R., Bruni-Cardoso, A., & Bissell, M. J. (2012). Coherent angular motion in the establishment of multicellular architecture of glandular tissues. *Proceedings of the National Academy of Sciences of the United States of America*, *109*(6), 1973–1978.

Ursin, G., Hovanessian-Larsen, L., Parisky, Y. R., Pike, M. C., & Wu, A. H. (2005). Greatly increased occurrence of breast cancers in areas of mammographically dense tissue. *Breast Cancer Research: BCR*, *7*(5), R605-8.

Velez, D. O., Tsui, B., Goshia, T., Chute, C. L., Han, A., Carter, H., & Fraley, S. I. (2017). 3D collagen architecture induces a conserved migratory and transcriptional response linked to vasculogenic mimicry. *Nature Communications*, *8*(1), 1651.

Velez, Daniel O., Ranamukhaarachchi, S. K., Kumar, A., Modi, R. N., Lim, E. W., Engler, A. J., Metallo, C. M., & Fraley, S. I. (2019). 3D collagen architecture regulates cell adhesion through degradability, thereby controlling metabolic and oxidative stress. *Integrative Biology: Quantitative Biosciences from Nano to Macro*, *11*(5), 221–234.

Wada, K.-I., Itoga, K., Okano, T., Yonemura, S., & Sasaki, H. (2011). Hippo pathway regulation by cell morphology and stress fibers. *Development (Cambridge, England)*, *138*(18), 3907–3914.

Walters, N. J., & Gentleman, E. (2015). Evolving insights in cell-matrix interactions: elucidating how non-soluble properties of the extracellular niche direct stem cell fate. *Acta Biomaterialia*, *11*, 3–16.

Wang, H., Lacoche, S., Huang, L., Xue, B., & Muthuswamy, S. K. (2013). Rotational motion during three-dimensional morphogenesis of mammary epithelial acini relates to laminin matrix assembly. *Proceedings of the National Academy of Sciences of the United States of America*, *110*(1), 163–168.

Weaver, V. M., Petersen, O. W., Wang, F., Larabell, C. A., Briand, P., Damsky, C., & Bissell, M. J. (1997). Reversion of the malignant phenotype of human breast cells in three-dimensional culture and in vivo by integrin blocking antibodies. *The Journal of Cell Biology*, *137*(1), 231–245.

Wei, S. C., Fattet, L., Tsai, J. H., Guo, Y., Pai, V. H., Majeski, H. E., Chen, A. C., Sah, R. L., Taylor, S. S., Engler, A. J., & Yang, J. (2015). Matrix stiffness drives epithelial-mesenchymal transition and tumour metastasis through a TWIST1-G3BP2 mechanotransduction pathway. *Nature Cell Biology*, *17*(5), 678–688.

Welch, D. R., & Hurst, D. R. (2019). Defining the Hallmarks of Metastasis. *Cancer Research*, *79*(12), 3011–3027.

Wess, T. J. (2005). *Advances in Protein Chemistry* (Vol. 70, pp. 341–374). Academic Press.

Wolf, K., Te Lindert, M., Krause, M., Alexander, S., Te Riet, J., Willis, A. L., Hoffman, R. M., Figdor, C. G., Weiss, S. J., & Friedl, P. (2013). Physical limits of cell migration: control by ECM space and nuclear deformation and tuning by proteolysis and traction force. *The Journal of Cell Biology*, *201*(7), 1069–1084.

Wolf, K., Wu, Y. I., Liu, Y., Geiger, J., Tam, E., Overall, C., Stack, M. S., & Friedl, P. (2007). Multi-step pericellular proteolysis controls the transition from individual to collective cancer cell invasion. *Nature Cell Biology*, *9*(8), 893–904.

Wood, G. C., & Keech, M. K. (1960). The formation of fibrils from collagen solutions. 1. The effect of experimental conditions: kinetic and electron-microscope studies. *Biochemical Journal*, *75*, 588–598.

Wyckoff, J. B., Pinner, S. E., Gschmeissner, S., Condeelis, J. S., & Sahai, E. (2006). ROCK- and myosin-dependent matrix deformation enables protease-independent tumor-cell invasion in vivo. *Current Biology: CB*, *16*(15), 1515–1523.

Xie, J., Bao, M., Bruekers, S. M. C., & Huck, W. T. S. (2017). Collagen Gels with Different Fibrillar Microarchitectures Elicit Different Cellular Responses. *ACS Applied Materials & Interfaces*, *9*(23), 19630–19637.

Yang, L., Shi, P., Zhao, G., Xu, J., Peng, W., Zhang, J., Zhang, G., Wang, X., Dong, Z., Chen, F., & Cui, H. (2020). Targeting cancer stem cell pathways for cancer therapy. *Signal Transduction and Targeted Therapy*, *5*(1), 8.

Yue, X., Lukowski, J. K., Weaver, E. M., Skube, S. B., & Hummon, A. B. (2016). Quantitative proteomic and phosphoproteomic comparison of 2D and 3D colon cancer cell culture models. *Journal of Proteome Research*, *15*(12), 4265–4276.

Zeng, Y.-N., Kang, Y.-L., Rau, L.-R., Hsu, F.-Y., & Tsai, S.-W. (2017). Construction of cell-containing, anisotropic, three-dimensional collagen fibril scaffolds using external

vibration and their influence on smooth muscle cell phenotype modulation. *Biomedical Materials (Bristol, England)*, *12*(4), 045019.

Zhang, J., Goliwas, K. F., Wang, W., Taufalele, P. V., Bordeleau, F., & Reinhart-King, C. A. (2019). Energetic regulation of coordinated leader–follower dynamics during collective invasion of breast cancer cells. *Proceedings of the National Academy of Sciences*, *116*(16), 7867–7872.

Zheng, F., Kelly, M. R., Ramms, D. J., Heintschel, M. L., Tao, K., Tutuncuoglu, B., Lee, J. J., Ono, K., Foussard, H., Chen, M., Herrington, K. A., Silva, E., Liu, S. N., Chen, J., Churas, C., Wilson, N., Kratz, A., Pillich, R. T., Patel, D. N., … Ideker, T. (2021). Interpretation of cancer mutations using a multiscale map of protein systems. *Science*, *374*(6563), eabf3067.